UNIVERSITY OF SOUTHAMPTON

# NOVEL ACTIVE WAVEGUIDE DEVICES IN DIRECT-BONDED STRUCTURES

**by**

**Corin B. E. Gawith**

A thesis submitted for the degree of
Doctor of Philosophy

FACULTY OF ENGINEERING AND APPLIED SCIENCE
OPTOELECTRONICS RESEARCH CENTRE

SEPTEMBER 2001

UNIVERSITY OF SOUTHAMPTON

## ABSTRACT

FACULTY OF ENGINEERING AND APPLIED SCIENCE
OPTOELECTRONICS RESEARCH CENTRE

Doctor of Philosophy

# NOVEL ACTIVE WAVEGUIDE DEVICES IN DIRECT-BONDED STRUCTURES

by

Corin B. E. Gawith

This thesis describes a series of experimental studies on the use of direct bonding for optical waveguide fabrication. The direct bonding technique involves contacting two ultra-clean polished surfaces to form an adhesive-free vacuum-tight bond. Optical materials bonded in this way can be formed into waveguide devices, and this work extends direct bonding to include periodically poled materials and a new solid-state ion-exchange process.

The first result of this work describes the fabrication of a 5.5-mm-long, 12-μm-thick periodically poled $LiNbO_3$ planar waveguide buried in $LiTaO_3$. Frequency doubling experiments performed with this device demonstrate a conversion efficiency of 4.3 $\%W^{-1}$, a value 40% greater than that calculated for an optimised bulk device of similar length.

Also demonstrated is a photorefractive iron-doped $LiNbO_3$ waveguide buried in non-photorefractive magnesium-doped $LiNbO_3$. In optical limiting experiments this device demonstrates a change in optical density of 2 and photorefractive response time of 5 milliseconds, representing 20 times greater optical limiting and 60 times faster operational speed than the bulk material.

$K^+$-$Na^+$ ion-exchange between direct-bonded glass layers is studied and used as a novel solid-state technique for waveguide fabrication. This process is also developed to incorporate direct-UV-written channel waveguides in an ion-exchanged buried photosensitive glass layer. Finally, operation of a single-mode channel waveguide laser in neodymium-doped photosensitive SGBN glass (based on a composition of silica, germania, boron, and sodium) is demonstrated, with propagation losses of $< 0.3$ dB $cm^{-1}$ and milliwatt-order lasing thresholds.

**Acknowledgements**

It has been a pleasure working at the Optoelectronics Research Center for the past few years and I have enjoyed my research a great deal. This is in no small part due to my project supervisor, Dr. Peter Smith, who somehow managed not only to find the ideal area of research for me, but also to give me the support, advice, and freedom necessary to develop and explore my own ideas. For this I am extremely grateful.

Thanks must also go to my colleagues at the ORC who have taught me so much, particularly; Ping Hua, Dave Sager, Dr. Graeme Ross, and Dr. David Shepherd, for all their patience, time and advice. I would also like to thank my collaborators from outside Southampton; Dr. Gary Cook from DERA for including me in such an interesting project, and Prof. Hiromasa Ito from Tohoku University for providing me with the opportunity to live and work in Japan for a glorious summer.

To my friends, who have kept me smiling throughout, thanks guys! Wozzie, Paul, Al, Louise, Tracy, Stu, Ed, Alex, Arshad, Greg, Sam, Joyce, Jude, Dan and Sally (who somehow managed to work even stranger hours than I did), you're all too cool for words.

For my family and friends from back home, for all your love and support, thank you.

And to Miya, thank you for everything.

# CONTENTS

# CONTENTS

“I think we’re all a little wiser now.”

- *Optimus Prime* (1988)

# Chapter 1
# INTRODUCTION

## 1.1 Motivation and aims

The concept of adhesive-free bonding, or gluing without glue, is centuries old. Cited references lead as far back as the 13th century when the Fransiscan friar Bartholomaeus Anglicus stressed the importance of cleanliness when joining silver and gold, and to discussions by Galilei in the early 1600's describing the adhesion of smooth marble, metal, or glass plates where rough ones would not (for these and other events in the history of direct bonding refer to the recent review article by Plößl and Kräuter [1]). Refered to as 'wringing on', 'ansprengen' (from the German 'to jump on'), and 'contact optique', the spontaneous cohesion of optically finished solids moved from a scientific curiosity to an undesirable nuisance in the early 1900's as it became common for delicate and expensive parts produced by newly developed optical polishing technology to be accidentally joined so tightly that they could not be parted again [1-2]. Sixty years on, and the advent of laser technology heralded a new direction for this physical phenomenon, as what would become known as the 'direct bonding' technique was developed to create precision aligned, vacuum tight, mirror-bearing optical flats to be fused to the ends of a short and stable silica-bodied gas laser [3-4]. Developed at the Philips Research laboratories in the Netherlands in 1962, these laser systems represented the first commercial application of direct bonding and would be applied to form the basis of early laserdisc technology [2-4].

Since the mid-1980's interest in direct bonding has developed along with the silicon-on-insulator and semiconductor industries [1,5-7]. The process of bonding and thinning silicon and oxidised silicon wafers for semiconductor devices is by far the most widely studied topic in direct bonding to date and numerous reviews have been written on the subject (the most comprehensive of which constitutes an entire issue of the Philips Journal of Research [2-3,5-6,8-14]). However, despite being founded on a technique used for optics, the development of direct-bonding in the optoelectronics industry has remained limited, simply due to the advanced technologies required for preparation, bonding, and post treatment of samples, and the inherent costs involved (see Chapter 2). As such, research in this field remains limited to a few groups

worldwide, and each with specifically chosen applications. These include; lithium niobate waveguide layers for electro-optic applications [15-16], layered stacks of periodically-poled lithium niobate for high power operation [17], multi-layered stacks of gallium arsenide for use in quasi-phase-matching [18-19], large (multipart) Ti:sapphire laser crystals for increased areas of good optical quality [20], Pyrex wafers for ion-exchange processes [21], ion-exchanged buried channel waveguides [22], and planar waveguide lasers [23-24]. The latter of these devices was supplied (prior to the start of this project) for characterisation at the Optoelectronics Research Centre by an American adhesive-free-bonding company called Onyx Optics [25], and exhibited excellent waveguiding properties suitable for application to wide a range of material and device types. However, direct bonding is by no means a mainstream technology and very little of the available scope offered by direct-bonded structures to the field of optoelectronics has been explored.

To this end, the research described in this thesis is based upon the development of novel active planar waveguide devices in direct-bonded structures. The primary aim of this project is to introduce and develop a specialised direct bonding fabrication technique for use with the polishing and clean-room facilities available at the Optoelectronics Research Centre, and to integrate that technique into existing waveguide and device technologies. The objective of this research is the design and fabrication of highly efficient waveguide structures based on the low-loss interfacial properties previously demonstrated in direct-bonded structures [23-24]. Of particular interest is the concept that any two materials with suitable surface preparation can be direct-bonded, regardless of structure or composition (a theory that has yet to be universally proven by practical means) [1], and that direct bonding can be used to preserve the bulk characteristics of each bonded material layer (provided the annealing temperature does not exceed that for material modification) [16]. This has proven to be of particular importance during work with complex structures, such as the domain inverted regions in periodically-poled lithium niobate, as the conservation of the full periodicity and nonlinearity of the material (properties which tend to be degraded by alternative waveguide fabrication techniques in this material, as discussed in Chapter 3) within a direct-bonded waveguide device has provided highly efficient results in the field of nonlinear frequency conversion.

Somewhat ironically, other experiments in this thesis have acted towards deliberately altering the bulk properties of direct-bonded substrates to determine novel waveguide fabrication techniques. In particular it has been discovered that the atomically smooth interface between two direct-bonded layers is an ideal boundary for ionic diffusion between glass layers of different chemical compositions. This inherent versatility, in what is still a relatively unexplored field of optical waveguide design and fabrication, lends itself readily to the discovery of new processes and techniques, while adding subtle twists to existing technologies. As such, the motivating force behind this project is the production of novel waveguide configurations and devices in direct-bonded structures, with a view to increasing awareness of this little-known technique and further integrating it for use in marketable optical technology. However, it will only be by the creation of significantly specialised devices that the commercial viability of direct bonding in the field of optoelectronics will ever truly be proven.

## 1.2 Thesis Synopsis

Direct bonding has proven to be a versatile technique for use in waveguide design and fabrication, and several distinct device types have been realised during this project. Spanning a variety of optoelectronics fields and processes, from nonlinear effects and laser waveguiding, to UV-writing and material microstructuring, the principal results in this thesis are presented as stand-alone chapters, chronicling the history and background of investigated research areas, the current state of technology, and the advantages offered by a direct-bonded waveguide configuration. In each case the processes used to design, fabricate, and characterise a waveguide device are presented in full, as are experimental results of device performance.

Beginning with a brief overview of the factors involved in the design and fabrication of direct-bonded structures, Chapter 2 describes the direct bonding technique developed for use at the Optoelectronics Research Centre, early examples of bonded samples, and the waveguide theory used to design a direct-bonded waveguide device. Chapter 3 describes the nonlinear process of quasi-phase-matched second-harmonic generation in periodically-poled lithium nobate and the enhanced conversion efficiency available in a buried planar waveguide configuration. In a similar format, Chapter 4 introduces the process of nonreciprocal transmission in iron-doped lithium

niobate and the direct-bonded planar structure that represents the first efficient waveguide device in this material for this application. Chapter 5 moves on to the topic of alkali ion-exchange in borosilicate glass, introducing the technique of intersubstrate ion-exchange between direct-bonded glass layers and its application towards low-loss active planar waveguide devices. This research is extended in Chapter 6 with a discussion of photosensitivity in glass substrates and the application of direct UV writing to create single-mode channel waveguides in a buried ion-exchanged layer. Conclusions and a brief description of the numerous direct bonding experiments and collaborative projects planned for future work at the University of Southampton are discussed in Chapter 7.

## REFERENCES

[1] A. Plößl and G. Kräuter, "*Wafer direct bonding: tailoring adhesion between brittle materials*", Materials Science and Engineering, Vol. R25, No. 1-2, p.1-88 (1999).

[2] J. Haisma, G. A. C. M. Spierings, and T. L. Michielsen, "*Frameworks for direct bonding*", Philips Journal of Research, Vol. 49, p.11-21 (1995).

[3] U. K. P. Biermann, A. A. van Gorkum, and J. A. Pals, "*Direct bonding: from an optical technology to a broad research topic*", Philips Journal of Research, Vol. 49, p.1-10 (1995).

[4] J. Haisma, G. A. C. M. Spierings, U. K. P. Biermann, and A. A. van Gorkum, "*Diversity and feasibility of direct bonding: a survey of a dedicated optical technology*", Applied Optics, Vol. 33, No. 7, p.1154-1169 (1994).

[5] J. Haisma, T. M. Michielsen, and F. J. H. M. van der Kruis, "*Silicon-wafer fabrication and (potential) applications of direct-bonded silicon*", Philips Journal of Research, Vol. 49, p.65-89 (1995).

[6] J. Haisma, "*Direct bonding in patent literature*", Philips Journal of Research, Vol. 49, p.165-170, (1995).

[7] Q. Y. Tong and U. Gösele, "*Semiconductor wafer bonding*", Wiley Interscience (1999).

[8] J. Haisma, G. A. C. M. Spierings, T. L. Michielsen, and C. L. Adema, "*Surface preparation and phenomenological aspects of direct bonding*", Philips Journal of Research, Vol. 49, p.23-46 (1995).

[9] G. A. C. M. Spierings, J. Haisma, and T. L. Michielsen, "*Surface related phenomena in the direct bonding of silicon and fused-silica wafer pairs*", Philips Journal of Research, Vol. 49, p.47-63 (1995).

[10] H. Baumgart, T. J. Letavic, and R. Egloff, "*Evaluation of wafer bonding and etch back for SOI technology*", Philips Journal of Research, Vol. 49, p.91-124 (1995).

[11] R. Egloff, T. Letavic, B. Greenberg, and H. Baumgart, "*Evaluation of strain sources in bond and etchback silicon-on-insulator*", Philips Journal of Research, Vol. 49, p.125-138 (1995).

[12] G. A. C. M. Spierings, J. Haisma, and F. J. H. M. van der Kruis, "*Direct bonding of organic polymeric materials*", Philips Journal of Research, Vol. 49, p.139-149 (1995).

[13] J. Haisma, J. J. C. Groenen, and P. W. de Haas, "*Non-silicon applications of direct bonding*", Philips Journal of Research, Vol. 49, p.151-163 (1995).

[14] J. Haisma, "*Direct bonding: retrospect and outlook*", Philips Journal of Research, Vol. 49, p.171-177 (1995).

[15] Y. Tomita, M. Sugimoto, and K. Eda, "*Direct bonding of $LiNbO_3$ single crystals for optical waveguides*", Applied Physics Letters, Vol. 66, No. 12, p.1484-1485 (1995).

[16] K. Eda, M. Sugimoto, and Y. Tomita, "*Direct heterobonding of lithium niobate onto lithium tantalate*", Applied Physics Letters, Vol. 66, No. 7, p.827-829 (1995).

[17] M. J. Missey, V. Dominic, L. E. Myers, and R. C. Eckardt, "*Diffusion-bonded stacks of periodically poled lithium niobate*", Optics Letters, Vol. 23, No. 9, p.664-666 (1998).

[18] Y. S. Wu, R. S. Fiegelson, R. K. Route, D. Zheng, L. A. Gordon, M. M. Fejer, and R. L. Byer, "*Improved GaAs bonding process for quasi-phase-matched second harmonic generation*", Journal of the Electrochemical Society, Vol. 145, No. 1, p.366-371 (1998).

[19] E. Lallier, L. Becouarn, M. Brévignon, and J. Lehoux, "*Infrared difference frequency generation with quasi-phase-matched GaAs*", Electronics Letters, Vol. 34, No. 6, p.1609-1611 (1998).

[20] A. Sugiyama, H. Fukuyama, T. Sasuga, T. Arisawa, and H. Takuma, "*Direct bonding of Ti:Sapphire crystals*", Applied Optics, Vol. 37, No. 12, p.2407-2410 (1998).

[21] F. Pigeon, B. Biasse, and M. Zussy, "*Low-temperature Pyrex glass wafer direct bonding*", Electronics Letters, Vol. 31, No. 10, p.792-793 (1995).

[22] S. Péllisier, F. Pigeon, B. Biasse, M. Zussy, G. Pandraud, and A. Mure-Ravaud, "*New technique to produce buried channel waveguides in glass*", Optical Engineering, Vol. 37, No. 4, p.1111-1114 (1998).

[23] C. T. A. Brown, C. L. Bonner, T. J. Warburton, D. P. Shepherd, A. C. Tropper, and D. C. Hanna, "*Thermally bonded planar waveguide lasers*", Applied Physics Letters, Vol. 71, No. 9, p.1139-1141 (1997).

[24] C. L. Bonner, T. Bhutta, D. P. Shepherd, and A. C. Tropper, "*Double-clad structures and proximity coupling for diode-bar-pumped planar waveguide lasers*", IEEE Journal of Quantum Electronics, Vol. 36, No. 2, p.236-242 (2000).

[25] www.onyxoptics.com

# Chapter 2
# DIRECT BONDING

## 2.1 Introduction

It is a well-known phenomenon that two flat solids will stick to each other when their surfaces are pushed together [1]. If these surfaces are sufficiently flat and clean, attractive forces will pull the two bodies into intimate contact and allow the formation of atomic bonds between the two solids, causing a structural transition from a system containing two surfaces to a state with no identifiable surfaces [1], and providing the potential for a perfectly bonded interface. Such a deceptively simple premise, this ideal forms the basis of the direct bonding technique [1-19], a stringent combination of surface preparation, cleaning, and contacting processes developed to bring two surfaces together at a few tens of nanometers such that they will be attracted by interatomic forces and caused to bond.

Using a combination of Van der Waals forces (attractive forces between molecules noticeable at atomic distances in the nanometer range) and other surface properties such as static electrical charges, adsorbed layers, and chemical interactions, a low-loss, seamless, vacuum tight interface can be created between explicit material layers, providing a multitude of structural possibilities and the basis of every experiment in this thesis. As such, this chapter provides an introduction to the direct bonding technique by describing the issues of surface preparation, the factors behind waveguide structure and design, and the fabrication processes which begin to explore the vast possibilities of this versatile technique. Two excellent reviews of semiconductor wafer direct bonding, by Haisma et al. [2] and Plößl et al. [3], cover much of the information described in this chapter, forming a fundamental basis upon which direct bonding at the Optoelectronics Research Centre was developed.

## 2.2 Features of Direct Bonding

Direct bonding incorporates many features that make the process ideal for waveguide design and fabrication [12-15]. In terms of optical propagation, the most important of these characteristics are the low losses exhibited by the boundary between each pair of bonded layers, as when prepared correctly two optical components can be

contacted across an atomically smooth interface [4]. Such an interface would show intrinsically low losses due to a lack of diffraction and absorption effects, and provide a potentially perfect boundary for optical waveguiding applications [5]. An intrinsically non-invasive technique, bonding materials by virtue of surface preparation alone also means that each layer can be made to retain the full characteristics of the original bulk material, even when polished down to waveguiding dimensions [13].

While direct bonding creates a seamless bond between two materials, many other techniques for joining components in both optical and semiconductor manufacturing processes require an adhesive layer between the composite materials. Such intermittent layers are often weak and prone to break down when run at high frequencies or temperatures, restricting the use of the eventual device. Diffusion of foreign atoms from the adhesive layer to the bonded samples, during high temperature annealing for example, can also increase propagation losses in the device due to added impurities and local changes in refractive index. Direct bonding can overcome these problems by forming a seamless, vacuum tight layer between two explicit material surfaces, joining the two pieces into one whole across an interface of similar strength to the chemical bonds within the bulk material layers [4].

Further applications of direct bonding include interfacial engineering, where the combination of many bonded regions within the same structure can be used to bury a specific layer of material [16-17]. Combining this effect with patterning, etching, and filling techniques, can also lead to buried structures of a three-dimensional nature. Perhaps the most powerful advantage of this fabrication technique though, is its ability to join combinations of samples from; monocrystalline, polycrystalline, amorphous, metallic or even composite (such as optical fibres) groups of materials [2-3]. The insensitivity of direct bonding towards the composition and morphology of the surface state also allows bonding across various crystallographic orientations and lattice constants [5]. This can be important for use with etch-stopping techniques for interface engineering, and also provides an advantage over other forms of monocrystalline multilayer creation, such as heteroepitaxial growth [2].

## 2.3 Pre-Bonding Conditions

While the credentials of the direct bonding technique are impressive, and seemingly ideal for the production of low-loss waveguide devices [5], several stringent physiognomic (geometrical, mechanical, physical, chemical, and thermal properties) pre-bonding conditions must be satisfied before the materials can be joined [1,4]. These production steps are relatively lengthy and expensive process when compared with adhesive bonding techniques, but are necessary to give the quality and compatibility of surface required for a stable, low-loss bonded interface.

Of paramount importance is the mechanical surface state of each sample, requiring that for every new type of material to be used for direct bonding a polishing technology must be developed to provide a smooth surface of ~ 2 nm peak to valley roughness (with a preferred value of approximately one atomic diameter (~ 0.5 nm peak to valley roughness) [4]). Such an atomic scale roughness is particularly important for bonded surfaces that incorporate a hydrophilic treatment (Section 2.4) as hydrogen bonds can only form across an interface of one atomic diameter. Precautions must also be taken during mechanical polishing to reduce the effects of plastic deformation and crystallographic damage of the material in the sub-surface layer, as these effects can result in damage and optical losses at the interfacial boundary [1]. In addition, the geometrical shape of each sample must be considered, as the complementarity of curvature between the two surfaces has to be accurate to a high degree. Shape deviations across the entire sample surface must be less than 50 nm if a uniform bond is to be produced throughout [2], although thinner samples with higher elasticity can help reduce this requirement slightly. Direct bonding is therefore best suited to thin, flat bodies.

The chemical surface state of each sample is also important, as direct bonding requires the surface of each material to be exceptionally clean. This includes the removal of all organic, inorganic, and chemical based foreign bodies from each polished sample [3]. Some materials also require a chemical treatment in order to activate them for direct bonding and increase the potential bonding energy of ambient surface forces. Such treatments are usually hydrophilic in nature and can increase bond strength by approximately one order of magnitude [6].

Required interfacial strength and the thermomechanical properties of contacted materials must be also considered, as a bonded interface will usually require high temperature annealing to strengthen it sufficiently for further processing [2-3]. Such heat treatments form an integral part of the direct bonding technique, and determination of the temperature required to anneal each pair of materials is performed in relation to bond strength. This process utilises two rods, glued to the top and bottom of the bonded sample, to apply a pulling force to the interface in order to break the annealed surfaces apart along the join [12]. When the applied annealing temperature has proved sufficient, breakage will occur throughout the bonded sample in bulk, indicating that the two materials are no longer distinguishable as separate pieces. The choice of a suitable pair of materials for direct bonding is therefore highly dependant on the bond strength required for further processing as, for high temperature annealing, materials with well matched thermomechanical properties are needed for the bond to remain stable during the heating process. As such, researching materials with similar thermal expansion coefficients and compatible refractive indices is a large part of waveguide design in direct-bonded optical devices.

## 2.4 The Hydrophilic Treatment

By treating each material in a suitable aqueous environment the polished surfaces for direct bonding can be rendered hydrophilic [6]. This treatment provides each surface with a layer of OH groups that will, under ambient conditions, adsorb a monolayer of water molecules. After the materials are contacted, these water molecules and OH groups become trapped at the interface, allowing hydrogen bridges to form between the two surfaces. Hydrogen bonds are analogous to covalent bonds (in which an electron pair binds two positively charged structures), allowing a proton ($H^+$ ion) to come between two atoms, polarizing them and attracting them by means of the induced dipoles [6]. This chemical treatment helps to increase the bonding energy, and thus the overall interface strength, between the two materials.

The strengthening effects of a hydrophilic treatment can best be understood by taking a closer look at the direct-bonded interface itself (Figure 2.1). Because the two surfaces will not be perfectly flat on an atomic scale, there are parts of the interface where, at the moment of bonding, hydrogen links cannot be formed between the water

molecules adsorbed at the surfaces. However, once the initial bond has formed, water molecules will diffuse to those regions where the gap between the surfaces is too large for hydrogen bonding. This diffusion enlarges the effective area across which hydrogen bonds can form and thus increases the bond energy. A theoretical calculation of the contribution that hydrogen bonds add to the bonding energy between two surfaces can be performed based on a theoretical model of the monolayer of water, as described in Reference [6]. The results of such a calculation show that the bonding energy of a hydrophilic treated direct-bonded interface is 0.104 J $m^{-2}$, an increase of over one order of magnitude when compared with the bonding energy provided by Van der Waals forces alone (0.0075 J $m^{-2}$). However, it should be noted that while a hydrophilic treatment can significantly increase the strength of a bonded interface, such a technique is unlikely to provide the interfacial strength required for further mechanical processing (such as sawing and polishing). Therefore, a high temperature annealing treatment is often used to further increase the interfacial bonding energy, attaining a value close to that of purely chemical bonds in the original materials [2-3].

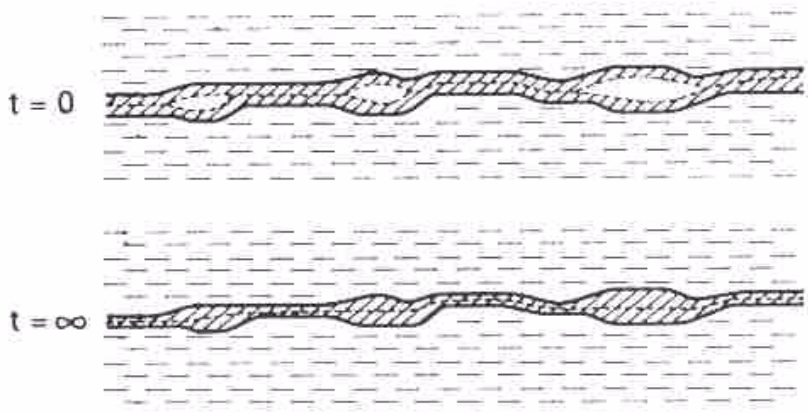


**Figure 2.1**: Schematic representation of the interface between two direct bonded materials depicting the formation of hydrogen bonds across the sample interface, as illustrated in Reference [6].

## 2.5 Adhesive avalanche

Once the materials for bonding have been chosen, shaped, polished, and cleaned, they are ready for direct bonding. Contacting of the two surfaces occurs spontaneously at room temperature in ambient conditions, although a dedicated clean environment is recommended if optimum surface condition is to be maintained. The mechanisms behind the direct bonding process begin when the samples are prepared in a hydrophilic treatment and positioned with their polished surfaces in parallel. A

combination of gravitational and applied forces cause the samples to approach one another to within such a short distance (tens of nanometers) that attractive Van der Waals forces (interactions caused by fluctuating charge distributions and electric dipole moments between neighbouring atoms, noticeable even when no permanent dipole moment is present [6]) start to draw the surfaces together [2]. At a critical distance of some tenths of a nanometer, adhesive avalanche [1] occurs and the two polished surfaces snap together. In this adhesive avalanche an initially small bonded area is formed where the surfaces are in atomic contact. This initial bond is defined by a structural transition from a system containing two surfaces to a state with no identifiable surfaces [1]. As larger parts of the surfaces are drawn together the size of the bonded region increases at a linearly constant rate and air is expelled from the gap between the two samples [3]. What results is a direct-bonded interface akin to one large grain boundary between the two material layers [4]. Once the surfaces are in atomic contact, hydrogen bonds form across the interface to increase the strength of the bonded region and after a suitable annealing treatment the direct-bonded sample will be ready for further processing.

## 2.6 The direct bonding technique

Based on techniques developed for use in the semiconductor industry [2-3], the fabrication process outlined in this section describes a direct bonding technique derived by the author for use with the materials, polishing, and cleaning facilities available at the Optoelectronics Research Centre of the University of Southampton. This technique has been used in the preparation of both glass and crystal substrates for use in a diverse range of direct-bonded structures and devices, the primary results and applications of which are presented in Chapters 3 to 6.

The direct bonding process is performed in several phases (Figure 2.2), beginning with the surface preparation of each substrate layer. To ensure surface compatibility, a diamond-edged circular saw is used to dice the bulk materials into complementary shapes with relative surface areas and thickness as required. Surface polishing is then accomplished in two stages, featuring an initial mechanical lapping step (incorporating the use of 9 μm and 3 μm calcined aluminium oxide slurries in turn), followed by a chemical polishing treatment of syton (an aqueous alkaline solution

containing suspended nanoparticles of silica [2]) to leave each surface with an optical finish. It has been noted that for optimum reproducible direct bonding performance, the final thickness of each polished sample should be ~ 500 μm or less (although samples as thick as 2 mm have been successfully bonded with no interfacial voids).

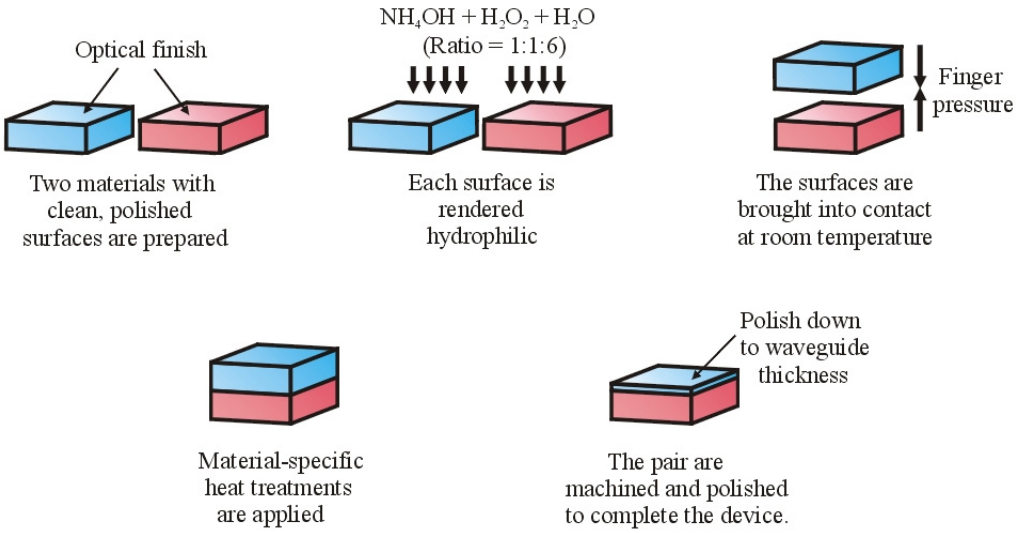


**Figure 2.2**: Schematic representation of the major steps in the Direct Bonding process.

Cleaning of each polished surface begins with an Ecoclear™ (a solvent designed by specifically for wax removal) treatment in which the sample is left to soak overnight and then gently scrubbed with an acetone rinsed cotton bud to remove any large traces of dirt and mounting wax remaining from the polishing step. The samples are then treated in a succession of chemicals (ecoclear, acetone, isopropanol, microclean detergent, and two water rinses) for twenty minutes at a time in an ultrasonic bath at 50 °C. Surface cleanliness is then checked under a microscope at 20× magnification, with any residual dirt or wax (if present this is usually soft, mobile, and found near the edges of the sample) being easily removed with a cotton bud. To increase eventual bond strength and uniformity, the samples are then placed into a mixture of ammonium hydroxide ($NH_4OH$), hydrogen peroxide ($H_2O_2$), and water ($H_2O$), at a ratio of 1:1:6 for ten minutes [13], followed by a de-ionised water rinse for four minutes, a treatment which renders the polished surfaces hydrophilic. After removal from the water the samples are contacted in parallel at room temperature and held in position until adhesive avalanche takes place.

Contact between clean, polished materials has been performed successfully by three methods, giving a variety of bonding times and results. The first technique uses a dry surface method, wherein both samples are blown dry with an inert gas supply before they are contacted. Experimentally impressive, when brought into close proximity the two surfaces literally snap together to bond *instantaneously*. While capable of forming void-free interfaces, this process negates any chance of repositioning the two samples if an alignment error occurs. In direct contrast, the second experimental method used to contact surface-ready samples is performed directly after the hydrophilic water rinse and involves placing the two materials in parallel while they are still wet. This technique allows for lengthy positioning of the two layers with relation to one another as it takes time (as long as ten minutes) for the excess liquid to dissipate from the boundary at room temperature. Finger pressure must be applied to maintain the position of each sample and promote bonding, but the slippage caused by the intermittent water layer can result in the forming and breaking of small bonded regions along the interface (Figure 2.3), an effect which can cause surface damage to both samples before adhesive avalanche takes place. As an effective compromise, the most versatile contacting technique used in these experiments to date combines elements of the wet and dry contacting processes to allow the formation of void-free interfaces between selectively aligned substrate layers. This is implemented by leaving a small amount of liquid on one sample while drying the other completely, creating a thin layer of water that can be squeezed between the contacted surfaces and provide a short time for sample alignment. Once in position, blow-drying and applied pressure can be used to remove this liquid layer from between the samples, inducing

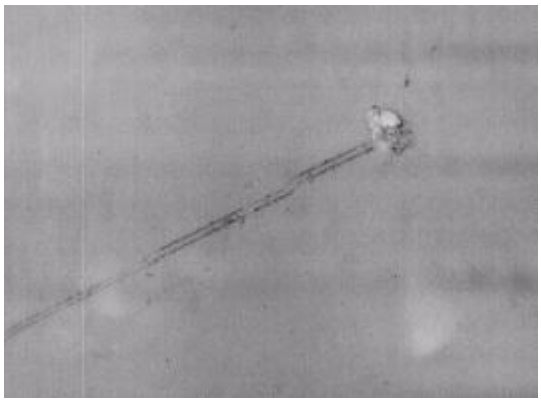

**Figure 2.3**: A photograph of bonding damage caused by movement during wet sample alignment (50x magnification). As demonstrated by this picture, sample motion has caused a small bonded area to break away from the surface (top right in the picture), causing scratches as it is dragged along between the material layers.

adhesive avalanche and removing trapped moisture at the sample interface. This technique has been employed successfully to produce void free interfaces in well-aligned crystal and amorphous materials, and bonded interfacial areas of up to 3 cm × 5 cm have been produced within the scope of this project.

In order to promote strength and uniformity across the bonded interface two subsequent methods of heat treatment have been developed, tailored for the specific characteristics of the materials involved. For example, ferroelectric materials (such as $LiNbO_3$ and $LiTaO_3$) can be placed directly into a 120 °C oven after their surfaces have been contacted to induce a sudden increase in temperature of the crystals. The resulting pyroelectric effect [18] causes a build-up of static charge on the surfaces of each crystal that will (provided each layer is aligned along a similar crystalline orientation) pull the two layers together rapidly and eliminate any remaining voids from the interface. This effect is visible by the removal of interference fringes from the unbonded sections of material. Alternatively, materials such as glass should be left at room temperature for a few days to allow the formation of hydrogen bonds between the contacted surfaces (this has been recorded to take as long as 100 hours in direct-bonded silicon substrates [1]) before being placed into a 120°C oven to dry out thoroughly. The latter process is performed to remove any excess water absorbed by the materials during the cleaning and hydrophilic treatments, as expansion of such liquids during high temperature annealing can cause sample damage.

Completion of each sample involves annealing the bonded interface at a temperature specific to the materials used and strength required for further processing. This step usually begins with a process of trial and error for each new material, with successively higher temperatures being applied until bond strength is sufficient to allow precision polishing of the waveguiding layer down to a pre-determined thickness. As a buried structure is often advantageous for optical waveguide devices, additional cladding layers can be added with the same technique. Once completed, the direct-bonded sample can then be diced and end-face polished as necessary, and Table 2.1 provides a summary of results for the materials investigated during this project.

| Material | | Bonds at 25°C? | Annealing Temp. (°C) | Notes | Result |
|---|---|---|---|---|---|
| Core | Cladding | | | | |
| $LiNbO_3$ (+z) | $LiNbO_3$ (-z) | ✓ | 300 | Bonded uniformly for crystal thickness of 1mm or less and surface areas up to that of a 3 inch diameter wafer. | Section 2.7 |
| $LiNbO_3$ (+z) | $LiNbO_3$ (+z) | ✓ | 300 | Bonds well but pyroelectric effect cannot be used to improve contact. | Section 7.3 |
| $LiNbO_3$ (-z) | $LiNbO_3$ (-z) | ✓ | 300 | As above. | - |
| $LiNbO_3$ (+x) | $LiNbO_3$ (-z) | ✓ | × | Bonded interface does not survive at temperatures above 100 °C and is not strong enough to allow polishing. | - |
| PPLN | $LiTaO_3$ | ✓ | 300 | Bonded uniformly over surface areas of several square centimetres, with interfacial strength allowing polishing to a few μm. | Chapter 3 |
| Fe:$LiNbO_3$ | MgO:$LiNbO_3$ | ✓ | 300 | High temperature annealing causes a degrading ion-exchance mechanism between the two substrate layers. | Chapter 4 |
| $LiNbO_3$ | MgO:$LiNbO_3$ | ✓ | × | Bonded interface does not survive at temperatures above 100 °C and is not strong enough to allow polishing. | - |
| $LiNbO_3$ | quartz | ✓ | × | As above. | - |
| Nd:BK-7 | BK-7-type | ✓ | 350 | Annealing causes ion-exchance between the two substrate layers providing a novel route towards waveguide fabrication. | Chapter 5 |
| Nd:SGBN | BK-7-type | ✓ | 350 | As above. | Chapter 6 |
| Er:SGBN | BK-7-type | ✓ | 350 | As above. | - |
| F2 | F7 | ✓ | 350 | Bonds well over large areas to give a passive planar waveguide structure. | - |

**Table 2.1:** A summary of direct bonding experiments and results investigated during the scope of this project. Annealing temperatures represent the minimum temperature required to provide interfacial strength suitable for polishing down to waveguide dimensions, and more information can be found on each experiment in the referenced chapters.

## 2.7 Interfacial characteristics of direct-bonded lithium niobate

Before creating direct-bonded PPLN waveguides for use in frequency-doubling experiments (Chapter 3), several preliminary tests were performed with single-domain lithium niobate substrates. The original samples investigated were 500-μm-thick and used as prepared by the supplier (Crystal Technologies) such that the initial dicing and polishing stages of direct bonding were ignored. A variety of contacting methods were used to successfully bond several $LiNbO_3$ samples, the most dramatic being when both samples were dried after the hydrophilic treatment and the two pieces spontaneously snapped together. However, whether the samples are wet or dry before contact, unbonded spots can occasionally form at the interface. These spots were originally attributed to trapped moisture between the layers (the unbonded regions expand as a result of applied heat indicative of an expanding gas trapped between the two surfaces), but a recent review of wafer-direct-bonding by Plößl and Kräuter [2] cites hydrogen (trapped at the surface as an integral part of the hydrophilic

treatment [10]) as the cause for similar unbonded spots in direct-bonded silicon wafers. As such, the overall cause for this problem is likely to be slight deviations in the quality of each polished surface when supplied, prompting several tests to assess the quality and strength of each bonded interface.

When contacted, the $LiNbO_3$ samples used in preliminary testing were positioned such that the x-, y-, and z-axis of each crystal were aligned in parallel. Annealing of these direct-bonded samples was performed at 300 °C for one hour, a previously reported time and temperature required to create bond energies comparable to those within the internal $LiNbO_3$ crystal structure [19]. As a test of interfacial strength, extreme force was applied to one of these direct-bonded samples until it eventually fractured, the result of which is shown in the photograph of Figure 2.4. Rather than cracking along the direct-bonded interface (the interface runs horizontally in the picture starting from the ledge at the upper left), it can be seen that the sample has broken in bulk, preferring instead to shear through the bonded structure. This effect shows that the annealed bond has fused the two separate crystals into a single whole, gaining sufficient interfacial strength to resist further processing.

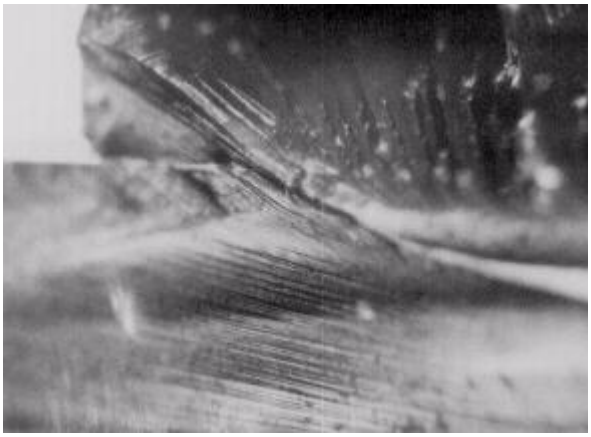

**Figure 2.4**: The interface of a shattered pair of lithium niobate substrates contacted by direct bonding. After a heat treatment of 300 °C for 1 hour, this sample has gained an interfacial strength similar to that of the chemical bonds within a single lithium niobate crystal.

Additional assessment of the direct-bonded interface between two $LiNbO_3$ samples was performed using transmittance measurements from a spectraphotometer. In general, the intensity loss of an optical beam at each surface of a $LiNbO_3$ sample is around 14% (due to Fresnel reflection), although this changes slightly with the wavelength of the incident light. As these losses are surface dependent, this would

suggest that if the light is directed through a direct-bonded pair of $LiNbO_3$ crystals, perpendicular to the interface, any additional losses to those suffered by a single $LiNbO_3$ sample would be due to gaps at the bonded interface. In a worst-case scenario it could be assumed that the interface between two direct-bonded layers is not contacted at all (retaining the loss characteristics of two separate interfaces), with a transmittance versus wavelength curve that emulates two separate $LiNbO_3$ samples held in parallel. Therefore, a test of the direct-bonded interface integrity was performed by comparing the transmittance characteristics of three $LiNbO_3$ configurations; a single $LiNbO_3$ piece, two pieces of $LiNbO_3$ pressed together, and a direct-bonded $LiNbO_3$ pair, throughout the visual range of wavelengths of light.

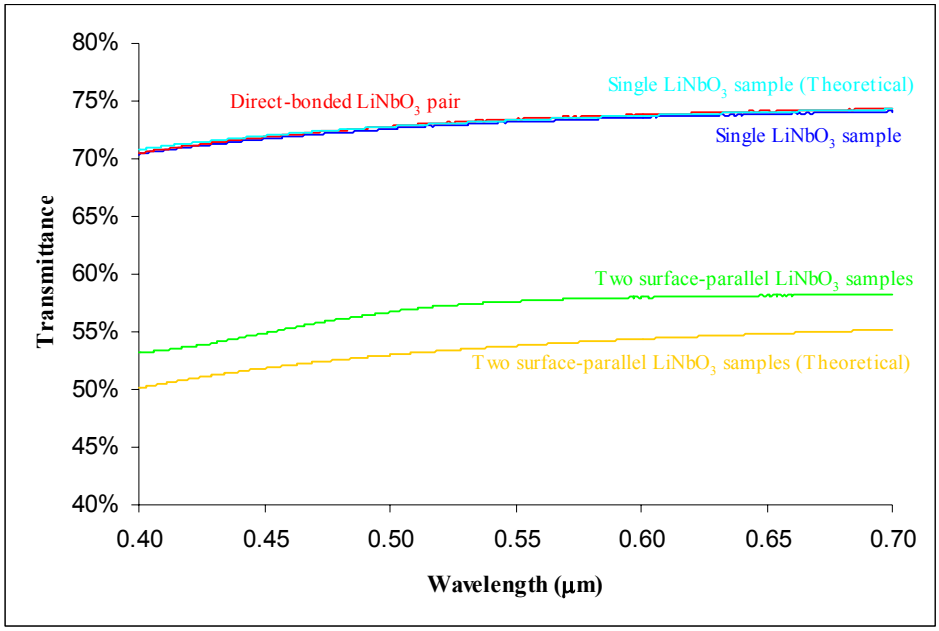


**Figure 2.5**: Transmittance characteristics of three lithium niobate configurations: a single substrate, two substrates held together in parallel, and a direct bonded pair of $LiNbO_3$ substrates. Measurements were taken perpendicular to the surface of each sample and feature a transmittance error of ± 0.01 %. Theoretical curves are based on a 14 % transmission loss due to the Fresnel reflection at each sample surface (Section 3.8), and the disparity between theory and measurement for the case of two surface-parallel crystals is likely to be due to close proximity interference effects during testing.

The graph of Figure 2.5 demonstrates that the transmittance of a direct-bonded pair of $LiNbO_3$ samples and that of a single sample are approximately equal, whereas the loss at the unbonded interface of two parallel lithium niobate samples is substantially higher. This result demonstrates that the two explicit $LiNbO_3$ samples have been fused into a single whole by direct bonding (eliminating the two internal interfaces

completely) to produce a seamless, multi-layered structure with low interfacial losses, and a good basis for the experiments described in the following chapters.

## 2.8 Waveguide theory for direct-bonded devices

Having developed the fundamental techniques required for creating direct-bonded structures, the remainder of this Chapter discusses the application of direct bonding technology to the field of waveguide fabrication and design. The majority of waveguide structures produced by direct bonding [20-26] consist of three dielectric layers; a core region of high refractive index, $n_1$, surrounded by substrate and cladding layers with lower refractive indices $n_2$ and $n_3$ respectively, the fundamental properties of which are illustrated in Figure 2.6. The most generally examined case is the asymmetric waveguide, where $n_2 > n_3$, and waveguide theory governing the propagation of light in such a structure is described in several textbooks [27-31]. In this section, the theoretical discussion follows closely from that presented by Lee in Reference [27] and is applied towards the basic design factors used to create a direct-bonded planar waveguide device, from the choice of material layers with suitable refractive indices to the optimisation of the geometry and dimensions of the waveguide core, and how these are related to previously discussed aspects of fabrication, such as interfacial strength. Particular attention is paid to the example of a direct-bonded waveguide structure based on lithium niobate and lithium tantalate crystal layers (as described in the next chapter), although a similar methodology can be applied to the other devices described in this Thesis.

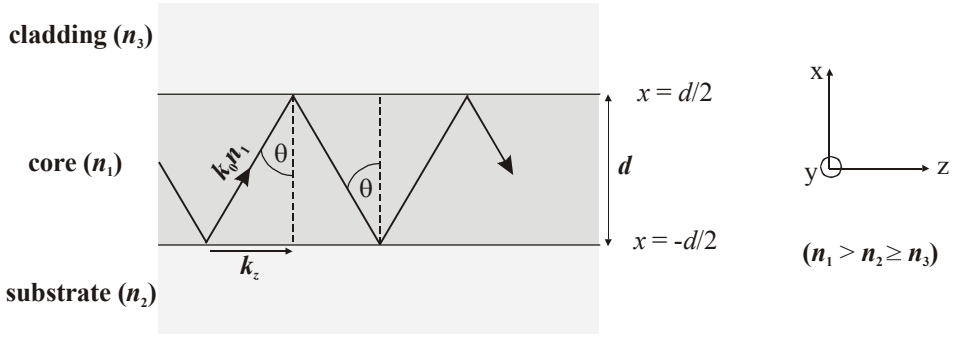


**Figure 2.6:** Fundamental properties of an asymmetric waveguide structure, including the ray interpretation for light propagation along the core of the waveguide [27]. The substrate and cladding layers of the waveguide are assumed to be of infinite thickness.

The propagation of a coherent beam of light along the core of a planar waveguide is illustrated in Figure 2.6. The light travels along the *z*-direction of the structure and is confined within the waveguide via total internal reflection at both the core-substrate and core-cladding boundaries of the device, implying that the angle of propagation, $\theta$, must be greater than the critical angle, $\theta_c$, for each interface [27]. In an asymmetric waveguide configuration, where the critical angle is greater at the core-substrate boundary, this means that the angle of propagation must be larger than $\theta_c = \sin^{-1}(n_2/n_1)$ if the light is to travel along the core of the device [27]. Under such conditions the light is said to be travelling in a guided waveguide mode, and is defined as an electromagnetic field distribution that maintains the same transverse distribution and polarisation state at all distances along the waveguide axis [27]. Subsequent theory is often presented in terms of a propagation constant related to the optical path length travelled by the guided mode [28]

$$k_z = k_0 n_1 \sin\theta \tag{2.1}$$

where $k_0 = 2\pi/\lambda$ ($\lambda$ is the freespace wavelength of the light) and the quantity $n_1 \sin\theta$ is described as the effective refractive index of the mode, $n_{eff}$. Taking values in the range of $n_1$ to $n_2$ (representing the limits of guided propagation: $90° > \theta > \theta_c$), the effective refractive index provides a simple insight into the guiding conditions within the waveguide structure, as when $n_{eff}$ is close to $n_1$ ($\theta \Rightarrow 90°$) the light is well confined within the waveguide core with very little penetration into the substrate or cladding layers, while if $n_{eff}$ approaches $n_2$ ($\theta \Rightarrow \theta_c$) then the fraction of light confined within the core reduces until eventually no guidance takes place [28].

While the 'bouncing beam' interpretation of Figure 2.6 gives a good description of fundamental terms and an intuitive explanation for the propagation of light in a waveguide, a more thorough analysis of modal characteristics can be performed using electromagnetic theory based on derivations from Maxwell's equations, as presented in References [27,29]. Here, the discussion will be limited to the propagation of TE modes (where the electric field component is polarised along the *y*-direction) in a one-dimensional waveguide format, but a similar methodology can also be applied to find the TM modes (magnetic field polarised along *y*), and to describe modal propagation in other waveguide geometries [27]. The form of the field distribution for TE modes in the asymmetric waveguide, $E_y$, is assumed to have an oscillatory (guided)

behaviour in the core and exponentially decaying fields in the substrate and cladding regions of the device such that [27]

$$E_y(x,z) = \begin{Bmatrix} A_3 e^{-\alpha_{3x}x} \\ A_1 \cos(k_{1x}x + \psi) \\ A_2 e^{+\alpha_{2x}x} \end{Bmatrix} e^{-ik_z z} \qquad \begin{matrix} x > d/2 \quad (cladding) \\ |x| \le d/2 \quad (waveguide) \\ x < -d/2 \quad (substrate) \end{matrix} \tag{2.2}$$

where $\psi$ is a phase constant describing waveguide asymmetry, and $k_{1x}$, $\alpha_{2x}$, and $\alpha_{3x}$ are transverse wavenumbers defined by the appropriate dispersion relation in each region of the waveguide [32];

$$k_{1x} = k_0 \sqrt{n_1^2 - n_{eff}^2}\,, \tag{2.3}$$

$$\alpha_{2x} = k_0 \sqrt{n_{eff}^2 - n_2^2}\,, \tag{2.4}$$

$$\text{and} \quad \alpha_{3x} = k_0 \sqrt{n_{eff}^2 - n_3^2}\,. \tag{2.5}$$

Elimination of the unknown amplitude coefficients $A_1$, $A_2$, and $A_3$ is performed by applying boundary conditions at the two interfaces of the structure ($x = \pm d/2$) and satisfying the requirement of tangential continuity for the electric- and magnetic-field components of the guided mode across those boundaries [27]. The result is an eigenvalue equation that determines the guidance condition in the waveguide, which is usually expressed in the form [28]:

$$\tan(k_0 n_1 d \cos\theta - m\pi) = \sqrt{\frac{n_1^2 - n_3^2 - n_1^2\cos^2\theta}{n_1^2\cos^2\theta}} + \sqrt{\frac{n_1^2 - n_2^2 - n_1^2\cos^2\theta}{n_1^2\cos^2\theta}} \tag{2.6}$$

where $d$ is the core thickness and $m$ is an integer value representing the mode number. A transcendental equation with no analytical solution, subsequent information regarding the propagation characteristics of guided modes described in Equation 2.6 must be found numerically or graphically [28]. Figure 2.7 provides examples of the graphical solution for determining the number and propagation angle of guided modes in waveguides based on lithium niobate (core) and lithium tantalate (substrate) crystal layers, where in each graph the left- and right-hand sides of Equation 2.6 are plotted as functions of $\cos\theta$ and solutions found where the curves intersect [28]. It is important to note that the solutions of Equation 2.6 do not describe a continuous range of angles but are instead limited to a discrete set of values, each representing a different path of guided propagation, and thus an independent mode of the waveguide [27]. The examples presented demonstrate that the three basic factors which

determine the number of guided modes in a given waveguide structure are the refractive index profile, the thickness of the core layer, and the wavelength of the guided light, and that the condition for cutoff (where the propagation angle of the light becomes so small that it is no longer guided) is determined by wavelength and waveguide asymmetry [28].

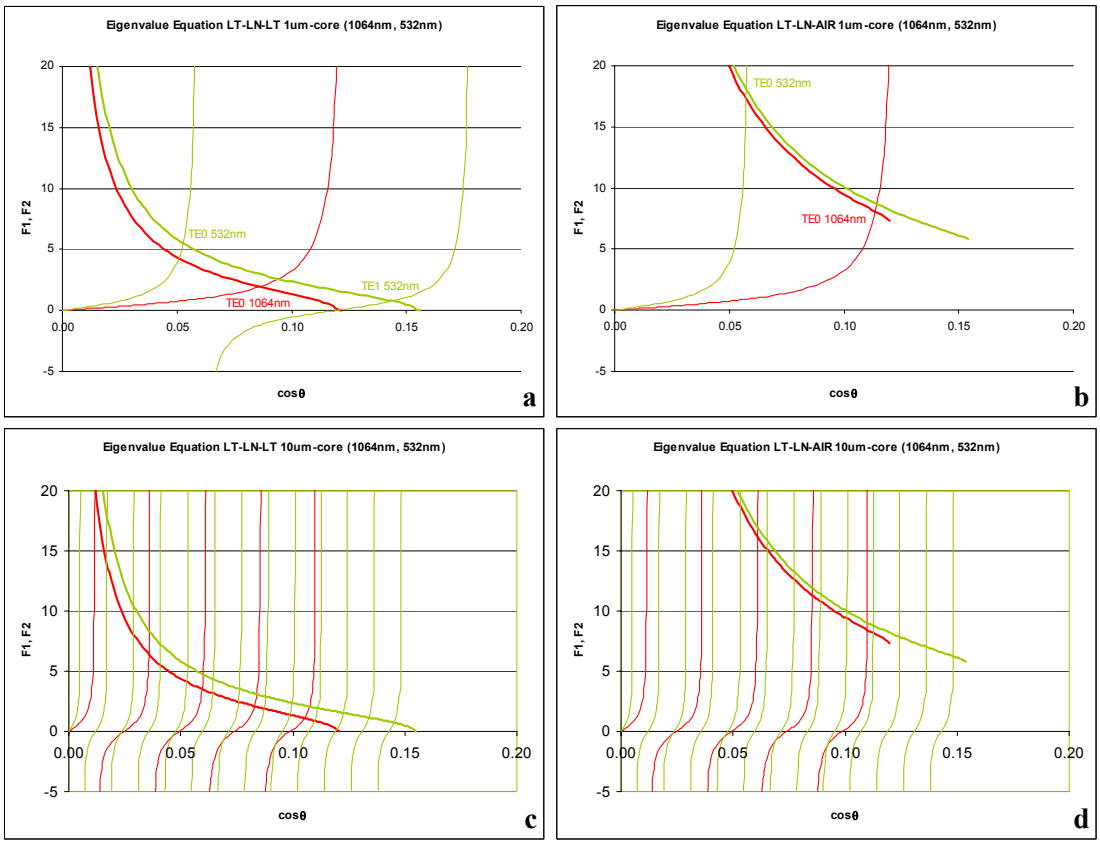


**Figure 2.7:** Solutions of the Eigenvalue equation guidance condition (Equation 2.6) for two waveguide types based on a lithium tantalate substrate layer with lithium niobate core and either; a,c) lithium tantalate (symmetric), or b,d) air (asymmetric) cladding materials. Examples a and b represent waveguides with a 1μm-thick-core layer, while c and d feature 10-μm-thick core sizes. Red and green lines represent solutions for freespace wavelengths of 1064 nm and 532 nm respectively, where thick lines represent the right-hand side of Equation 2.6 as a function of $\cos\theta$ and the thin lines the left. Refractive indices for lithium niobate and lithium tantalate at each given wavelength are calculated by use of the Sellmeir equations discussed in Section 3.7 [33].

As it would be very time consuming if repeated graphical solutions had to be obtained for a waveguide model whenever the propagation wavelength, thickness, or refractive indices of the design were changed, these variables can be combined into three normalised parameters applicable to a large number of waveguide geometries [27]. These are a frequency parameter normalised to film thickness, $V$, a normalised refractive index parameter, $b$, and an asymmetry measure, $a$, as defined by [31];

$$V = k_0 d\sqrt{n_1^2 - n_2^2}\,, \tag{2.7}$$

$$b = \frac{n_{eff}^2 - n_2^2}{n_1^2 - n_2^2}, \tag{2.8}$$

and $$a = \frac{n_2^2 - n_3^2}{n_1^2 - n_2^2}\,. \tag{2.9}$$

By substituting the limits of the effective refractive index ($n_1 \geq n_{eff} \geq n_2$) into the normalised refractive index parameter, the range of values that $b$ can take lies between zero and one, with higher values demonstrating stronger guidance and $b = 0$ representing the cutoff condition for a particular mode [28]. Values of the asymmetry measure range from zero in a symmetrical waveguide structure (where $n_2 = n_3$) towards infinity in the limit of very strong asymmetry ($n_2 >> n_3$). Combining these normalised parameters to provide knowledge of the effective refractive index as a function of frequency then leads to the desired information about modal propagation and dispersion in a planar waveguide device, and can be achieved via a rearrangement of the guidance condition of Equation 2.6, to give [27]:

$$V\sqrt{1-b} = m\pi + \tan^{-1}\sqrt{\frac{b+a}{1-b}} + \tan^{-1}\sqrt{\frac{b}{1-b}}\,. \tag{2.10}$$

Solutions to this equation are again found graphically and are typically obtained from a normalised graph of $V$ versus $b$ [27], an example of which is given in Figure 2.8. The graph is generated using values between zero and one for the normalised

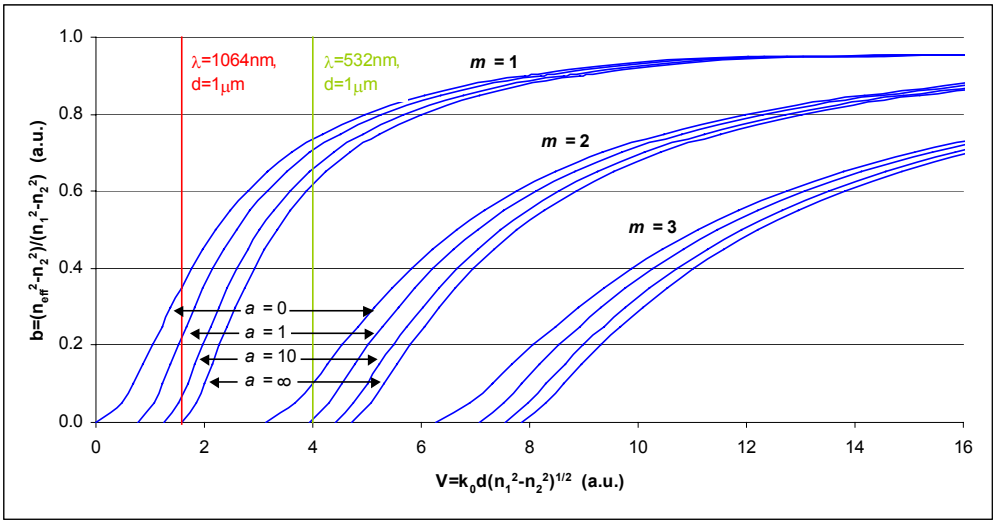


**Figure 2.8:** Normalized $b$ vs. $V$ diagram for a planar waveguide with lithium niobate core and lithium tantalate substrate layers. Examples for the first three modes of propagation and a range of waveguide asymmetries are presented, including solutions for wavelengths of 1064 nm and 532 nm in a waveguide with a 1-μm-thick core region.

refractive index parameter, integer values of $m$ to represent the different possible modes of propagation, and a calculated asymmetry parameter determined by waveguide geometry. Intersection points with the calculated $V$ number for a given wavelength (determined using Equation 2.7) provides information regarding the number of modes and dispersion characteristics of the waveguide, while the corresponding values of $b$ give the effective refractive index and angle of propagation.

Having solved the guidance condition for a given waveguide structure, the transverse electric field profile, $E_y(x)$, for each guided mode can be determined by applying the discrete angle of propagation for that mode, $\theta_m$, to find values for $n_{eff}$, $k_{1x}$, $\alpha_{2x}$ and $\alpha_{3x}$, and a subsequent solution to Equation 2.2. A value for the phase constant, $\psi$, is calculated from the relation [27]

$$2\psi = \tan^{-1}\left(\sqrt{\frac{n_1^2 - n_3^2 - n_1^2\cos^2\theta_m}{n_1^2\cos^2\theta_m}}\right) - \tan^{-1}\left(\sqrt{\frac{n_1^2 - n_2^2 - n_1^2\cos^2\theta_m}{n_1^2\cos^2\theta_m}}\right) \qquad (2.11)$$

which equals zero for a symmetric waveguide and increases with waveguide asymmetry to represent an offset of optical confinement towards the core-substrate interface [28]. Transverse electric field profiles for the above examples of lithium-niobate-based waveguide structures with a 1-μm-thick core are presented in Figure 2.9. The electric field profiles are normalised by setting the amplitude coefficient $A_1$ to a have value of 1, and then selecting $A_2$ and $A_3$ to maintain a continuous field across the interfacial boundaries of the waveguide [28]. The nomenclature TE$m$ is used to label the TE modes via the number of zeros in each profile, where TE0 represents the first-order mode of the waveguide, TE1 the second, and so on [28].

From the graphs of Figure 2.9 it is apparent that the degree of penetration of the transverse electric field into the substrate and cladding regions of the waveguide is wavelength dependent [28]. As the refractive indices of these regions are different to that of the core, it also follows that the effective refractive index encountered by the mode is wavelength dependent, resulting in dispersion [28]. With a clear difference in profile for the first-order modes in symmetric and asymmetric waveguides (from near-Gaussian in the symmetric case to the distorted asymmetric profile), it can also be seen that an asymmetric geometry can lead to a poor overlap of the transverse

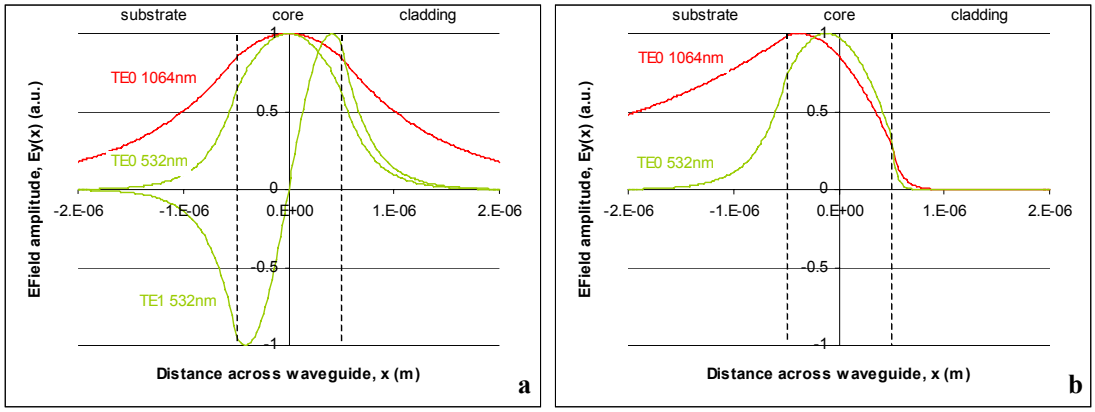


**Figure 2.9:** Transverse electric field profiles for TE modes in; a) a symmetric waveguide with a 1-µm-thick lithium niobate core region surrounded by lithium tantalate substrate and cladding regions, and b) an asymmetric waveguide based on a 1-µm-thick lithium niobate core with a lithium tantalate substrate and air as the cladding material. The fields are normalised to have a maximum value of $E_y$ = 1, and red and green lines represent solutions for propagation wavelengths of 1064 nm and 532 nm respectively. It should be noted that in the special case of a symmetric waveguide, the transverse electric field profiles for 'odd' order modes (TE1, TE3, TE5, etc.) are determined by replacing the cos function of Equation 2.2 with a sin function [27].

electric field profiles of a propagating mode at different wavelengths [32]. In an interaction that is dependent on more than one wavelength, such as the process of second harmonic generation described in Chapter 3, or the laser action discussed in Chapters 5 and 6 for example, this effect becomes particularly important as the operational efficiency of an active waveguide device largely depends on the modal size and overlap of the fundamental and signal beams, and the related intensity distribution in the waveguide [34]. As such, when designing such a device it is often advantageous to apply a symmetric (or near-symmetric) waveguide geometry that supports just a single mode at both the fundamental and signal wavelengths, ensuring a good overlap for high intensity interactions between the two. As most single-mode optical waveguide structures require a core thickness of just a few microns, fabrication of such devices by direct bonding therefore requires high interfacial strength and a precisely reproducible polishing process (obtaining surface parallelism across a bonded core layer of less than 10-µm-thick is not a trivial task), the development of which for a variety of materials and processes is presented in the following chapters.

## REFERENCES

[1] J. Haisma, G. A. C. M. Spierings, T. L. Michielsen, and C. L. Adema, "*Surface preparation and phenomenological aspects of direct bonding*", Philips Journal of Research, Vol. 49, p.23-46 (1995).

[2] J. Haisma, G. A. C. M. Spierings, U. K. P. Biermann, and A. A. van Gorkum, "*Diversity and feasibility of direct bonding: a survey of a dedicated optical technology*", Applied Optics, Vol. 33, No. 7, p.1154-1169 (1994).

[3] A. Plößl and G. Kräuter, "*Wafer direct bonding: tailoring adhesion between brittle materials*", Materials Science and Engineering, Vol. R25, 1-2, p.1-88 (1999).

[4] J. Haisma, G. A. C. M. Spierings, and T. L. Michielsen, "*Frameworks for direct bonding*", Philips Journal of Research, Vol. 49, p.11-21 (1995).

[5] J. Haisma, "*Direct bonding: retrospect and outlook*", Philips Journal of Research, Vol. 49, p.171-177 (1995).

[6] G. A. C. M. Spierings, J. Haisma, and T. L. Michielsen, "*Surface related phenomena in the direct bonding of silicon and fused-silica wafer pairs*", Philips Journal of Research, Vol. 49, p.47-63 (1995).

[7] U. K. P. Biermann, A. A. van Gorkum, and J. A. Pals, "*Direct bonding: from an optical technology to a broad research topic*", Philips Journal of Research, Vol. 49, p.1-10 (1995).

[8] J. Haisma, T. M. Michielsen, and F. J. H. M. van der Kruis, "*Silicon-wafer fabrication and (potential) applications of direct-bonded silicon*", Philips Journal of Research, Vol. 49, p.65-89 (1995).

[9] G. A. C. M. Spierings, J. Haisma, and F. J. H. M. van der Kruis, "*Direct bonding of organic polymeric materials*", Philips Journal of Research, Vol. 49, p.139-149 (1995).

[10] J. Haisma, J. J. C. Groenen, and P. W. de Haas, "*Non-silicon applications of direct bonding*", Philips Journal of Research, Vol. 49, p.151-163 (1995).

[11] J. Haisma, "*Direct bonding in patent literature*", Philips Journal of Research, Vol. 49, p.165-170 (1995).

[12] Y. Tomita, M. Sugimoto, and K. Eda, "*Direct bonding of $LiNbO_3$ single crystals for optical waveguides*", Applied Physics Letters, Vol. 66, No. 12, p.1484-1485 (1995).

[13] K. Eda, M. Sugimoto, and Y. Tomita, "*Direct heterobonding of lithium niobate onto lithium tantalate*", Applied Physics Letters, Vol. 66, No. 7, p.827-829 (1995).

[14] C. T. A. Brown, C. L. Bonner, T. J. Warburton, D. P. Shepherd, A. C. Tropper, and D. C. Hanna, "*Thermally bonded planar waveguide lasers*", Applied Physics Letters, Vol. 71, No.9, p.1139-1141 (1997).

[15] S. Pélissier, F. Pigeon, B. Biasse, M. Zussy, G. Pandraud, and A. Mure-Ravaud, "*New technique to produce buried channel waveguides in glass*", Optical Engineering, Vol. 37, No. 4, p. 1111-1114 (1998).

[16] R. Egloff, T. Letavic, B. Greenberg, and H. Baumgart, "*Evaluation of strain sources in bond and etchback silicon-on-insulator*", Philips Journal of Research, Vol. 49, p.125-138 (1995).

[17] H. Baumgart, T. J. Letavic, and R. Egloff, "*Evaluation of wafer bonding and etch back for SOI technology*", Philips Journal of Research, Vol. 49, p.91-124 (1995).

[18] M. J. Missey, V. Dominic, L. E. Myers, and R. C. Eckardt, "*Diffusion-bonded stacks of periodically poled lithium niobate*", Optics Letters, Vol. 23, No. 9, p.664-666 (1998).

[19] K. Eda, M. Sugimoto, and Y. Tomita, "*Direct heterobonding of lithium niobate onto lithium tantalate*", Applied Physics Letters, Vol. 66, No. 7, p.827-829 (1995).

[20] Y. Tomita, M. Sugimoto, and K. Eda, "*Direct bonding of $LiNbO_3$ single crystals for optical waveguides*", Applied Physics Letters, Vol. 66, No. 12, p.1484-1485 (1995).

[21] K. Eda, M. Sugimoto, and Y. Tomita, "*Direct heterobonding of lithium niobate onto lithium tantalate*", Applied Physics Letters, Vol. 66, No. 7, p.827-829 (1995).

[22] C. T. A. Brown, C. L. Bonner, T. J. Warburton, D. P. Shepherd, A. C. Tropper, and D. C. Hanna, "*Thermally bonded planar waveguide lasers*", Applied Physics Letters, Vol. 71, No. 9, p.1139-1141 (1997).

[23] C. L. Bonner, T. Bhutta, D. P. Shepherd, and A. C. Tropper, "*Double-clad structures and proximity coupling for diode-bar-pumped planar waveguide lasers*", IEEE Journal of Quantum Electronics, Vol. 36, No. 2, p.236-242 (2000).

[24] C. B. E. Gawith, D. P. Shepherd, J. A. Abernethy, D. C. Hanna, G. W. Ross, and P. G. R. Smith, "*Second-harmonic generation in a direct-bonded periodically poled $LiNbO_3$ buried waveguide*", Optics Letters, Vol. 24, No. 7, p.481-483 (1999).

[25] C. B. E. Gawith, T. Bhutta, P.Hua, J. Wang, D. P. Shepherd, G. W. Ross, and P. G. R. Smith, "*Buried laser waveguides in neodymium doped BK-7 by $K^+$-$Na^+$ ion-exchange across a direct-bonded interface*", Applied Physics Letters, Vol. 75, No. 24, p.3757-3759 (1999).

[26] C. B. E. Gawith, P. Hua, P. G. R. Smith, and G. Cook, "*Nonreciprocal transmission in a direct-bonded photorefractive Fe:$LiNbO_3$ buried waveguide*", Applied Physics Letters, Vol. 78, No. 26, p.4106-4108 (2001).

[27] D. H. Lee, "*Electromagnetic principles of integrated optics*", John Wiley and Sons (1986).

[28] N. J. Cronin, "*Microwave and optical waveguides*", Institute of Physics Publishing (1995).

[29] A. Yariv, "*Quantum electronics*" 3rd Edition, John Wiley and Sons (1989).

[30] A. Ghatak, K. Thyagarajan, "*Introduction to fiber optics*", Cambridge University Press (1998).

[31] R. Guenther, "*Modern optics*", John Wiley and Sons (1990).

[32] C. L. Bonner, "*Multi-watt, diode-pumped planar waveguide lasers*" (Thesis), University of Southampton (2000).

[33] D. H. Jundt, "*Temperature-dependent Sellmeier equation for the index of refraction, $n_e$, in congruent lithium niobate*", Optics Letters, Vol. 22, No. 20, p.1553-1555 (1997).

[34] W. P. Risk, "*Modelling of longitudinally pumped solid-state lasers exhibiting reabsorption losses*", Journal of the Optical Society of America B, Vol. 5, No. 7, p.1412-1423 (1988).

# Chapter 3
# SECOND-HARMONIC GENERATION IN A DIRECT-BONDED PERIODICALLY-POLED LITHIUM NIOBATE BURIED WAVEGUIDE

## 3.1 Introduction

The primary application of nonlinear optical devices is the generation of new and tunable wavelength ranges not available with existing laser sources [1]. Dating back to the earliest experiment by Franken et al. in 1961 [2], the fundamental work on nonlinear optics arose as a direct result of the advent of laser technology and concentrated on the generation of second harmonics from a ruby laser as it propagated through a quartz crystal. Just a year later, Kleinmann [3] demonstrated that the efficiency of these early processes was limited by the effects of dispersion in the optical material, reducing the effective interaction between the fundamental and second harmonic waves as they travelled through the medium, and that this could be greatly improved by using crystal birefringence to match their relative phase velocity over an interaction distance of many optical wavelengths. The concept of quasi-phase-matching was also introduced in 1962, as Armstrong et al. [4] considered the prospect of allowing a steady slippage between the fundamental and second harmonic as they propagated through a nonlinear material, which they proposed could be periodically rectified by modification of the crystal structure. It would not be until the early 1980's however, that developments in the growth and manipulation of nonlinear crystals would mature sufficiently to allow the precise definition of such periodically domain-inverted structures [5], providing the basis for the diverse range of widely tunable wavelengths and devices under active research to the present day [6-8].

Described in this chapter are the fundamentals of second-harmonic generation in a nonlinear material and their application towards producing highly efficient buried waveguide devices in direct-bonded structures. The phase-matching techniques used to increase conversion efficiency in a frequency-doubling process are discussed, along with the methods used to create periodic domain inversion and optical confinement in $LiNbO_3$ substrates. The fabrication procedure used to bury a periodically-poled lithium niobate (PPLN) waveguide in lithium tantalate, from the choice of substrate materials to the direct bonding and precision polishing of each

material layer, is presented in full. Finally, the nonlinear characteristics of a buried PPLN waveguide device are described.

### 3.2 Second-harmonic generation

The origin of nonlinear effects, such as second harmonic generation, lies in the way in which atoms in a material become polarised under the application of an electric field [1]. In the case of a weak electric field, the polarisation is assumed to remain linearly proportional to the applied field and is defined by the equation [1]

$$P = \varepsilon_0 \chi_1 E \tag{3.1}$$

where $\varepsilon_0$ is the permittivity of free space, $\chi_1$ is the linear optical susceptibility of the material ($\chi_1 = n^2$ - 1), and $E$ is the electric field. However, as the applied electric field becomes more intense, the simple relation of Equation 3.1 becomes invalid and several contributions must be taken into account if the induced polarisation of the material is to be determined. Under a large electric field, the polarisation state of the material is expressed more generally as a power series expansion of the applied electric field by use of the equation [9]

$$P = \varepsilon_0\left(\chi_1 E + \chi_2 E^2 + \chi_3 E^3 + \ldots\right) \tag{3.2}$$

where $\chi_2$ and $\chi_3$ are the second and third-order nonlinear susceptibilities of the material. It is the term $\chi_2$ which then gives rise to second-harmonic generation in a material, as demonstrated when an electric field of the form $E = E_0 \sin \omega t$ (such as that produced by the temporal variation of an electromagnetic wave) is applied to Equation 3.2 to give [10]:

$$\begin{aligned} P &= \varepsilon_0\left(\chi_1 E_0 \sin \omega t + \chi_2 E_0^2 \sin^2 \omega t + \chi_3 E_0^3 \sin^3 \omega t + \ldots\right) \\ &= \varepsilon_0\left(\chi_1 E_0 \sin \omega t + \tfrac{1}{2}\chi_2 E_0^2\left[1 - \cos 2\omega t\right] + \ldots\right) \end{aligned} \tag{3.3}$$

where $E_0$ is the amplitude and $\omega$ the frequency of the incident electromagnetic wave. The resulting term in $2\omega$ corresponds to an electromagnetic wave with twice the frequency of the incident electromagnetic field, indicating that if the term $\varepsilon_0\chi_2 E^2$ is sufficiently large the fundamental wave will generate a second-harmonic as it propagates through the material [1]. From this basic premise, a variety of interesting optical phenomena arise from $\chi_2$ and $\chi_3$, many of which are used as the basis of frequency conversion. For example, $\chi_2$ gives rise to second-harmonic generation [2], dc rectification [11], the linear electro-optic effect [12], parametric oscillation [13],

and three-frequency mixing and sum generation processes [14]. The third-order nonlinear susceptibility results in third-harmonic generation [15], the quadratic electro-optic effect [16], two photon absorption [17], and Raman [18], Brillouin [19], and Rayleigh [20] scattering. As second-harmonic generation is the focus of this chapter, the effects that arise from $\chi_2$ will form the basis of further derivations, although a similar methodology can be applied to third-harmonic effects [21].

### 3.3 Material considerations

In a crystalline material both the linear susceptibility and the second-order nonlinear susceptibility are dependent upon the symmetry properties of the crystal [1]. In a centrosymmetric material the interaction of applied electric field and induced polarisation results in no asymmetric charge distribution, and therefore no net polarisation, such that the $\chi_2$ term (and subsequent even terms; $\chi_4$, $\chi_6$, etc.) of Equation 3.3 is cancelled. This effect is well illustrated by Yariv in Reference [21], and demonstrates that harmonic generation cannot be observed in solids that possess a center of symmetry (Figure 3.1a). In a noncentrosymmetric crystal however (such as $LiNbO_3$ [22]), an applied optical field produces an asymmetrical polarisation in the crystal, which can result in the generation of harmonic frequencies of the fundamental

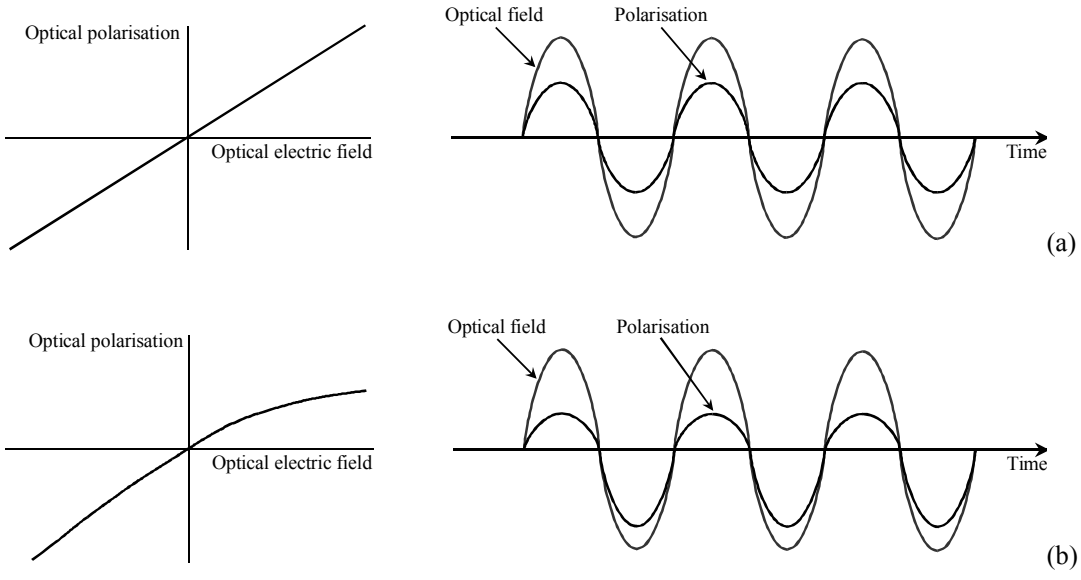


**Figure 3.1**: Relation between an applied sinusoidal electric field and induced polarisation in; (a) a linear dielectric crystal, and (b) a crystal lacking inversion symmetry, as illustrated in Reference [21].

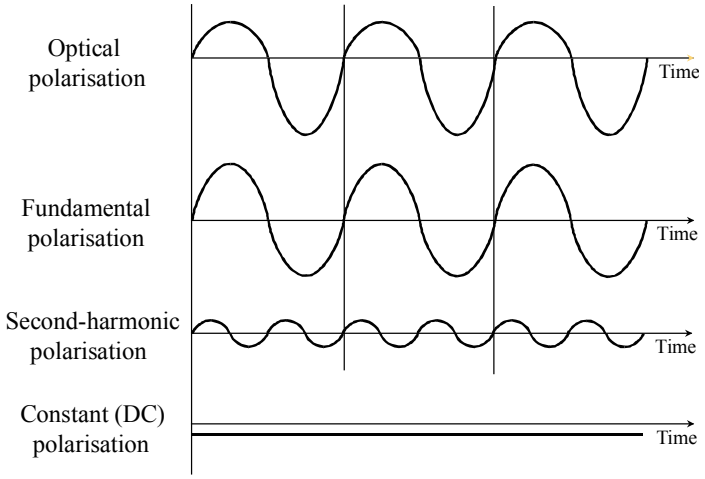


**Figure 3.2**: Fourier analysis of the nonlinear polarisation wave of Figure 3.1b shows that it contains components oscillating at; the fundamental frequency, twice the fundamental frequency (second-harmonic), and an average dc negative component, as illustrated in Reference [21].

wave as it propagates through the material (Figure 3.1b). A Fourier analysis of this polarisation shows that it consists of fundamental-frequency and frequency-doubled components, as well as a dc component, $\frac{1}{2}\varepsilon_0\chi_2 E_0^2$, as illustrated in Figure 3.2 [21].

The scale of nonlinearities in a crystal medium are dependent upon crystal structure and the polarisation of incoming light [5]. As such, the performance of second-harmonic generation for a particular material or crystal orientation is quantified by the introduction of nonlinear coefficients, full derivations of which are available in References [1,5,21]. By assuming that the depletion of the fundamental wave to the second-harmonic is negligible, that the absorption of the medium at the fundamental wavelength is also negligible, that there is no second-harmonic power at the start of a crystal, and that the fundamental travels as a plane wave, the overall efficiency of second-harmonic generation is often described in relation to the effective nonlinear coefficient of the material, $d_{eff}$, via the equation [5]

$$\eta = \frac{I_{2\omega}}{I_\omega} = \frac{2\omega^2 d_{eff}^2 l^2 I_\omega}{n_\omega^2 n_{2\omega} c^3 \varepsilon_0} \operatorname{sinc}^2\left(\frac{\Delta k l}{2}\right) \tag{3.4}$$

where $I_\omega$ and $I_{2\omega}$ are the fundamental and second-harmonic intensities respectively, $l$ is the material length, $n_\omega$ is the refractive index of the material at the fundamental wavelength ($\lambda_\omega$), $n_{2\omega}$ is the refractive index at the wavelength of the second-harmonic, and $\Delta k = k_{2\omega} - 2k_\omega$ is the difference between the corresponding wave vectors ($k_\omega = 2\pi n_\omega / \lambda_\omega$, etc.) due to wavelength dispersion in the material. From this equation

it is clear that for a plane wave interacting in a nonlinear material the conversion efficiency from fundamental to second-harmonic is quadratically dependent on both the nonlinear coefficient and the length of the sample, and is proportional to the fundamental intensity. However, in practice Gaussian intensity laser beams are used instead of plane waves, and are often tightly focussed into the centre of a nonlinear crystal to increase the fundamental intensity required for efficient second harmonic generation [1]. Subsequent beam divergence, from the beam waist and towards the ends of the nonlinear material, defines a physical limit for optimal focussing and frequency doubling efficiency of this interaction based on the overall length of the sample, an effect explored mathematically by Boyd and Kleinmann in the relation [23]

$$\eta = \frac{2\omega^2 d_{eff}^2}{\pi n_\omega^2 n_{2\omega} \varepsilon_0 c^3} P_\omega l k_\omega h(\beta, \xi) \tag{3.5}$$

where $P_\omega$ is the power of the fundamental beam, and the term $h(\beta,\xi)$ is the Boyd-Kleinmann focussing factor ($\xi = l / k_\omega w_0^2$ is the focussing parameter and $\beta = \frac{1}{2}\rho(lk_\omega)$ is the double refraction parameter used to describe Poynting vector walk-off ($\rho$ is the refraction angle) between the fundamental and second-harmonic beams [23]). As such, the focussed interaction of high-intensity fundamental and second-harmonic beams in a bulk nonlinear material demonstrates a conversion efficiency proportional to the length of the crystal (rather than the length squared). However, in an optical waveguide geometry the effects of beam divergence in the nonlinear material can be avoided, and the high incident intensity offered by a focussed Gaussian beam can be governed solely by the area of the guided mode [1]. As a result, the conversion efficiency between fundamental and second-harmonic beams in a nonlinear-material based waveguide device would feature the combined benefits of a quadratic dependence on length and nonlinear coefficient, and a proportional dependence on intensity (in a waveguide geometry the effective refractive indices of each mode and overlap integral of modal intensity distributions must be taken into account (see Section 2.8)), as described in Equation 3.4. In a crystal such as $LiNbO_3$ for example, which features three nonlinear coefficients [24]; $d_{22}$ (~ 2.5 pm $V^{-1}$), $d_{31}$ (~ 5 pm $V^{-1}$), and $d_{33}$ (~ 30 pm $V^{-1}$), it would therefore be beneficial to access the largest of these coefficients over the longest distance possible, with the high fundamental beam intensity offered by focussing into an optical waveguide.

### 3.4 Phase-matching techniques

Reduced efficiency in second-harmonic generation is caused by wavelength dispersion within the nonlinear material, an effect that causes frequency doubled light to propagate at a speed different to that of the fundamental pump beam [5]. The result is that the fundamental and second-harmonic waves will periodically become out of phase as they propagate through the crystal, causing destructive interference of the second-harmonic. The intensity of the frequency-doubled light therefore varies periodically throughout the crystal, with a maximum value being reached after the two waves have propagated by just a few microns (depending on the wavelengths involved). This distance is called the coherence length of the material and is defined as [5]

$$l_c = \frac{\pi}{\Delta k} = \frac{\lambda_\omega}{4\left(n_{2\omega} - n_\omega\right)}. \tag{3.6}$$

Once this coherence length has been passed, the energy in the second-harmonic is returned to the fundamental wave, resulting in zero irradiance of the frequency doubled light after two, or any even number of coherence lengths [4]. This in turn results in a low average conversion efficiency between the fundamental and second-harmonic frequencies, as demonstrated by the graph of Figure 3.3.

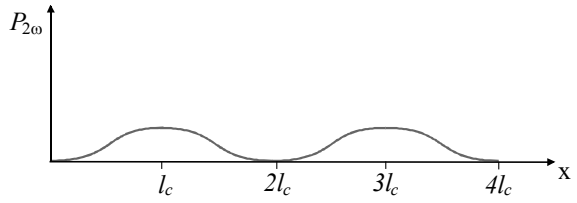


**Figure 3.3**: A graph of second-harmonic output power ($P_{2\omega}$) vs. distance of propagation ($x$) through a nonlinear material [25].

In order to maximise the conversion efficiency between fundamental and second-harmonic frequencies in $LiNbO_3$, the effective coherence length for continuous generation of second-harmonic power must be extended. Phase-matching [1,3] is a well established technique for accomplishing this, and is performed by forcing the fundamental and second-harmonic waves to remain in phase as they propagate through the crystal medium. In a system based on second-harmonic generation, the refractive indices of the crystal at the fundamental and second-harmonic wavelengths must be balanced such that $n_{2\omega} = n_\omega$ if phase-matching is to be achieved. This can be effectively demonstrated in many negative birefringent crystals, which can be aligned

to allow the fundamental (pump) frequency to correspond to the ordinary ray of propagation, and the second-harmonic (signal) to the extraordinary ray [10] (Figure 3.4), conditions which should be reversed for positive birefringent materials. With this technique, the coherence length can be increased from microns to the entire crystal length, allowing a continuous build up in the irradiance of the frequency doubled light and a subsequent increase in conversion efficiency by orders of magnitude [10].

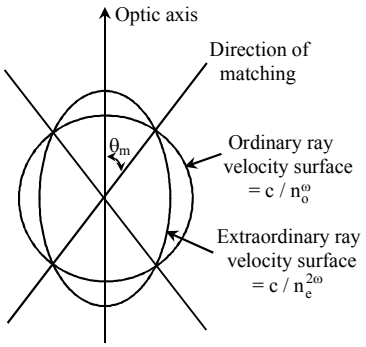


**Figure 3.4**: Index matching in a negative birefringent material. The condition $n_e^{2\omega} = n_o^{\omega}$ is satisfied for propagation at an angle $\theta_m$ to the optic axis [10].

Unfortunately, maximising the efficiency of second-harmonic generation via the birefringent-phase-matching technique can be a difficult process, as several optimising factors must to be taken into account. The most critical of these requirements is the ability to match the refractive indices of the fundamental and second-harmonic waves as they propagate through the material, a balance which can be thwarted by wavelength-related dispersion in the crystal media. This effect limits the range of wavelengths available for frequency-doubling by birefringent-phase-matching, although some limited flexibility is available by tuning the individually temperature dependent refractive indices of the birefringent material [5]. However, it should be noted that materials exhibiting an insufficient level of birefringence, such as $LiTaO_3$, cannot be phase-matched via birefringence at any temperature. Further disadvantages of this technique include the fact that birefringent-phase-matching is unable to access the largest nonlinear coefficient of $LiNbO_3$, $d_{33}$ [24]. The available alternative, $d_{31}$, offers a reduced nonlinear conversion efficiency that limits the overall performance of this technique.

As an alternative to birefringent-phase-matching, quasi-phase-matching [4,5,8] is a process designed to ease the stringent conditions for overcoming dispersion in second-harmonic generation. By adapting the domain structure of a ferroelectric material, it is possible to periodically alter the spontaneous polarisation within the material and take full advantage of the high irradiances of frequency-doubled light that are available after each coherence length of propagation [5]. Since the sign of the nonlinear coefficient is related to the direction of spontaneous polarisation, periodic reversal of the domain orientation can be used to provide a consistent phase slippage between the fundamental and second-harmonic fields as they travel through the material, dramatically increasing the efficiency of second-harmonic generation. In general, the period used for quasi-phase-matched second-harmonic generation in a $LiNbO_3$ crystal is given by the equation [5]:

$$\Lambda = 2l_c = \frac{\lambda_\omega}{2\left(n_{2\omega} - n_\omega\right)} \tag{3.7}$$

where $\Lambda$ is the grating period and corresponds to a change in domain orientation after every coherence length of propagation. Such a structural change is referred to as periodic poling [5], and can be used to increase the distance of interaction between the fundamental and second-harmonic frequencies from one coherence length to the full extent of the crystal. This is a crucial step in optimising the effects of frequency-doubling, as the conversion efficiency of second-harmonic generation is proportional to length squared. To illustrate this effect, the graph of second-harmonic output power versus propagation distance for poled and unpoled $LiNbO_3$ samples, given in Figure 3.5, shows the increased output efficiency available from a quasi-phase-matched system over just a few periods of domain inversion [5].

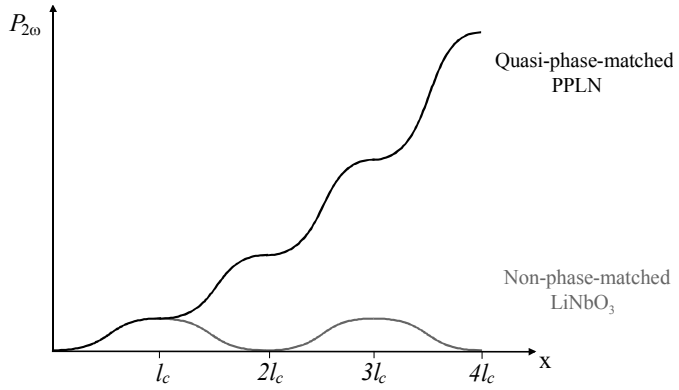


**Figure 3.5**: A graph of second-harmonic output power ($P_{2\omega}$) vs. distance of propagation ($x$) through a quasi-phase-matched PPLN substrate, and an unpoled $LiNbO_3$ substrate [25].

In addition to escaping the necessity of index-matching for an increase in conversion efficiency, quasi-phase-matching has the added bonus of being able to access the largest nonlinear coefficient in $LiNbO_3$, $d_{33}$. This is performed by periodically inverting the material along its optic axis and propagating both the fundamental and second-harmonic waves with polarisations parallel to the domain inversions [26] (both waves are polarised in the z-direction), an arrangement illustrated in Figure 3.6. Further benefits of quasi-phase-matching include its relatively simple technique, operational stability, and a widely selectable phase-matching wavelength, which offers a range of frequency doubled outputs for the full transparency range of $LiNbO_3$ (approximately 350 nm to 4800 nm [5]). This provides a distinct advantage over birefringent-phase-matching, which cannot compensate for wavelength dispersion below a fundamental wavelength of 1000 nm in $LiNbO_3$ [8] (making the second-harmonic generation of blue light via this technique impossible), by allowing much shorter wavelengths to be generated.

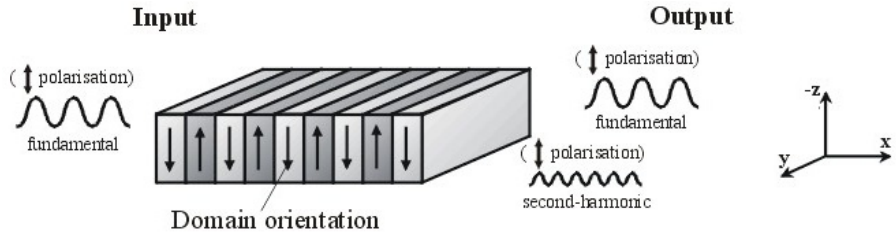


**Figure 3.6**: Orientation of crystal structure and polarised fundamental and second-harmonic waves for quasi-phase-matching in a PPLN substrate.

## 3.5 Periodically-poled lithium niobate

The ability to create periodic domain (and nonlinear coefficient) reversal in lithium niobate for quasi-phase-matching processes is an essential step in improving the efficiency of second-harmonic generation in the material. The longstanding popularity of $LiNbO_3$ as a basis for nonlinear processes comes from the material's large nonlinear coefficient, low melting temperature [22] (a factor which makes the material easier to produce and thus widely available), ready availability (arising from the use of $LiNbO_3$ surface acoustic wave filters in every mobile phone), and ferroelectric crystal structure that lends versatility in the methods used for domain inversion [5,6,22].

The crystal structure of $LiNbO_3$ is composed of distorted oxygen octahedra that are rotated in a screw-like fashion through successive layers of the material [22]. Oxygen ions are arranged in a hexagonally close packed structure in planes perpendicular to the optic axis (z-axis), with each plane being separated by a lithium or niobium ion at sequential interstitial sites. It is the relative position of these metallic ions along the optic axis of the crystal that determines the phase of the material [5], be it paraelectric or ferroelectric (Figures 3.7 (a) and (b) respectively). In the paraelectric phase, above the ~ 1120 °C Curie temperature of $LiNbO_3$ [22], the $Li^+$ ions are situated at the center of a plane of oxygen ions and the $Nb^{5+}$ ions are at the center of oxygen octahedra, leading to a symmetrical configuration with no spontaneous polarisation. Conversely, the ferroelectric phase of $LiNbO_3$, below the Curie temperature, features an asymmetric configuration wherein $Li^+$ and $Nb^{5+}$ ions are no longer situated at equal distances between the planes of oxygen atoms. In this case the two metallic ions are displaced by different amounts along the optic axis of the crystal (the lithium and niobium ions are pulled apart slightly) in a direction that defines the sign of the spontaneous polarisation of the crystal [22]. By referring back to the illustration of

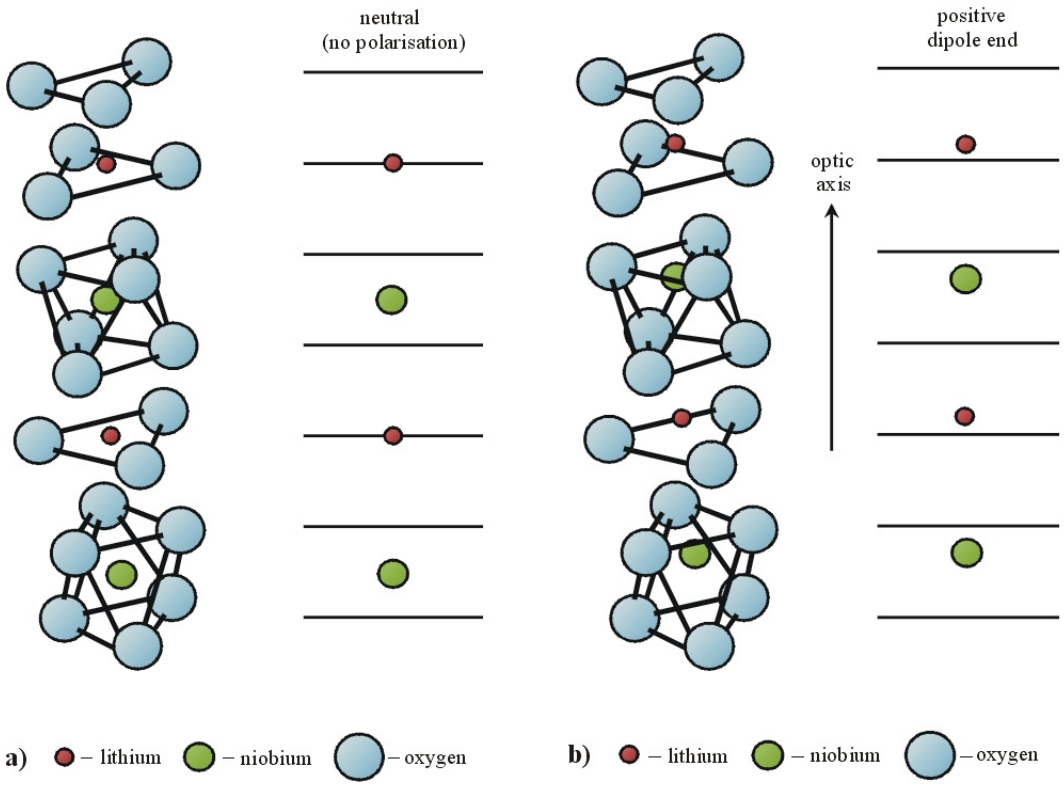


**Figure 3.7**: The (a) paraelectric (nonpolar) and (b) ferroelectric (spontaneous polarisation) phases, of $LiNbO_3$ [5].

Figure 3.7b, it becomes evident that inducing the $Li^+$ ions to move across the triangular plane of oxygen atoms will reverse the sign of spontaneous polarisation in the crystal, producing the desired effect of inverting the material's nonlinear coefficient [5].

Periodic poling in lithium niobate has been performed using a number of techniques involving the application of heat, chemistry, electric fields, or combinations of the three [5,8]. In each case the desired outcome is to alter the single-domain structure of the material to a structure with periodic 180° reversals of the $d_{33}$ nonlinear coefficient along the x-axis of the crystal (Figure 3.6). The devices described in this chapter incorporate several periodically poled gratings, which were created by an electric field poling technique at room temperature.

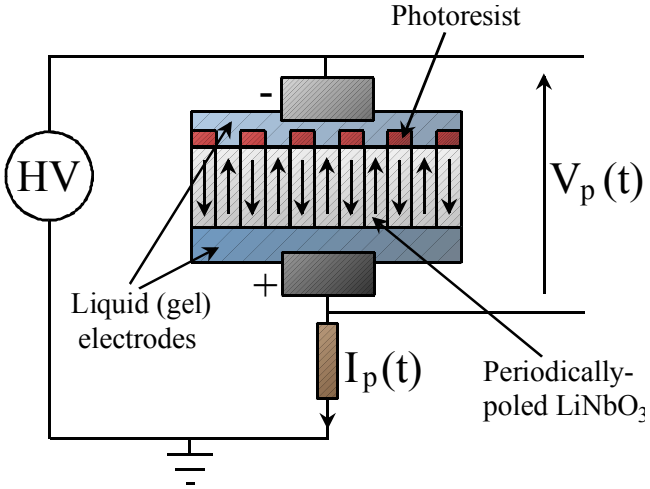


**Figure 3.8**: Experimental arrangement for room temperature electric field poling of $LiNbO_3$ [16].

As stated earlier, the ferroelectric phase of lithium niobate is defined by its spontaneous polarisation ($P_s$) of ~ 0.7 $Cm^{-2}$ [26]. In a single domain crystal of lithium niobate, where the spontaneous polarisation is uniform throughout, the surface charge of the material is determined by the relation $Q = P_sA$, where $A$ is the cross-sectional area of the crystal. In order to invert the spontaneous polarisation of $LiNbO_3$ at room temperature, an electric field exceeding the coercive field ($E_c$ = 21 $kVmm^{-1}$) of the crystal must be applied [5], the effect of which is to force the $Li^+$ ions to cross the oxygen planes in the crystal lattice. For room temperature electric field poling, a high voltage is applied to single domain $LiNbO_3$ via regularly placed electrodes on the -z face of the crystal, as shown in Figure 3.8. A standard photolithographic process is

used to define a pattern of photoresist on the -z face of the crystal, incorporating open regions through which the domain inverting voltage is applied, and masked regions for which 1-2 μm-thick photoresist is sufficient to block the applied field. Contact is made between the surface of the crystal and the high voltage supply electrodes by use of a conductive gel, which can be applied between the fine periods of photoresist mask without the risk of spillage. A grounded negative electrode is contacted to the -z face of the crystal, while a positive electrode allows the application of high voltage pulses to the non-patterned +z face of the sample. During the application of a high voltage pulse ($V_p$) of ~ 22 kVmm$^{-1}$ negative current derived feedback ($I_p$) is used to control the voltage across the sample, allowing precise control of the poling temporal profile.

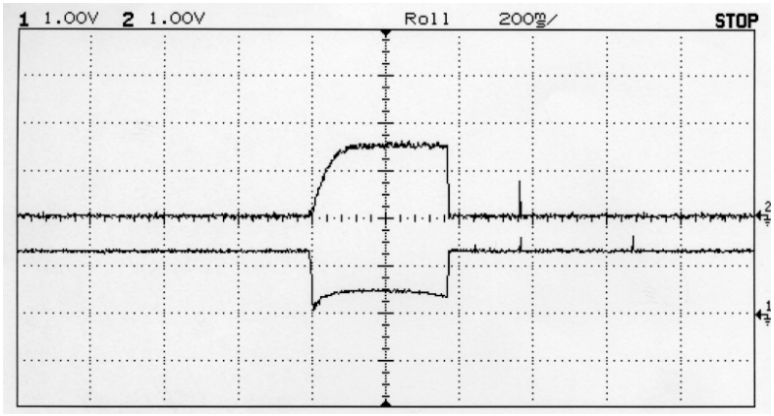


**Figure 3.9**: Oscilloscope trace featuring current and voltage characteristics of the room temperature electric field poling process of PPLN. Trace provided by Graeme Ross of Southampton University.

As domain inversion involves the reversal of the spontaneous polarisation of the material, the total charge flowing from one electrode to the other during poling must be equal to $Q = 2P_sA_{inv}$, where $A_{inv}$ is the cross-sectional area of the crystal to undergo domain inversion. Current measurements give control over this process, as the area under the curve of poling current versus time represents the total charge moved from one electrode to the other during the process. Monitoring voltage changes between the two surface electrodes also provides useful information, as a sharp increase in voltage indicates sample breakdown, wherein the crystal is forced to conduct and electron avalanche occurs [24]. Typical traces of poling current and voltage versus time, as recorded during the application of a high voltage to a $LiNbO_3$ crystal, are given in Figure 3.9. The characteristic current curve illustrates the rise and fall in current associated with domain switching in the material, and the voltage trace (displayed

upside-down to allow distinction between the two graphs) remains approximately constant, indicating no breakdown in the device. An example of a uniform PPLN grating, fabricated by the application of an electric field at room temperature, is given in Figure 3.10. The versatility of this electric-field poling technique can be applied to offer a widely selectable phase-matching wavelength in lithium niobate, with the period of each domain inverted structure being predetermined to match the coherence length of a given input beam by use of Equation 3.7. Examples of this include; ~ 6.50 μm periods of domain inversion in $LiNbO_3$ being used to frequency double a 1064 nm (infra-red) fundamental beam to give a 532 nm (green) second-harmonic output [27-28], and a 4.50 μm period of domain inversion in $LiNbO_3$ being used to frequency double a 946 nm (infra-red) fundamental beam to give a 473 nm (blue) second-harmonic output [29-30].

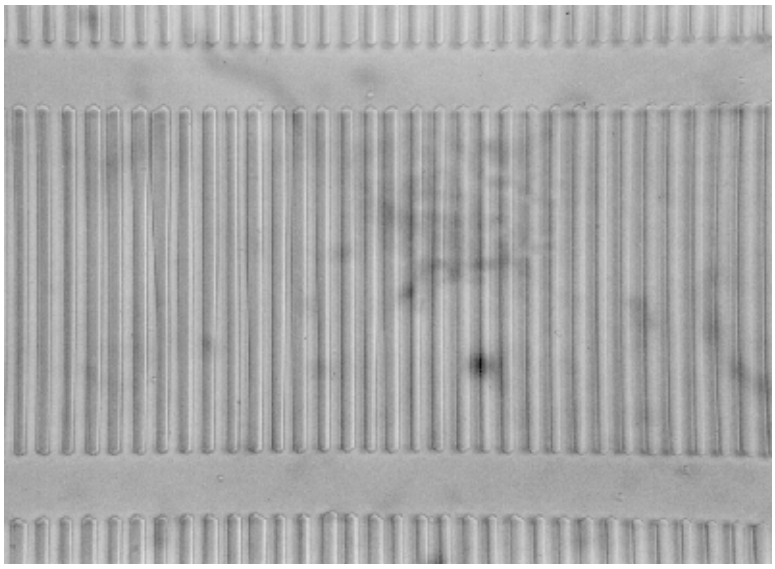

**Figure 3.10**: A photograph of the z-face of a 30 μm PPLN grating fabricated by the application of an electric field at room temperature. The dark stripes indicate regions of domain inversion in the $LiNbO_3$ substrate. Picture provided by Joyce Abernethy of Southampton University.

### 3.6 PPLN waveguides

Periodically-poled lithium niobate combines the important characteristics of a large nonlinear coefficient and non-critical phase-matching capabilities for any wavelength in its transmission range, making it an attractive material for nonlinear frequency conversion. The combination of these material characteristics with the optical confinement offered by a waveguide geometry provides a promising route to the realisation of various compact nonlinear devices based on harmonic or parametric generation.

One of the most commonly used methods for fabricating waveguides in $LiNbO_3$, which is also suitable for PPLN, is titanium indiffusion [31-33]. This process diffuses titanium into the $LiNbO_3$ from a deposited metal layer, replacing vacant Li and Nb sites in the crystal matrix to create a graded-index waveguide. The resulting change in crystal structure can have an adverse affect on both the nonlinearity and domain-inverted structure of a PPLN substrate [31], although waveguides produced by this method have demonstrated effective second-harmonic generation of an 845 nm fundamental frequency into the blue with a conversion efficiency of 1.6 % $W^{-1}$ $cm^{-2}$ [31]. Proton exchange techniques are another popular method for creating waveguides in both lithium niobate and PPLN [34-36], relying on an acidic melt to remove lithium ions from the bulk crystal structure and form hydroxyl groups in their stead. Unfortunately, the refractive index change in proton-exchanged waveguides is not isotropic, such that only the extraordinary refractive index is raised and the ordinary index is slightly lowered [32]. As a result, such waveguides will only display optical confinement for either TE or TM modes of propagation, depending on the cut of the crystal. Traditional proton exchange techniques can also result in the complete erasure of PPLN's domain-inverted structure while causing a reduction of nonlinearity in the material by up to 80 %, although more recent methods have solved these problems [34].

In contrast to these methods, direct bonding [37-38] can be used to combine bulk layers of PPLN and suitable cladding materials to form waveguiding boundaries. Such a bond can be formed irrespective of the lattice constants and orientation of the materials involved and causes no deleterious modification of the crystalline microstructure of either material [38]. By bringing surfaces into contact this way, direct bonding can be used to create a multi-layered PPLN waveguide device that preserves the bulk characteristics of each bonded material. Some recent experiments investigating the bonding characteristics of PPLN have been directed toward fabricating thick multi-layered stacks of the material to form a large physical aperture for use in high power applications [39]. By contrast, the experiments described in this chapter have been aimed at creating a thin waveguiding layer of PPLN and exploiting optical confinement to obtain efficient second-harmonic generation, even at low pump powers. The presented results are from a planar waveguide device fabricated by direct

bonding PPLN onto a suitable substrate before precision polishing it down to waveguide dimensions, a method similar to that demonstrated in the production of (unpoled) $LiNbO_3$ planar waveguides for electro-optic applications [38,40]. One of the primary attractions of this technique is that during the fabrication process the nonlinearity and domain characteristics of the PPLN structure should remain entirely unchanged from those of the bulk material, unlike most proton exchange and titanium indiffusion techniques. A further attraction of the direct bonding method is the extra flexibility available when designing devices, offering the possibility to combine multiple layers with different material properties. Such structures have previously been explored in the fabrication of silicon semiconductors (see Reference [41] and other papers on direct bonding in the same journal issue) and garnet and glass waveguides for use in lasers [42], although many areas of exploration remain for the direct bonding of multi-layered optical devices. To this end, the remainder of this chapter describes the fabrication of a symmetrical PPLN waveguide buried in $LiTaO_3$ by direct bonding and precision-polishing methods, and the characteristics of second-harmonic generation exhibited by the domain-inverted structure.

### 3.7 Fabrication of buried PPLN waveguide devices

Fabrication of the buried PPLN waveguide device began with a 0.5-mm-thick single-domain z-cut $LiNbO_3$ sample of ~ 15 mm × 15 mm surface area. A photoresist pattern was created on the -z face of the crystal by photolithography, and domain inversion in the z-axis was performed at room temperature by application of a single high-voltage pulse of approximately 11 kV through liquid electrodes. Application of this pulse resulted in three 5.5-mm-long PPLN gratings positioned in the centre of the $LiNbO_3$ sample at 1 mm intervals. Grating periods of 6.58 μm, 6.50 μm, and 6.38 μm were created, the first two of which are suitable for frequency doubling of a Nd:YAG laser operating at 1064 nm. $LiTaO_3$ was chosen as a suitable material for both the substrate and the cladding layers, as it has a lower refractive index than $LiNbO_3$ and also combines thermal characteristics that are a good match for $LiNbO_3$, an essential prerequisite when annealing bonds at high temperatures. To illustrate crystal compatibility, the extraordinary refractive indices ($n_e$) of $LiNbO_3$ and $LiTaO_3$ are presented in Figure 3.11, as calculated for the wavelength range of 400 nm to 4000 nm by the use of temperature dependent Sellmeier equations (the crystals are

assumed to be at a room temperature of approximately 25 °C) [43,44]. In addition, the thermal expansion coefficients [45] of each crystal are given in Table 3.1.

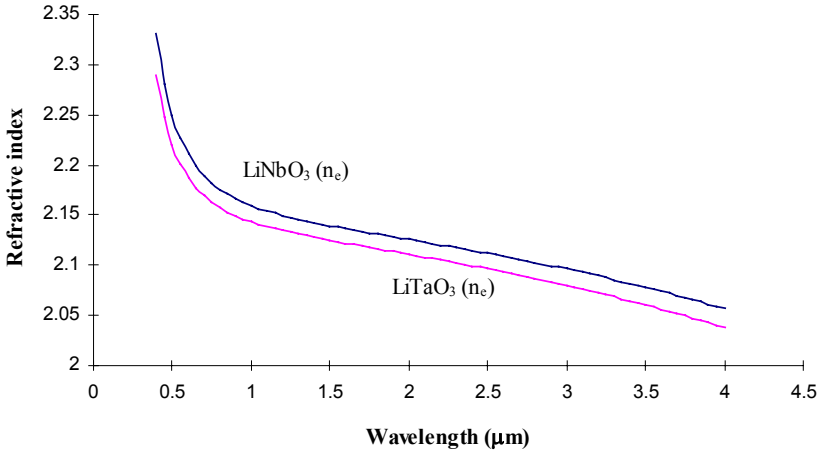


**Figure 3.11**: Extraordinary refractive indices, $n_e$, of $LiNbO_3$ and $LiTaO_3$ throughout the wavelength range of 400 nm to 4000 nm. Refractive index profiles are calculated by use of Sellmeier equations [43,44], assuming a room temperature of 25 °C.

| Crystal | Coefficient of linear thermal expansion (0 – 500 °C) | | |
|---|---|---|---|
| | $\alpha\times10^{-6}$ °C (x-direction) | $\alpha\times10^{-6}$ °C (y-direction) | $\alpha\times10^{-6}$ °C (z-direction) |
| $LiNbO_3$ | 14.4 | 16.1 | 7.5 |
| $LiTaO_3$ | 15.9 | 15.4 | 2.2 |

**Table 3.1**: Thermal expansion coefficients of $LiNbO_3$ and $LiTaO_3$ [45].

The $LiTaO_3$ substrate used in this experiment was 0.5-mm-thick and was shaped relative to the PPLN sample, providing a bonding area of ~ 12 mm × 10 mm between the two optically flat surfaces. A mixture of $H_2O_2$-$NH_4OH$-$H_2O$ (1:1:6) was applied to both materials after they were cleaned, followed by several minutes of rinsing in deionised water so that their surfaces could be rendered hydrophilic [46]. The PPLN and $LiTaO_3$ layers were brought into contact at room temperature, with both samples aligned along the same crystalline orientation. A heat treatment of 120 °C immediately followed crystal contact, inducing the pyroelectric effect [22] at the direct bonding interface. The resultant electrostatic attraction forced any excess air or liquid from between the two surfaces, while bringing them close enough to encourage the formation of hydrogen bonds. This effect was demonstrated by the elimination of most of the contact fringes at the crystal interface. Annealing of the bonded sample at 350 °C for 6 hours provided a bond strength sufficient for further machining, and the PPLN region was then polished down to obtain a waveguiding layer of

12-μm-thickness (with a variance of less than 1 μm across the entire layer, as observed by optical inspection). A further direct-bonded cladding layer of $LiTaO_3$ was then added with the same procedure as above.

**Figure 3.12:** A photograph of three direct-bonded $LiNbO_3$ planar waveguide devices. The sample to the left is the PPLN device described in this chapter.

The final direct-bonded structure included interfaces of approximately 12 mm × 10 mm above and below the PPLN core, although the presence of optical fringes provided evidence of small unbonded regions at the edges of the sample. The unwanted material surrounding the gratings was later removed by use of a dicing saw, and the waveguide end faces were then polished to a parallel optical finish (Figure 3.12). The dimensions of the resulting buried PPLN planar waveguide structure are given schematically in Figure 3.13. Figure 3.14 is a photograph of the polished end-face of the device, taken at 50× magnification, which demonstrates the uniformity of the bonded interfaces above and below the buried waveguide. Further investigation showed no signs of any gaps along either polished end-face, up to the 100× magnification limit of the microscope used.

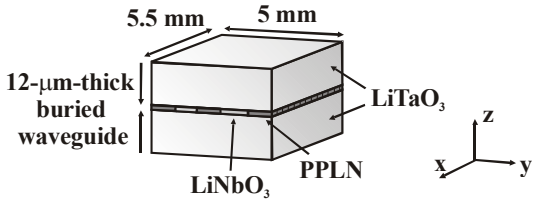


**Figure 3.13**: Schematic end-face diagram of buried $LiNbO_3$ waveguide, incorporating three PPLN gratings (fabricated before bonding), each 1-mm-wide.

**Figure 3.14**: A photograph of the polished end-face of a 12μm thick PPLN waveguide (running horizontally through the middle of the picture) buried in $LiTaO_3$ by direct bonding and precision polishing techniques. Taken at 50× magnification, this picture demonstrates the uniformity of each direct-bonded interface.

## 3.8 Waveguide characteristics

To test the nonlinear properties of the buried PPLN structure the characteristics of second-harmonic generation for the 6.50-μm-period grating were investigated. This grating, which occupied the middle section of the buried waveguide, performed more efficiently than the other available gratings during initial tests and thus was chosen for full investigation. The 1064-nm pump source used in these experiments was a cw diode-pumped Nd:YAG laser operating with multi-axial modes. The linear polarisation state was rotated with a half-wave plate so that it was parallel with the z-axis of the PPLN to access the $d_{33}$ nonlinear coefficient. Focussing of the pump radiation for launch into the waveguide was performed with the combination of microscope objective and cylindrical lenses shown in Figure 3.15. The initially circular pump beam was passed through a 2.4× cylindrical-lens telescope to expand it

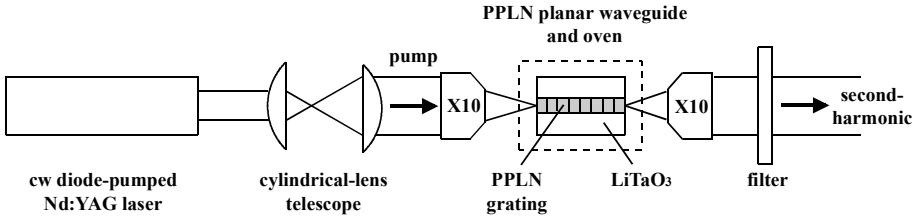


**Figure 3.15**: Experimental arrangement for second-harmonic generation in a buried PPLN waveguide (side view). A fundamental beam of 1064-nm wavelength was used for frequency-doubling experiments in the 6.5-μm PPLN grating.

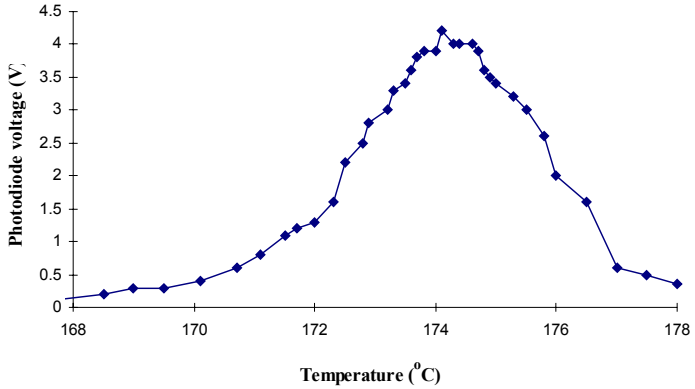


**Figure 3.16**: A graph of relative second-harmonic output power (measured by use of a photodetector) vs. temperature for a 6.50μm period buried PPLN grating with a 1064 nm cw diode-pumped Nd:YAG laser fundamental source.

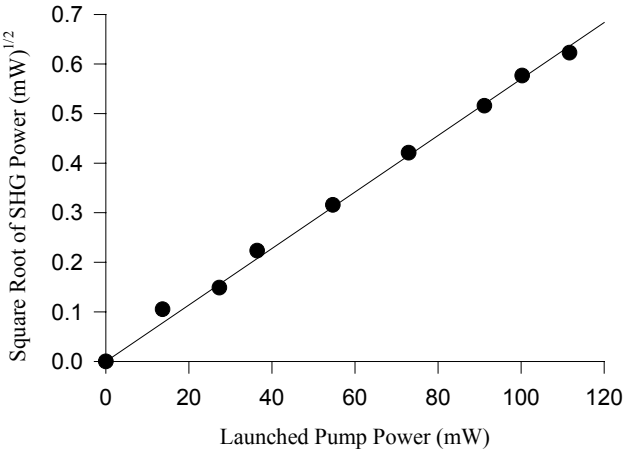


**Figure 3.17**: Dependence of the square root of the generated second-harmonic (532-nm) power on fundamental infrared (1064-nm) power. The powers are internal to the PPLN.

in the guided direction before focussing the beam onto the PPLN grating with a 10× microscope objective. Such a combination of optics was chosen to provide a good launch efficiency while helping to reduce divergence in the horizontal unguided plane. This choice resulted in a pump source with a line focus spot size of 4 ± 1 μm in the guided direction and 11 ± 1 μm in the nonguided direction, as measured with a silicon camera and mode profiling software. It should be noted that focussing to a waist in the nonguided plane at the input face is not the optimum condition for maximum conversion efficiency to the second-harmonic [23], and was chosen here for the sake of simplicity. Also, for this initial demonstration both the input and the output end faces of the waveguide were polished but left uncoated, leading to a 14% Fresnel reflection at each face. A second 10× microscope objective was used to collect the transmitted light from the waveguide, followed by an infrared filter to remove any pump light from the measurements of second-harmonic output power. Temperature tuning of the grating to 174.1 °C minimised the photorefractive effect during operation of the device [24], and a graph of second-harmonic output power versus temperature was measured with a photodetector (Figure 3.16). Subsequent measurements of optimised second-harmonic output power were recorded with a power meter.

For 204 mW of launched pump power (λ = 1064 nm), a second-harmonic power of 1.8 mW (λ = 532 nm) was generated internal to the crystal, corresponding to a conversion efficiency of 4.3 % $W^{-1}$ for the buried planar waveguide device (a figure of merit obtained by assuming 1 Watt of fundamental input power [8]). Figure 3.17 shows a plot of the square root of the second-harmonic power versus launched pump power, confirming the expected quadratic dependence (Equation 3.4). In the absence of a detailed analysis for second-harmonic generation in this mixed guided-unguided geometry, the observed efficiency of the buried PPLN waveguide device was compared with a calculation of optimised second-harmonic power expected from a similar length of bulk PPLN material. Following the Boyd-Kleinmann treatment for a focussed interaction, the second-harmonic output power for a bulk PPLN device is determined by the equation [23]:

$$P_{2\omega} = \frac{2\omega^2 P_\omega^2 d_{eff}^2}{\pi n_{2\omega} n_\omega^2 \varepsilon_0 c^3} k_\omega L h(B,\xi) \tag{3.8}$$

where $d_{eff} = (2/\pi)d_{33}$ is the effective nonlinear coefficient of the PPLN grating [16], and $h(B,\xi)$ is the Boyd-Kleinmann factor, which is assumed to equal 1 for a noncritical phase-matching geometry with no walk-off and optimised focussing in the center of the grating [23]. Further assuming an effective nonlinear coefficient of 16 pm $V^{-1}$ (a value lower than the predicted maximum of 21 $pmV^{-1}$, but consistent with results in similarly produced PPLN gratings [27]), an optimized second-harmonic output power of 1.3 mW is predicted for the bulk material, a lower result than the 1.8 mW of power obtained from the direct-bonded waveguide. This comparison demonstrates that even with nonoptimum focusing, a short crystal length, and only one guided dimension, the buried PPLN device shows an improved second-harmonic conversion efficiency of almost 40% over that of the bulk material.

An upper limit for the propagation loss of the waveguide structure was found by measuring the transmission of a 1064-nm laser beam when it was end launched into the waveguide. It was noted that the transmission changed between the PPLN and the $LiNbO_3$ (not periodically poled) sections of the waveguide, and the launch condition was therefore optimised individually for each of these regions. A maximum transmission of 81% was found at the edges of the PPLN grating (where the most efficient second-harmonic generation occurred) and throughout the uniform $LiNbO_3$ sections, whereas 65% transmission was obtained at the center of the PPLN grating. As the end-faces of the device were not anti-reflection coated, these results account for a Fresnel reflection of 14% at each end-face of the device and can be converted into a propagation loss in dB $cm^{-1}$ using the relation [10]

$$loss(\mathrm{dB\,cm^{-1}}) = \frac{10\log_{10}T}{L_{cm}} \tag{3.9}$$

where $T$ is the measured transmission and $L$ the length of the device in centimeters. Thus, over the 5.5-mm length of the grating, the upper limit on the propagation loss in each section is found to be 1.7 dB $cm^{-1}$ for the PPLN edges and the $LiNbO_3$ regions and 3.4 dB $cm^{-1}$ for the center of the PPLN grating. As the quoted transmission figures also include launch losses, it can be assumed that the propagation losses are much lower.

Modal characterisation of the output from the PPLN waveguide was performed with a video camera and PC-based evaluation software. It was observed that both the remaining 1064-nm light and the second-harmonic radiation generated by the PPLN grating were in the fundamental spatial mode (Figure 3.18a), despite the fact that a 12-μm-thick waveguide with such a large index difference ($\Delta n_e \approx 1\%$) could be expected to support a number of modes. Only by using a deliberately poor launch was it possible to excite anything other than the fundamental mode at 1064 nm. At the same time, it was noted that the 1064-nm throughput from the $LiNbO_3$ region within the same buried structure was multispatial mode in nature (Figure 3.18b). This clear difference in the mode properties, combined with the different transmissions described above, suggests that the index profile of the PPLN grating is different from that of the uniform $LiNbO_3$ region. The reason for these unexpected but potentially useful properties has not yet been determined, although they are possibly linked to strain-induced changes in refractive index throughout the buried layer. It is hoped that this effect can be developed and exploited to provide a simple route towards creating channel waveguides in a direct-bonded structure, as discussed in Section 7.2.

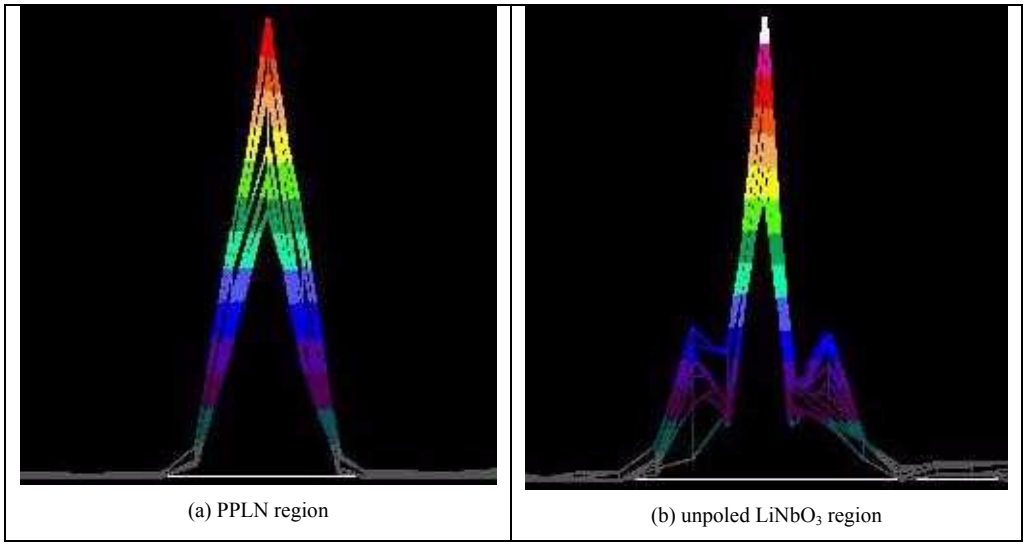

(a) PPLN region

(b) unpoled $LiNbO_3$ region

**Figure 3.18**: Modal properties of the (a) PPLN, and (b) unpoled $LiNbO_3$ sections of the buried waveguide. Both images are measured as output intensity (vertical, arbitrary units) vs. waveguide cross-section (horizontal, arbitrary units). The single peak of graph (a) depicts single-mode behaviour, and (b) depicts multi-mode behaviour in the same buried structure.

## 3.9 Conclusions

This chapter describes the successful fabrication of a 12-μm-thick 5.5-mm-long symmetrical direct-bonded PPLN waveguide buried in $LiTaO_3$. Using a 6.50 μm

period PPLN grating at an elevated temperature of 174 °C, efficient quasi-phase-matched frequency doubling of the 1064-nm line of a cw diode-pumped Nd:YAG laser was demonstrated. For 204 mW of fundamental pump power, nearly 2 mW of green power was generated at an output wavelength of 532 nm. This result, obtained with nonoptimum focussing conditions, provides a second-harmonic output power almost 40% greater than the theoretical expectation for a similar length of bulk material. The waveguiding properties were shown to be different in the PPLN and the uniform $LiNbO_3$ regions of the sample, with the PPLN grating showing surprisingly robust single-spatial-mode behaviour. These results suggest that the production of longer buried waveguides, potentially incorporating channel structures, could lead to highly efficient nonlinear devices. The ability to work with thin samples may allow shorter periods to be fabricated effectively, thus extending second-harmonic generation to shorter blue wavelengths. More generally, the direct bonding technique offers promise in providing extra degrees of design freedom for nonlinear waveguiding devices.

## REFERENCES

[1] P. G. Harper and B. S. Wherret, "*Nonlinear optics*", Scottish Universities Summer School in Physics 16th, Heriot-Watt University (1975).

[2] P. A. Franken, A. E. Hill, C. W. Peters, and G. Weinreich, "*Generation of optical harmonics*", Physical Review Letters, Vol. 7, No. 4, p.118-119 (1961).

[3] D. A. Kleinmann, "*Nonlinear dielectric ploarisation in optical media*", Physical Review, Vol. 126, p.1977-1979 (1962).

[4] J. A. Armstrong, N. Bloembergen, J. Ducuing, and P. S. Pershan, "*Interactions between light waves in a nonlinear dielectric*", Physical Review, Vol. 127, p.1918-1939 (1962).

[5] M. Houe and P. D. Townsend, "*An introduction to methods of periodic poling for second-harmonic generation*", Journal of Physics D: Applied Physics, Vol. 28, p.1747-1763 (1995).

[6] A. Grisard, E. Lallier, G. Garry, and P. Aubert, "*Ferroelectric integrated optics: recent developments*", IEEE Journal of Quantum Electronics, Vol. 33, No. 10, p.1627-1635 (1997).

[7] J. Webjorn, S. Siala, D. W. Nam, R. G. Waarts, and R. J. Lang, "*Visible laser sources based on frequency doubling in nonlinear waveguides*", Journal of Quantum Electronics, Vol. 33, No. 10, p.1673-1685 (1997).

[8] R. Byer, "*Quasi-phasematched nonlinear interactions and devices*", Journal of Nonlinear Optical Physics and Materials, Vol. 6, No. 4, p.549-592 (1997).

[9] E. Hecht, "*Optics*" 2nd Ed., Addison-Wesley (1987).

[10] J. Wilson and J. F. B. Hawkes, "*Optoelectronics an introduction*" 2nd Ed., Prentice Hall (1989).

[11] M. Bass, P. A. Franken, J. F. Ward, and G. Weinreich, "*Optical rectification*", Physical Review Letters, Vol. 9, No. 11, p.446-448 (1962).

[12] P. A. Franken and J. F. Ward, "*Optical harmonics and nonlinear phenomena*", Reviews of Modern Physics, Vol. 35, No. 1, p.23-39 (1963).

[13] J. A. Giordmaine and R. C. Miller, "*Tunable coherent parametric oscillation in $LiNbO_3$ at optical frequencies*", Physical Review Letters, Vol. 14, No. 24, p.973-976 (1965).

[14] C. C. Wang and G. W. Racette, "*Measurement of parametric gain accompanying optical difference frequency generation*", Applied Physics Letters, Vol. 6, No. 8, p.169-171 (1965).

[15] R. W. Terhune, P. D. Maker, and C. M. Savage, "*Optical harmonic generation in calcite*", Physical Review Letters, Vol. 8, No. 10, p.404-406 (1962).

[16] R. W. Minck, R. W. Terhune, and C. C. Wang, "*Nonlinear Optics*", Applied Optics, Vol. 5, No. 10, p.1595-1612 (1966).

[17] W. Kaiser and C. G. B. Garrett, "*Two-photon excitation in $CaF_2:Eu^{2+}$*", Physical Review Letters, Vol. 7, No. 6, p.229-231 (1961).

[18] G. Eckhardt, R. W. Hellwarth, F. J. McClung, S. E. Schwartz, and D. Weiner, "*Stimulated raman scattering from organic liquids*", Physical Review Letters, Vol. 9, No. 11, p.455-457 (1962).

[19] R. Y. Chiao, C. H. Townes, and B. P. Stoicheff, "*Stimulated brillouin scattering and coherent generation of intense hypersonic waves*", Physical Review Letters, Vol. 12, No. 21, p.592-595 (1964).

[20] D. I. Mash, V. V. Morozov, V. S. Starunov, and I. L. Fabelinskii, "*Stimulated scattering of light of the rayleigh-line wing*", Soviet Physics JETP Letters to the Editor, Vol. 2, p.25-27 (1965).

[21] A. Yariv, "*Quantum electronics*" 3rd Edition, John Wiley and Sons (1989).

[22] A. M. Prokhorov and Y. S. Kuz'Minov, "*Physics and chemistry of crystalline lithium niobate*", Adam Hilger (1990).

[23] G. D. Boyd and D. A. Kleinman, "*Parametric interaction of focussed Gaussian light beams*", Journal of Applied Physics, Vol. 39, No. 8, p.3597-3639 (1968).

[24] V. Pruneri, "*Electric field periodically inverted $LiNbO_3$ for optical frequency conversion*" (Thesis), University of Southampton (1996).

[25] M. Yamada, N. Nada, T. Yamaguchi, M. Saitoh, and K. Watanabe, "*A quasiphase-matched waveguide for the blue second-harmonic generation*", Electronics and Communications in Japan, Part 2, Vol. 77, No. 11, p.206-213 (1994).

[26] V. Pruneri, J. Webjörn, P. St. J. Russell, J. R. M. Barr, and D. C. Hanna, "*Intracavity second harmonic generation of 0.532 μm in bulk periodically poled lithium niobate*", Optics Communications., Vol. 116, p.159-162 (1995).

[27] J. Webjörn, V. Pruneri, P. St. J. Russell, and D. C. Hanna, "*55% conversion efficiency to green in bulk quasi-phase-matching lithium niobate*", Electronics Letters, Vol. 31, No. 8, p.669-671 (1995).

[28] C. B. E. Gawith, D. P. Shepherd, J. A. Abernethy, D. C. Hanna, G. W. Ross, and P. G. R. Smith, "*Second-harmonic generation in a direct-bonded periodically poled $LiNbO_3$ buried waveguide*", Optics Letters, Vol. 24, No. 7, p.481-483 (1999).

[29] G. W. Ross, M. Pollnau, P. G. R. Smith, W. A. Clarkson, P. E. Britton, and D. C. Hanna, "*Generation of high-power blue light in periodically poled $LiNbO_3$*", Optics Letters, Vol. 23, No. 3, p.171-173 (1998).

[30] V. Pruneri, R. Koch, P. G. Kazansky, W. A. Clarkson, P. St. J. Russell, and D. C. Hanna, "*49 mW of cw blue light generated by first-order quasi-phase-matched frequency doubling of a diode-pumped 946-nm Nd:YAG laser*", Optics Letters, Vol. 20, No. 23, p.2375-2377 (1995).

[31] J. Amin, V. Pruneri, J. Webjörn, P. St. J. Russell, D. C. Hanna, and J. S. Wilkinson, "*Blue light generation in a periodically poled Ti:$LiNbO_3$ channel waveguide*", Optics Communications, Vol. 135, p.41-44 (1997).

[32] M. de Micheli, J. Botineau, P. Sibillot, D. B. Ostrowsky, and M. Papuchon, "*Fabrication and characterisation of titanium indiffused proton exchanged (TIPE) waveguides in lithium niobate*", Optics Communications, Vol. 42, No. 2, p.101-103 (1982).

[33] T. Fujiwara, R. Srivastava, X. Cao, and R. V. Ramaswamy, "*Comparison of photorefractive index change in proton-exchanged and Ti:indiffused $LiNbO_3$ waveguides*", Optics Letters, Vol. 18, No. 5, p.346-348 (1993).

[34] P. Baldi, M. P. de Micheli, K. E. Hadi, S. Nouh, A. C. Cino, P. Aschieri, and D. B. Ostrowsky, "*Proton exchanged waveguides in $LiNbO_3$ and $LiTaO_3$ for integrated lasers and nonlinear frequency converters*", Optical Engineering, Vol. 37, No. 4, p.1193-1202 (1998).

[35] P.J. Mathews, A. R. Mickelson, and S. W. Novak, "*Properties of proton exchange waveguides in lithium tantalate*", Journal of Applied Physics, Vol. 72, No. 7, p.2562-2574 (1992).

[36] K. K. Wong, "*An experimental study of dilute melt proton exchange waveguides in x- and z- cut lithium niobate*", GEC Journal of Research, Vol. 3, No. 4, p.243-250 (1985).

[37] J. Haisma, G. A. C. M. Spierings, U. K. P. Biermann, and A. A. van Gorkum, "*Diversity and feasibility of direct bonding: a survey of a dedicated optical technology*", Applied Optics, Vol. 33, No. 7, p.1154-1169 (1994).

[38] K. Eda, M. Sugimoto, and Y. Tomita, "*Direct heterobonding of lithium niobate onto lithium tantalate*", Applied Physics Letters, Vol. 66, No. 7, p.827-829 (1995).

[39] M. J. Missey, V. Dominic, L. E. Myers, and R. C. Eckardt, "*Diffusion-bonded stacks of periodically poled lithium niobate*", Optics Letters, Vol. 23, No. 9, p.664-666 (1998).

[40] Y. Tomita, M. Sugimoto, and K. Eda, "*Direct bonding of $LiNbO_3$ single crystals for optical waveguides*", Applied Physics Letters, Vol. 66, No. 12, p.1484-1485 (1995).

[41] J. Haisma, T. M. Michelsen, and F. J. H. M. van der Kruis, "*Silicon-wafer fabrication and (potential) applications of direct-bonded silicon*", Philips Journal of Research, Vol. 49, p.65-89 (1995).

[42] C. T. A. Brown, C. L. Bonner, T. J. Warburton, D. P. Shepherd, A. C. Tropper, and D. C. Hanna, "*Thermally bonded planar waveguide lasers*", Applied Physics Letters, Vol. 71, No. 9, p.1139-1141 (1997).

[43] D. H. Jundt, "*Temperature-dependent Sellmeier equation for the index of refraction, $n_e$, in congruent lithium niobate*", Optics Letters, Vol. 22, No. 20, p.1553-1555 (1997).

[44] K. S. Abedin and H. Ito, "*Temperature-dependent dispersion relation of ferroelectric lithium tantalate*", Journal of Applied Physics, Vol. 80, No. 11, p.6561-6563 (1996).

[45] Y. S. Kim and R. T. Smith, "*Thermal expansion of lithium tantalate and lithium niobate single crystals*", Journal of Applied Physics, Vol. 40, No. 11, p.4637-4641 (1969).

[46] G. A. C. M. Spierings, J. Haisma, and T. M. Michelsen, "*Surface-related phenomena in the direct bonding of silicon and fused-silica wafer pairs*", Philips Journal of Research, Vol. 49, p.47-63 (1995).

# Chapter 4
# NONRECIPROCAL TRANSMISSION IN A DIRECT-BONDED PHOTOREFRACTIVE Fe:$LiNbO_3$ BURIED WAVEGUIDE

## 4.1 Introduction

Photorefractivity is among the most important properties of lithium niobate, causing a localised change in refractive index when the crystal is exposed to light [1]. The first observation of this phenomenon was reported by Ashkin et al. in 1966 [2] after an experiment in which laser beams transmitted through $LiNbO_3$ and $LiTaO_3$ became defocused and the crystals appeared to be damaged by the light. Originally dubbed "optical damage" and "highly detrimental to the optics of nonlinear devices based on these materials" [2], this effect was soon discovered to be thermally erasable and the use of lithium niobate as a holographic storage medium for optical data was proposed [3]. The first explanation of the optically induced refractive index change then came in 1968 when Chen et al. presented a drift transport mechanism for the migration of free charges under the influence of an internal electric field [3]. Advancements to this model came as Staebler and Amodei considered diffusion as a second charge transport mechanism in 1972 [4] and Glass introduced the idea of a unidirectional light induced current, the photovoltaic effect, in 1974 [5]. It was not until 1979 however, that Kukhtarev et al. published a band transport model describing the successive stages of excitation, migration, and recombination of photogenerated charge carriers, which would become the most widely accepted explanation of the photorefractive effect to date [6-7].

Since its discovery, the photorefractive effect has proven to be both a blessing and a curse for optical interactions in lithium niobate, causing beam distortion in frequency doubling and electro-optic experiments [2], while leading to important advances in nonlinear optics such as holography [3,8-9], optical data processing [10-11], two-wave mixing [12-13] and nonreciprocal transmission [14-17]. One application of this advancement has been in the field of optical limiting, where a photorefractive material can be used to create a one-way window that favours transmission of coherent light from one side while blocking it from the other [14]. As the emphasis shifts from high-power pulsed lasers that can drive a wide range of nonlinearities, to low-power

continuous wave (cw) lasers, the development of materials and devices for efficient optical limiting at low input intensities has attracted scientific interest worldwide [18-19]. Fixed line filters (such as laser safety goggles) for example, make excellent optical limiters for low-power cw lasers of a specified wavelength, but can prove ineffective for use with widely tunable sources. The preferred solution is to develop self-activating optical limiting materials capable of automatically adapting to any wavelength within a specified range [20]. One such material is iron-doped lithium niobate, a photorefractive crystal that has already demonstrated the potential to provide a high degree of optical limiting for a wide range of lasers and wavelengths [17,20-21].

This chapter describes the origin of the photorefractive effect in iron-doped lithium niobate and its application towards producing efficient optical limiting devices in direct-bonded waveguide structures. The work presented was performed in collaboration with Gary Cook [20-23] under a Defence Evaluation and Research Agency (DERA) CASE award, and was undertaken as a feasibility study towards producing waveguide arrays for high speed optical limiting applications with low power cw lasers. Reviewed in this chapter are the material considerations governing the optimisation of photorefractivity and nonreciprocal transmission in lithium niobate crystals, the fundamentals of which are applied towards the design and characterisation of a buried planar waveguide device. The fabrication procedure used to bury a photorefractive iron-doped lithium niobate (Fe:$LiNbO_3$) waveguide in non-photorefractive magnesium-doped lithium niobate (MgO:$LiNbO_3$) by direct bonding [24-25] and precision polishing techniques is presented in full. Finally, the optical limiting characteristics of a buried Fe:$LiNbO_3$ planar waveguide device are described.

## 4.2 The photorefractive effect

The photorefractive effect is an optical phenomenon whereby the refractive index of a material is changed in proportion to gradients of incident light intensity [1]. In order for a crystal to exhibit the photorefractive effect it must be photoconductive or photovoltaic in nature, allowing an electric field to be optically induced within the material, and also electro-optic, to provide a subsequent change in refractive index [26]. The photorefractive effect is observed in all ferroelectric crystals, with the charge

transport mechanism being dominated by either diffusion [4] or the photovoltaic effect [5], and some paraelectric materials wherein the photorefractive effect can be induced by an externally applied electric field via a charge drift transport mechanism [3]. While many photorefractive materials exist, including the aforementioned ferroelectrics ($LiNbO_3$ [2], $LiTaO_3$ [2], $BaTiO_3$ [15], SBN [27], $KNbO_3$ [16], etc.), the semiconductor GaAs [28] and even some polymer materials [29], this chapter focuses on photorefractive processes in iron-doped lithium niobate, which has recently emerged as a good material for optical limiting applications, having the highest optical gain coefficient reported for any crystalline photorefractive material (100 $cm^{-1}$) [21] and large photovoltaic nonlinearities [17].

It has been widely accepted that the origin of the photorefractive effect in lithium niobate is the presence of iron impurities within the material [1,6,30]. Iron enters the crystal lattice during sample growth as either $Fe^{2+}$ or $Fe^{3+}$ ions, and it is the relative concentration of these two ionic species that determines the photorefractive susceptibility of the material [31]. The mechanism behind the photorefractive effect in iron-contaminated lithium niobate is usually described by the relation [30]

$$Fe^{2+} + h\upsilon \Leftrightarrow Fe^{3+} + e^{-} \tag{4.1}$$

where $h$ is Planck's constant, $\upsilon$ is the frequency of the incident beam and $e$ is the electron charge. The associated band transport model [6] assumes that the material has a pool of charges located in shallow $Fe^{2+}$ traps which are able to be excited into the conduction band upon illumination (Figure 4.1). In a uniformly illuminated area, the charges randomly re-distribute themselves and are unable to settle back into $Fe^{3+}$ traps due to constant re-excitation from the light. However, when two laser beams interfere in a photorefractive media, the highly mobile charges excited by bright interference fringes migrate under the influence of diffusion, or any internal or external electric

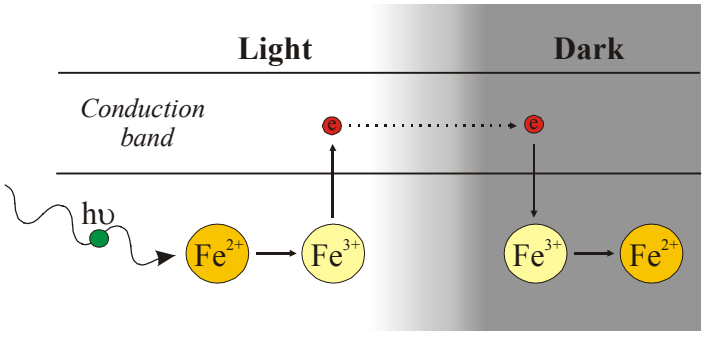


**Figure 4.1:** Photorefractive charge transfer of photoexcited electrons in Fe:$LiNbO_3$ [20].

fields, until captured by a trap in a darker region [20]. At a steady state, charges excited into the conduction band in high intensity areas will migrate towards areas of lower intensity, creating a periodic space-charge distribution, $\rho_{sc}$, and an associated periodic electric field, $E_{sc}$, from the relation [26]

$$E_{sc} = \int \rho_{sc} dx \,. \tag{4.2}$$

The photorefractive effect is illustrated in Figure 4.2, demonstrating the relationship between intensity, space charge distribution, electric field, and an associated refractive index change when two beams interfere in a photorefractive material. It is the electro-optic nature of lithium niobate that gives rise to this final effect, allowing the refractive index of the material to be changed via the linear Pockel's effect [32]

$$\Delta n = -\tfrac{1}{2} n^3 r_{eff} E \tag{4.3}$$

where $r_{eff}$ is the appropriate electro-optic coefficient as determined by the direction of beam propagation through the crystal. The resulting holographic refractive index grating is phase shifted by 90 degrees with respect to the light interference pattern, allowing power to be coupled from one interfering beam to the other due to simultaneous Bragg scattering of the two input beams from the refractive index grating and into each other [12].

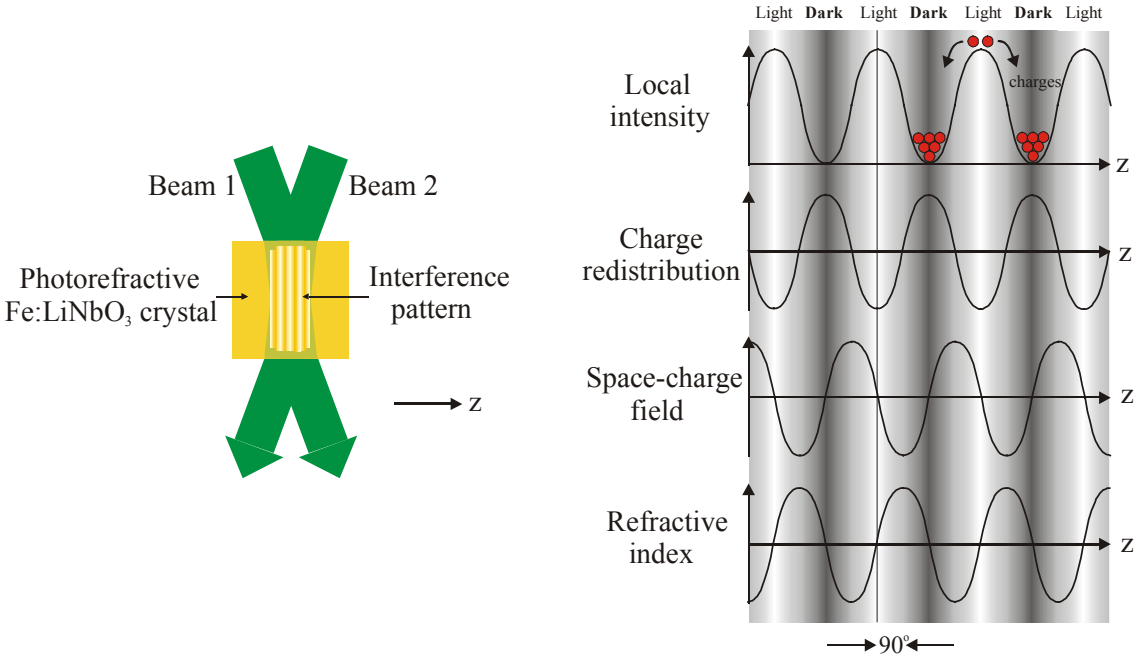


**Figure 4.2:** The photorefractive effect. The interference pattern formed by two coherent laser beams interfering in an electro-optic crystal causes photoexcited charges in brighter regions to migrate to regions of lower intensity. The resulting periodic space charge field induces a refractive index grating in the crystal via the electro-optic effect which is phase shifted by 90° relative to the incident light [20].

## 4.3 Material considerations

In most photorefractive materials, the magnitude of the nonlinear effect is independent of incident laser intensity [20]. Hence, when two beams interfere in lithium niobate, the maximum refractive index change attainable between light and dark interference fringes is also independent of laser intensity. The explanation is linked to the charge excitation process, which is limited due to the finite number of charges, and charge traps, available within the photorefractive material [30]. Once all of the charges have been photoexcited out of illuminated trap sites and diffused away into the darker areas of the material, no further build-up of the space charge field is possible and the maximum change of refractive index is obtained. The magnitude of the photorefractive effect therefore depends on the relative content of $Fe^{2+}$ charge donors and $Fe^{3+}$ traps within the material, with increased intensity speeding up charge generation and grating formation [26,30].

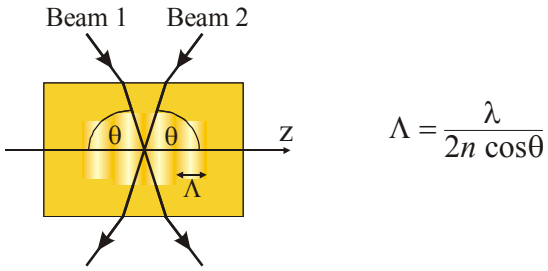


**Figure 4.3:** Two beams interfering within a photorefractive crystal to induce a holographic reflection grating of period, Λ [33].

Charge-trap density also determines the efficiency of two-beam coupling in lithium niobate by placing a physical limit on the maximum space-charge field attainable by diffusion, $E_d$, and thus the two-beam coupling gain, Γ, via the relation [17]

$$\Gamma = \frac{2\pi}{n\lambda} r_{eff} E_d \tag{4.4}$$

where $E_d \sim E_{sc}$ in a diffusion-dominated system [17,26]. Here, $E_d$ is inversely proportional to the period of the holographic grating, Λ, which is usually chosen to maximise the photorefractive response for a given material, laser wavelength, and intersection angle of the two interfering beams (Figure 4.3) [33]. It would therefore seem logical to maximise both the diffusion field and two-beam coupling efficiency by use of the finest possible grating spacing, as per the relation [20]

$$E_d = \frac{2\pi k_b T}{e\Lambda} \tag{4.5}$$

where $k_b$ is Boltzmann's constant and $T$ is the absolute temperature of the crystal. However, variations in charge-trap density lead to an optimum grating spacing for each photorefractive material, operation below which results in saturation of the space charge field and reduced coupling efficiency between the two interfering beams [30]. In the case of lithium niobate, where the photorefractive effect is dominated by charge diffusion, the optimum grating spacing, $\Lambda_{opt}$, is given by [20]

$$\Lambda_{opt} = 2\pi\sqrt{\frac{\varepsilon_s k_b T}{e^2 N_A^-}} \tag{4.6}$$

where $\varepsilon_s$ is the static permittivity and $N_A^-$ is the electron trap density.

In general, the charge-trap density of a photorefractive material is determined by the small amount of metal impurities included in the melt during crystal growth. In the case of iron-doped lithium niobate, it is the $Fe^{2+}$ ions that act as the absorbing species for electron generation, while the transparent $Fe^{3+}$ ions act as electron traps (Figure 4.1). Optimisation of the balance between donors and traps is achieved by oxidisation or reduction of the iron-doped crystal and can be monitored via the linear transmission characteristics of the material [30]. Experiments performed previously by Cook et al. demonstrate that $LiNbO_3$ crystals doped with iron concentrations of between 0.02 mol.% and 0.09 mol.%, and a linear transmission of between 30 % and 60 %, include sufficient trap density for any grating spacing in the visible spectrum [20,22].

### 4.4 Nonreciprocal transmission

In high charge-trap density photorefractive materials, two-beam coupling efficiency can be optimised by use of the finest period holographic gratings without saturation of the local space charge field (Equation 4.6). As the smallest interference fringe spacing is obtained when the angle between interfering beams is 180 degrees, highly efficient two-beam coupling can be performed when the pump and signal beams propagate and interfere along a single axis of a photorefractive crystal [15-17,21]. While such an arrangement can be readily achieved by the use of two independent laser beams [14], an effective and simple solution is to interfere an input beam with its own Fresnel reflection from the rear of the crystal [15], as illustrated in Figure 4.4. In Fe:$LiNbO_3$, this counter-propagating beam geometry is best operated along the z-axis of the crystal

where the holographic grating can access the highest effective electro-optic coefficient of the material, $r_{eff} = \pm r_{13} \approx 9.6$ pm $V^{-1}$ [17]. Here, the sign of the electro-optic coefficient gives rise to unidirectional coupling gain in either the forward or backward directions of the crystal, depending on the orientation of the crystal z-axis. Operation in this direction also allows the maximum contribution to beam coupling through the photovoltaic effect, which is due to the asymmetric placement of Li and Nb ions in the Fe:$LiNbO_3$ crystal lattice causing preferential charge displacement of photoexcited electrons along the +z-direction [5,34]. When the crystal is oriented for forward gain, the reflected signal beam is attenuated into the input beam direction such that the transmitted intensity actually increases slightly with time by compensating for back reflection [34]. Backward gain causes the reflected signal beam to be amplified at the expense of the input laser beam, quickly diminishing the transmitted intensity from the photorefractive crystal [34]. This effect is known as nonreciprocal transmission and is demonstrated in the photographs and intensity profiles provided in Figure 4.5.

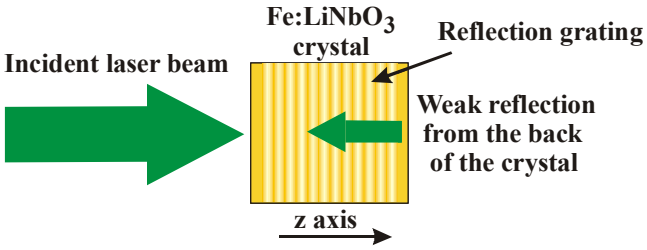


**Figure 4.4:** Two beam coupling in a counter-propagating beam geometry in Fe:$LiNbO_3$ [15,22].

Nonreciprocal transmission in Fe:$LiNbO_3$ is very pronounced and has recently received considerable attention as a means of achieving rapid optical limiting of tunable continuous wave lasers [17-20]. Performing as a one-way window that favours transmission of coherent light from one side while blocking it from the other [14], Fe:$LiNbO_3$ in a counter-propagating beam geometry allows simple self-referencing of the input beam and its Fresnel reflection, automatically adapting to any wavelength within the visible range of light while eliminating the need for beam splitters and other ancillary optics usually associated with two-beam coupling processes [22]. The uniaxial crystal structure of Fe:$LiNbO_3$ also renders this process insensitive to input polarisation. With both the pump and signal beams propagating along the same axis of the crystal, another major advantage of this arrangement is that the beams can be

tightly focussed without the loss of spatial overlap, providing the increased interaction length and local intensity associated with faster response times [20].

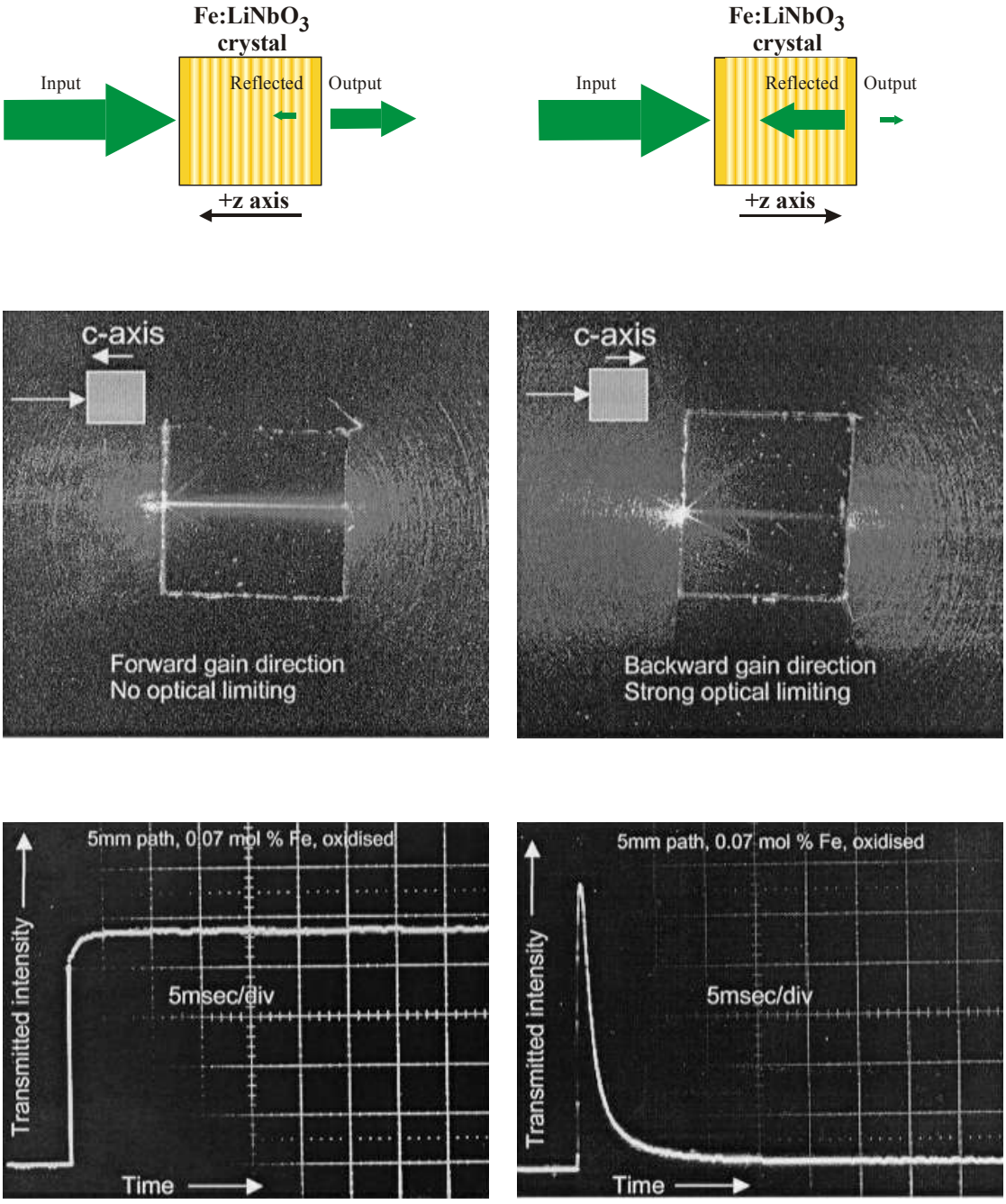


**Figure 4.5:** Nonreciprocal transmission and optical limiting effects with Fe:LiNbO$_3$ in a counter-propagating beam geometry. Images to the left demonstrate beam transmission through the crystal, while images to the right demonstrate the beam blocking associated with optical limiting. Photographs and oscillogram traces are reprinted with permission of Gary Cook [34].

## 4.5 Optical limiting and dark conductivity

Optical limiting based upon a counter-propagating beam geometry in Fe:$LiNbO_3$ includes an intensity dependence intrinsic to the function of rapidly coupling light back out of the crystal [20]. As the holographic grating is written, successively more of the input beam becomes blocked from the rear of the crystal and the intensity of the Fresnel reflection decreases with time. What little intensity remains must compete with the natural thermal excitation of charges, also known as dark conductivity, which gradually empties the shallow trap sites to erase the refractive index grating [10]. At low input intensities, where the Fresnel reflection can become very weak, dark conductivity dominates the rear of the crystal and the optical limiting efficiency is low. At higher intensities the effects of dark conductivity are overcome and the optical limiting efficiency is high. Efficient optical limiting in Fe:$LiNbO_3$ therefore requires that the rate of photoinduced charge generation and trapping used to write a holographic grating must be greater than the erasure rate of dark conductivity [20].

Dark conductivity exists in all photorefractive materials and effectively determines the fundamental limit of how long a holographic grating can be stored in a crystal [10]. While iron-doping actually raises the dark conductivity of lithium niobate (as will most impurities), the increased charge-trap density associated with the incorporation of Fe ions into the crystal lattice provides the greatest two-beam coupling efficiency and optical limiting in this material, while preserving relatively long storage times for holographic data recording (of many months) [21]. Fe:$LiNbO_3$ also provides wide spectral coverage and can be used for optical limiting throughout the visible range of wavelengths, from the deep blue (below ~ 420 nm absorption in the crystal becomes large and the Fresnel reflection is severely diminished) and well into the red (above ~ 670 nm the absorption becomes too small to generate enough charges to form a reflection grating) [22,30]. Conversely, magnesium is highly effective for increasing the dark conductivity of lithium niobate, with dopant concentrations of around 5 % eliminating the photorefractive effect and associated optical distortion in this material (for use in frequency doubling experiments etc.) [35]. Dark conductivity can also be increased by the application of heat, and holographic data can be completely erased from Fe:$LiNbO_3$ with an annealing treatment of 200 °C or more [3].

At high intensities, where the photogeneration rate is much higher than the erasure rate from dark conductivity, optical limiting occurs with a response time inversely proportional to intensity such that the rate of decline is rapid at first but becomes progressively slower as the intensity decays throughout the material [20]. This effect is illustrated in Figure 4.6, providing a typical transmission profile and two figures of merit for optical limiting processes. The first figure of merit is the response speed of the material, $\tau_r$, which is defined as the time taken for the transmitted intensity to reach 1/e of its original value, and for which faster reaction times are preferred [20]. Secondly, the relative change in optical density, $\Delta OD$, determines the ability of each photorefractive material to block the transmission of coherent light for a given wavelength and incident intensity [20]. This is taken as a ratio between the peak transmitted intensity at the time of exposure, $I_P$, and the steady state transmitted intensity at a time much greater than the 1/e response time, $I_{SS}$, via the equation [20]

$$\Delta OD = \log_{10}\left(Ip / Iss\right) \tag{4.7}$$

with higher values indicating stronger optical limiting performance.

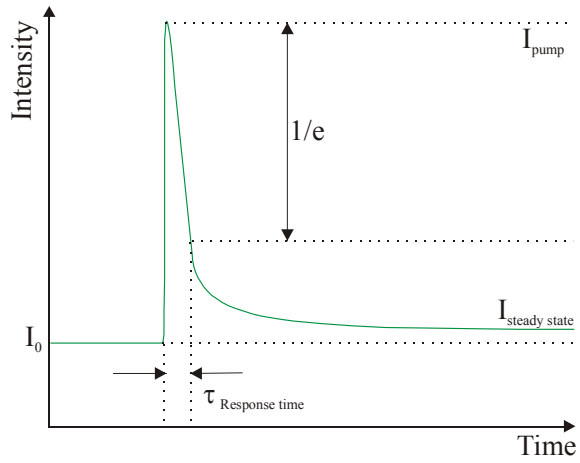


**Figure 4.6:** Transmission characteristics for counter-propagating beam geometry-based optical limiting processes in photorefractive crystals.

## 4.6 Focussing conditions

In general, optical limiting performance depends on the intensity, focussing conditions, and device length used for each photorefractive material. In the case of Fe:$LiNbO_3$, typical working intensities range from 100 W $cm^{-2}$ to 10 kW $cm^{-2}$ [17,20] and are best achieved by placing the crystal at the focal plane of a lens. At small system apertures of f/20 or less, bulk Fe:$LiNbO_3$ crystals have been found to work

exceedingly well in a focal plane geometry. For example, a 5-mm-long 0.07 mol.% iron-doped sample gives a $\Delta OD$ of 3.8 with a 1/e response time of 1.9 milliseconds using a f/20 lens and input intensity of 9 kW $cm^{-2}$ at 532 nm (this is the highest reported $\Delta OD$ reported in any photorefractive crystal to date [21]). However, at wider apertures where the confocal parameter becomes less than the crystal path length, the degree of optical limiting decreases rapidly, becoming negligible towards larger apertures, such as f/1 [22]. This effect is thought to arise from competition between grating formation and dark conductivity in the lower-intensity areas away from the beam waist, where charges that have settled into traps within dark interference fringes are randomly redistributed back into lighter areas (Figures 4.7a and 4.7b) [10]. Subsequent erasure of the refractive index grating reduces the effective optical interaction length for two beam coupling in the crystal, slowing the response speed and reducing the optical limiting efficiency [22]. Dark conductivity also affects the optimum device length of the bulk material, necessitating a balance between intensity dependence and interaction length for efficient optical limiting in a focal plane geometry, with device lengths of between 3 mm and 6 mm giving the best results [20]. An ideal solution therefore, is to replace bulk Fe:$LiNbO_3$ with a photorefractive optical waveguide in which the interaction length can be made arbitrarily long and the focussed intensity can be increased by the use of wide aperture lenses (Figure 4.7c) [22].

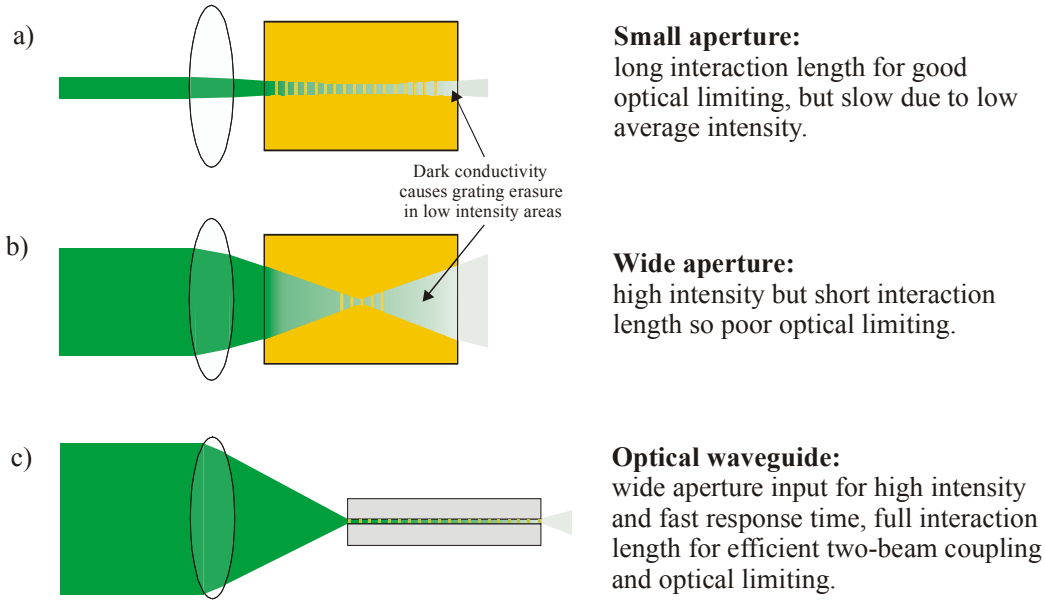


**Figure 4.7:** Focussing conditions versus dark conductivity, and their affect upon device performance, in a) small aperture and b) wide aperture systems, and how they may be improved in c) an optical waveguide geometry [22].

## 4.7 Fe:$LiNbO_3$ waveguides

The development of Fe:$LiNbO_3$ into a an optical fiber provides an attractive route towards fast and efficient optical limiting in low power laser systems [22]. In an arrangement where the use of wide aperture focussing lenses is usually restricted due to the effects of dark conductivity, the optical confinement offered by a fiber geometry would provide an arbitrarily long interaction length between pump and signal beams for increased two-beam coupling and optical limiting efficiency, while allowing access to the very high intensities developed by fast optical systems [22]. Unfortunately, the research and development of such technology is a costly endeavour, due to the intrinsic difficulties involved with forming single crystal fibers [22]. It would therefore be advantageous to provide preliminary evidence of improved optical limiting efficiency with increased intensity confinement, to be determined largely by the change in optical density and response speed for the device, as can be obtained using simpler waveguide geometries based upon planar and channel waveguide devices.

To date, several fabrication techniques have been explored towards the development of planar and channel waveguide devices in Fe:$LiNbO_3$. The simplest of these structures are developed from the bulk material, such as very thin layers of material polished down to waveguide dimensions [22] or mechanically diced parallel slabs [36], and represent the most cost effective means of producing large numbers of waveguides very quickly. However, while such structures do show some improvement over the bulk material, the feature size attainable by such techniques is limited (~ 20 μm for polishing and 50 μm for dicing) and prone to high losses due to surface defects. Light induced frustrated etching (LIFE) [37] provides smoother waveguide structures in wafer material by applying high intensity light (100 $Wcm^{-2}$ @ 488nm) to selectively suppress etching of the –z surface in a HF:$HNO_3$ (2:1) mix [38], although these features are thus far too small for waveguiding applications. More direct chemical modification of Fe:$LiNbO_3$ wafers uses proton exchange to replace $Li^+$ ions from the crystal with $H^+$ ions from heated benzoic acid, raising the refractive index for channel confinement, while unfortunately lowering the photorefractivity of the crystal [39]. Other technologies, including epitaxial growth of thin Fe:$LiNbO_3$ films onto suitable substrates, micro-Czochralski growth of

Fe:$LiNbO_3$ single crystal optical fibers, and the suspension of small crystal particles in a glass host, provide great potential for future devices in this material [22], however an efficient waveguide device for optical limiting in Fe:$LiNbO_3$ has not been previously demonstrated.

To this end, the remainder of this chapter describes our initial study towards producing an Fe:$LiNbO_3$ photorefractive waveguide device buried in MgO:$LiNbO_3$ by direct bonding [24-25] and precision polishing techniques. Previously applied methods of waveguide manufacture in this material, such as mechanical sawing [36], proton exchange [39] and LIFE [37], have resulted in high losses, no optical limiting, and undersized features, respectively. By contrast, direct bonding has been previously used in the design and realisation of highly efficient lithium niobate waveguide devices [40-41]. Here, the combination of a photorefractive Fe:$LiNbO_3$ waveguide with direct-bonded non-photorefractive MgO:$LiNbO_3$ cladding layers has resulted in an efficient buried waveguide device for optical limiting experiments.

### 4.8 Fabrication of a direct-bonded Fe:$LiNbO_3$ buried waveguide device

Fabrication of the waveguide device began with a sample of $LiNbO_3$ doped with 0.08 mol.% of iron. Provided that the crystal has a sufficiently high electron-trap density, optical limiting in Fe:$LiNbO_3$ is insensitive to the total Fe content (at least over the doping range of 0.02 mol.% to 0.09 mol.% [20]), and depends mainly on the linear transmission characteristics of the crystal, which in turn depend on the relative densities of the $Fe^{2+}$ and $Fe^{3+}$ oxidation states of the iron doping [30]. Magnesium-doped lithium niobate was chosen for both the substrate and cladding layers of our buried waveguide device as this material has a refractive index lower than that of either undoped lithium niobate or Fe:$LiNbO_3$ [42] and features similar thermal properties to those of the iron-doped waveguide layer, an important prerequisite when annealing bonds at high temperatures [24]. An additional benefit of MgO:$LiNbO_3$ is that the magnesium dopant increases the dark conductivity of the crystal, effectively suppressing the photorefractive effect in these layers and ensuring that all nonreciprocal transmission will occur in the buried waveguide region of our device only. For this experiment 5 mol.% of magnesium was added to the melt during crystal growth, a value associated with photorefractive resistance in lithium niobate [35].

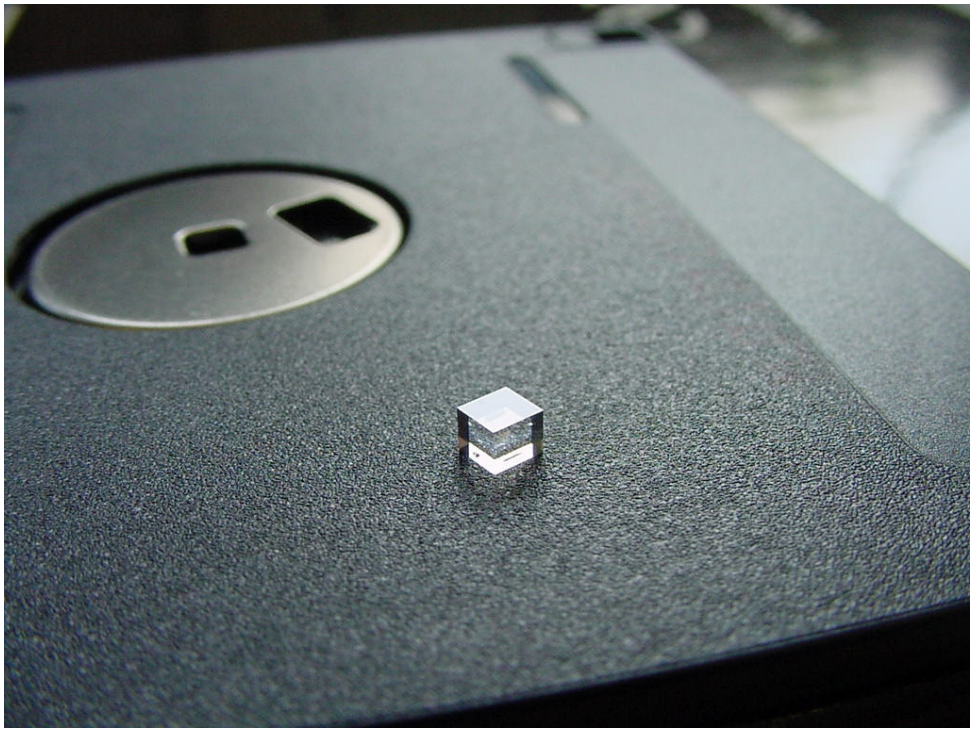

**Figure 4.8:** A photograph of a direct-bonded Fe:LN buried waveguide device.

From each crystal type a 1-mm-thick x-cut substrate of 6 mm × 6 mm surface area was diced and polished to provide an optically flat surface suitable for direct bonding. After cleaning, a mixture of $H_2O_2$-$NH_4OH$-$H_2O$ (1:1:6), followed by several minutes of rinsing in deionised water, was applied to both materials in order to render their surfaces hydrophilic [43]. The Fe:$LiNbO_3$ and MgO:$LiNbO_3$ layers were then brought into contact at room temperature, with both samples aligned along the same crystalline orientation, and finger pressure applied in order to promote adhesive avalanche [44]. This effect forces any excess air or liquid from between the two substrates, as demonstrated by the elimination of the interference fringes at the crystal interface. Annealing of the bonded sample at 350 °C for 6 hours provided a sufficient bond strength for further machining and the Fe:$LiNbO_3$ region was then polished down to obtain a waveguiding layer of 20-μm-thickness with a variance of less than 1 μm across the entire layer. A further cladding layer of MgO:$LiNbO_3$ was then added with the same procedure as above. The device was completed by removing any residual unbonded edge regions with dicing equipment and polishing the end faces of the waveguide to a parallel optical finish (Figure 4.8). The final dimensions of the buried Fe:$LiNbO_3$ waveguide device are given in Figure 4.9.

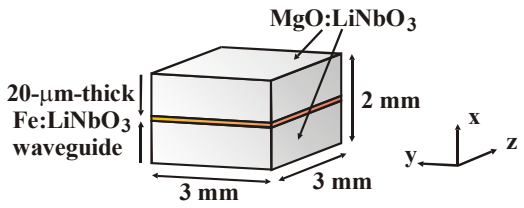


**Figure 4.9:** Schematic diagram of the direct-bonded Fe:$LiNbO_3$ buried waveguide device.

## 4.9 Device characterisation

Measurement of nonreciprocal transmission in our Fe:$LiNbO_3$ waveguide was performed using two-beam coupling in a counter-propagating beam geometry, a technique illustrated in Figure 4.4. This allows the signal beam to be derived from the weak Fresnel reflection of the incident beam at the exit face of the crystal [15], eliminating the need for beam splitters and other ancillary optics. The device is inserted into the beam such that the incident light propagates along the +z-axis of the crystal, providing access to the highest effective electro-optic coefficient of lithium niobate, $r_{eff} = \pm r_{13} \approx 9.6$ pm $V^{-1}$ [17]. For this experiment a continuous wave 532 nm frequency-doubled Nd:YAG laser source was first pre-expanded and collimated to over-fill a well corrected f/5 spherical lens. With a focussed spot size of ~ 6.5 μm diameter, this arrangement allows very high input intensities to be focussed into the waveguide at low incident pump powers, an input of just 25 mW gives a focussed intensity of 80 kW $cm^{-2}$ for example. This technique also provides an approximately uniform beam for focussing onto the front face of the buried Fe:$LiNbO_3$ waveguide and avoids any ambiguity over the actual f-number arising from the use of a Gaussian beam. The focussed spot was therefore an Airy pattern rather than a Gaussian, and only the central lobe contained within the first minima of the Airy pattern was launched into the waveguide. While a cylindrical lens would be more appropriate for use with our multimode planar waveguide, allowing reduction of beam divergence in the unguided direction and thus a more uniform beam intensity along the crystal length, a spherical lens was used in this experiment owing to the large aberrations present in our available cylindrical lenses. A fast-response shutter mechanism was used to block the pump beam prior to each crystal exposure and a photodiode was used to measure the far-field transmission characteristics of the device. This allows separation of the optical limiting transmission and any surrounding noise with a variable pinhole. A diagram of the full launch arrangement is given in Figure 4.10.

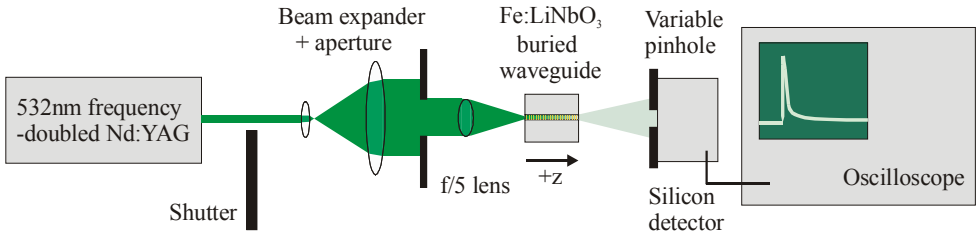


**Figure 4.10:** Experimental arrangement for optical limiting with counter propagating beams in a buried Fe:$LiNbO_3$ waveguide (side view).

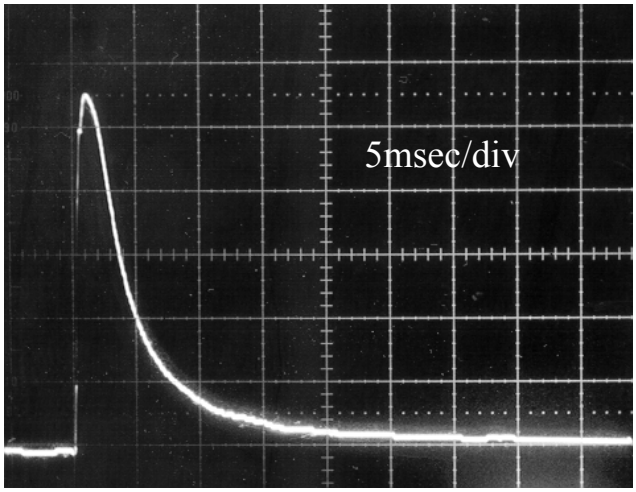


**Figure 4.11:** An oscillograph trace demonstrating far field optical limiting in the Fe:$LiNbO_3$ buried waveguide at 80 kW $cm^{-2}$ peak focussed intensity at $\lambda$ = 532 nm.

Upon exposure, the pump transmission in the waveguide declines due to the formation of a volume reflection grating in the photorefractive material as the pump and signal beams interfere. This effect is demonstrated in the oscillograph of Figure 4.11, from which the relative change in optical density obtained by optical limiting is determined via Equation 4.7. For our arrangement, an input focussed intensity of approximately 80 kW $cm^{-2}$ gave a measured $\Delta OD$ of 2 and 1/e response time of 4.9 milliseconds in the Fe:$LiNbO_3$ buried waveguide. This result represents a significant improvement over the bulk material at large apertures, with approximately 20 times less steady-state output transmission and 60 times faster optical limiting response than similar bulk crystals. This was confirmed with a 2.7-mm-long bulk $LiNbO_3$ crystal doped with 0.07 mol.% of iron, which gave a $\Delta OD$ of 0.71 and 1/e response time of 298 milliseconds in the same launch arrangement. Similarly, a 3.6-mm-long $LiNbO_3$ crystal co-doped with 0.03 mol.% of iron and 0.05 mol.% of terbium (a composition designed to increase photorefractive response times in lithium niobate [45]) gives a $\Delta OD$ of just 0.64 with a 1/e response time of 289 milliseconds. However, the intensity

required to achieve millisecond order response times in our photorefractive waveguide was higher than expected from similar experiments with bulk Fe:$LiNbO_3$ crystals [20], indicating non-optimised launch conditions or a possible change in local material properties during the direct bonding process. Since optical limiting in Fe:$LiNbO_3$ is intensity dependent in a counter-propagating beam arrangement, the first of these problems is likely to arise from the spherical lens used to focus light into the waveguide (Figure 4.10). Beam divergence in the unguided plane will rapidly reduce the pump intensity with distance in wide aperture systems, followed by a subsequent decrease in the $\Delta OD$. This deleterious effect would not occur in a channel waveguide geometry, where the beam shape is preserved throughout the length of the device, allowing faster response times and greater optical limiting efficiency at lower input intensities for future devices.

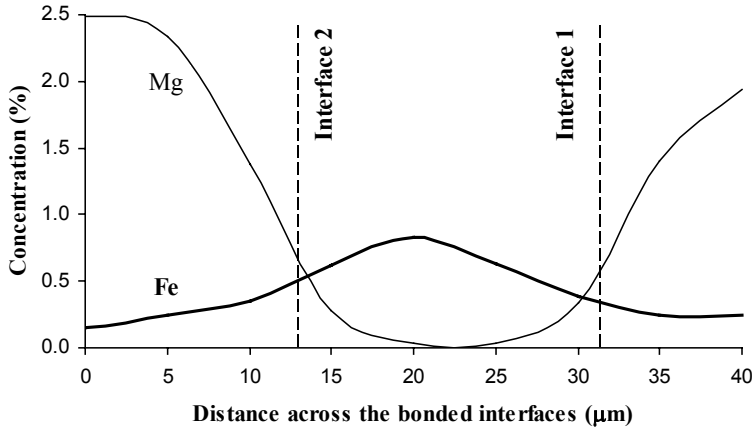


**Figure 4.12:** Chemical composition versus distance across the direct-bonded interfaces of an Fe:$LiNbO_3$ buried waveguide device. The nonsymmetrical diffusion profile arises as a result of the two annealing processes required to complete the three-layered device.

Investigation of the material properties of our direct bonded sample was performed using a scanning electron microscope (SEM) based compositional line profile analysis, a technique further described in Chapter 5. While the absolute resolution of the SEM is limited by the micron-order spot size of the probing electron beam, the measurement is sufficient to illustrate the relative changes in iron and magnesium concentrations across the polished end face of our device, the results of which are given in Figure 4.12. The graph shows significant inter-diffusion of iron and magnesium ions across the two bonded interfaces of the sample, indicating ion-exchange between the atomically-contacted substrate layers. Such a change in chemical composition is due

to the high-temperature annealing used in direct bonding [46] and represents a possible degradation mechanism for the optical limiting efficiency of the Fe:$LiNbO_3$ waveguide layer. For example, reduced iron content leads to reduced photoconductivity, electron trap density and charge generation and recombination rates, reducing the coupling gain and slowing down the response time of the photorefractive material. Further, the presence of magnesium at the edges of the buried waveguide suppresses the photorefractive effect in these areas, reducing the active volume of the waveguide layer. This again reduces the average two-beam coupling gain and increases the input intensity needed to achieve a given reduction in optical transmission. However, optimisation of material composition and annealing conditions should reduce these effects in future devices.

## 4.10 Conclusions

In conclusion, this chapter describes the fabrication of a 20-μm-thick photorefractive Fe:$LiNbO_3$ waveguide buried in MgO:$LiNbO_3$ by direct bonding and precision polishing techniques. Characterisation of optical limiting in this device was performed using two-beam coupling in a counter-propagating beam geometry with a 532 nm cw frequency-doubled Nd:YAG laser source. For an input focussed intensity of approximately 80 kW $cm^{-2}$ a relative change in optical density of 2 and a 1/e response time of less than 5 milliseconds were achieved using f/5 focusing optics. This result represents a steady state optical limiting transmission of 20 times less than the bulk material and a 60 times faster photorefractive response time. While the input intensity required to achieve this result was higher than expected from the bulk material, possible degradation mechanisms such as non-optimum focussing conditions and localised changes in material composition during the direct bonding process were explored, explained in terms of performance loss, and expanded for improvement. Overall, the buried planar waveguide structure allows access to wide aperture imaging systems for high-speed optical limiting applications, and future devices based on this technology are likely to incorporate multiple-layers and linear arrays of titanium indiffused channel waveguides.

## REFERENCES:

[1] A. M. Glass, "*The photorefractive effect*", Optical Engineering, Vol. 17, No. 5, p.470-479 (1978).

[2] A. Ashkin, G. D. Boyd, J. M. Dziedzic, R. G. Smith, A. A. Ballman, J. J. Levinstein, and K. Nassau, "*Optically-induced refractive index inhomogeneities in $LiNbO_3$ and $LiTaO_3$*", Applied Physics Letters, Vol. 9, No. 1, p.72-74 (1966).

[3] F. S. Chen, J. T. LaMacchia, and D. B. Fraser, "*Holographic storage in lithium niobate*", Applied Physics Letters, Vol. 13, No. 7, p.223-225 (1968).

[4] D. L. Staebler and J. J. Amodei, "*Coupled-wave analysis of holographic storage in $LiNbO_3$*", Journal of Applied Physics, Vol. 43, No. 3, p.1042-1049 (1972).

[5] A. M. Glass, D. von der Linde, and T. J. Negran, "*High-voltage bulk photovoltaic effect and the photorefractive process in $LiNbO_3$*", Applied Physics Letters, Vol. 25, No. 4, p.233-235 (1974).

[6] N. V. Kukhtarev, V. B. Markov, S. G. Odulov, M. S. Soskin, and V. L. Vinetskii, "*Holographic storage in electrooptic crystals. I. Steady state*", Ferroelectrics, Vol. 22, p.949-960 (1979).

[7] N. V. Kukhtarev, V. B. Markov, S. G. Odulov, M. S. Soskin, and V. L. Vinetskii, "*Holographic storage in electrooptic crystals. II.Beam coupling – light amplification*", Ferroelectrics, Vol. 22, p.949-960 (1979).

[8] D. L. Staebler and J. J. Amodei, "*Thermally fixed holograms in $LiNbO_3$*", Ferroelectrics, Vol. 3, p.107-113 (1972).

[9] D. W. Vahey, "*A nonlinear coupled-wave theory of holographic storage in ferroelectric materials*", Journal of Applied Physics, Vol. 46, No. 8, p.3510-3515 (1975).

[10] G. C. Valley and M. B. Klein, "*Optimal properties of photorefractive materials for optical data processing*", Optical Engineering, Vol. 22, No. 6, p.704-711 (1983).

[11] G. A. Rakuljic, V. Leyva, and A. Yariv, "*Optical data storage by using orthogonal wavelength-multiplexed volume holograms*", Optics Letters, Vol. 17, No. 20, p.1471-1473 (1992).

[12] P. Yeh, "*Two-wave mixing in nonlinear media*", IEEE Journal of Quantum Electronics, Vol. 25, No. 3, p.484-519 (1989).

[13] M. Cronin-Golomb, B. Fischer, J. O. White, and A. Yariv, "*Theory and applications of four-wave mixing in photorefractive media*", IEEE Journal of Quantum Electronics, Vol. QE-20, No. 1, p.12-30 (1984).

[14] P. Yeh, "*Contra-directional two-wave mixing in photorefractive media*", Optics Communications, Vol. 45, No. 5, p.323-326 (1983).

[15] K. R. MacDonald, J. Feinberg, M. Z. Zha, and P. Günter, "*Asymmetric transmission through a photorefractive crystal of barium titanate*", Optics Communications, Vol. 50, No. 3, p.146-150 (1984).

[16] M. Z. Zha, and P. Günter, "*Nonreciprocal optical transmission through photorefractive $KnbO_3$:Mn*", Optics Letters, Vol. 10, No. 4, p.184-186 (1985).

[17] A. Krummins, Z. Chen, and T. Shiosaki, "*Photorefractive reflection gratings and coupling gain in $LiNbO_3$:Fe*", Optics Communications, Vol. 117, p.147-150 (1995).

[18] R. Crane, K. Lewis, E. V. Stryland, and M. Khoshnevisan, "*Materials for optical limiting*", Materials Research Society Symposium Proceedings, Vol. 374 (1995).

[19] R. Sutherland, R. Patcher, P. Hood, D. Hagan, K. Lewis, and J. Perry, "*Materials for optical limiting II*", Materials Research Society Symposium Proceedings, Vol. 479 (1997).

[20] G. Cook, D. C. Jones, C. J. Finnan, L. L. Taylor, and T. W. Vere, "*Optical limiting with lithium niobate*", SPIE, Vol. 3798, p.2-16 (1999).

[21] G. Cook, C. J. Finnan, and D. C. Jones, "*High optical gain using counterpropagating beams in iron and terbium-doped photorefractive lithium niobate*", Applied Physics B, Vol. 68, p.911-916 (1999).

[22] G. Cook, J. P. Duignan, L. L. Taylor, and D. C. Jones, "*Developing photorefractive fibres for optical limiting*", SPIE, Vol. 4106, p.230-244 (1999).

[23] D. C. Jones and G. Cook, "*Non-reciprocal transmission through photorefractive crystals in the transient regime using reflection geometry*", Optics Communications, Vol. 180, p.391-402 (2000).

[24] J. Haisma, G. A. C. M. Spierings, U. K. P. Biermann, and A. A. van Gorkum, "*Diversity and feasibility of direct bonding: a survey of a dedicated optical technology*", Applied Optics, Vol. 33, No. 7, p.1154-1169 (1994).

[25] A. Plößl and G. Kräuter, "*Wafer direct bonding: tailoring adhesion between brittle materials*", Materials Science and Engineering, Vol. R25, No. 1-2, p.1-88 (1999).

[26] A. Yariv, "*Quantum electronics*" 3rd Edition, John Wiley and Sons (1989).

[27] M. D. Ewbank, R. R. Neurgaonkar, and W. K. Cory, "*Photorefractive properties of strontium-barium niobate*", Journal of Applied Physics, Vol. 62, No. 2, p.374-380 (1987).

[28] M. B. Klein and R. N. Schwartz, "*Photorefractive effect in $BaTiO_3$*", Journal of the Optical Society of America B, Vol. 3, p.293-305 (1986).

[29] S. Ducherme, J. C. Scott, R. J. Twieg, and W. E. Moerner, "*Observation of the photorefractive effect in a polymer*", Physical Review Letters, Vol. 66, No. 14, p.1846-1849 (1991).

[30] D. L. Staebler and W. Phillips, "*Fe-doped $LiNbO_3$ for read-write applications*", Applied Optics, Vol. 13, No. 4, p.788-794 (1974).

[31] K. Chah, M. Aillerie, M. D. Fontana, and G. Malovichko, "*Electro-optic properties in Fe:doped $LiNbO_3$ crystals as a function of composition*", Optics Communications, Vol. 176, p.261-265 (2000).

[32] J. Wilson and J. F. B. Hawkes, "*Optoelectronics an introduction*" 2nd Edition, Prentice Hall (1989).

[33] E. E. Robertson, "*Manipulation of the photorefractive properties of ferroelectric waveguides by ion-beam implantation*", University of Southampton, Thesis (1997).

[34] G. Cook, D. C. Jones, and J. P. Duignan, "*Influence of the photovoltaic effect on optical limiting with lithium niobate*", SPIE 2000 paper no. 4106C-37 (2000).

[35] T. Volk, N. Rubinina, and M. Wohlkecke, "*Optical-damage-resistant impurities in lithium-niobate*", Journal of the Optical Society of America B, Vol. 11, No. 9, p.1681-1687 (1994).

[36] A. V. Petrov, S. Yin, F.T.S. Yu, O. B. Leonov, Y. Suzuki, and K. Shinoda, "*Fabrication of $LiNbO_3$ single crystal fiber array for wideband antenna signal processing*", Proceedings of the SPIE, Vol. 3137, p.183-188 (1997).

[37] I. E. Barry, R. W. Eason, and G. Cook, "*Light-induced frustrated etching in Fe-doped $LiNbO_3$*", Applied Surface Science, Vol. 143, p.328-331 (1999).

[38] I. E. Barry, G. W. Ross, P. G. R. Smith, R. W. Eason, and G. Cook, "*Microstructuring of lithium niobate using differential etch rate between inverted and non-inverted ferroelectric domains*", Materials Letters, Vol. 37, No. 4-5, p.246-254 (1998).

[39] T. Fujiwara, R. Srivastava, X. Cao, and R. V. Ramaswamy, "*Comparison of photorefractive index change in proton-exchanged and Ti-indiffused $LiNbO_3$ waveguides*", Optics Letters, Vol. 18, No. 5, p.346-348 (1993).

[40] C. B. E. Gawith, D. P. Shepherd, J. A. Abernethy, D. C. Hanna, G. W. Ross, and P. G. R. Smith, "*Second-harmonic generation in a direct-bonded periodically poled $LiNbO_3$ buried waveguide*", Optics Letters, Vol. 24, No. 7, p.481-483 (1999).

[41] K. Eda, M. Sugimoto, and Y. Tomita, "*Direct heterobonding of lithium niobate onto lithium tantalate*", Applied Physics Letters, Vol. 66, No. 7, p.827-829 (1995).

[42] J. Noda, M. Fukuma, and S. Saito, "*Effect of Mg diffusion on Ti-diffused $LiNbO_3$ waveguides*", Journal of Applied Physics, Vol. 49, No. 6, p.3150-3154 (1978).

[43] Y. Tomita, M. Sugimoto, and K. Eda, "*Direct bonding of $LiNbO_3$ single crystals for optical waveguides*", Applied Physics Letters, Vol. 66, No. 12, p.1484-1485 (1995).

[44] J. Haisma, G. A. C. M. Spierings, T. L. Michielsen, and C. L. Adema, "*Surface preparation and phenomenological aspects of direct bonding*", Philips Journal of Research, Vol. 49, p.23-46 (1995).

[45] C. Yang, Y. Zhao, R. Wang, and M. Li, "*Studies of photorefractive crystals of double-doped Ce,Fe:$LiNbO_3$*", Optics Communications, Vol. 175, p.247-252 (2000).

[46] C. B. E. Gawith, T. Bhutta, D. P. Shepherd, P. Hua, J. Wang, G. W. Ross, and P. G. R. Smith, "*Buried laser waveguides in neodymium-doped BK-7 by $K^+$-$Na^+$ ion-exchange across a direct-bonded interface*", Applied Physics Letters, Vol. 75, No. 24, p.3757-3759 (1999).

# Chapter 5
# BURIED LASER WAVEGUIDES BY INTERSUBSTRATE ION-EXCHANGE ACROSS A DIRECT-BONDED INTERFACE

## 5.1 Introduction

Since the first ion-exchanged waveguides were reported by Izawa and Nakagome in 1972 [1], the technique of exchanging alkali ions between a substrate material and molten salt bath has become a staple part of the optoelectronics industry [2-6]. A fundamental stage in the development of optical planar waveguide devices in glass, these early experiments facilitated optical confinement by the electric-field induced migration of thallium into the surface of a borosilicate substrate, replacing some of the alkaline ions in the glass and raising the refractive index [1]. The next year, Giallorenzi et al. [3] demonstrated both surface and buried waveguides by a simpler thermal diffusion technique, eliminating the need for an applied electric-field and instigating the investigation of a diverse range of exchanging ions and host substrates [4-9]. Since that time, ion-exchange has been used as the basis for a diverse range of optical-fiber-compatible planar waveguide devices in glass, from passive waveguide structures [10] and on towards active laser and amplifier devices [11-12]. However, while significant progress has been made towards understanding the underlying mechanics of ion-exchange [13-14], and the effects of processing conditions on waveguide characteristics [15-16], the problems of choice and synthesis of suitable host materials have still not been fully satisfied [6] and the contemporary methods used to create ion-exchanged waveguides remain almost the same as those used thirty years ago...

The origin of the intersubstrate ion-exchange technique introduced in this chapter remained a mystery for over a year. Initially designed as a feasibility study for glass-based direct bonding projects, the combination of a neodymium-doped BK-7 layer and undoped BK-7 cladding substrate was originally intended to form a simple two-layer bonded structure for basic waveguide investigation. However, when a single-mode planar waveguide layer was accidentally discovered buried 50 μm below the top surface of the rare-earth-doped substrate, coinciding with the direct-bonded interface of the sample, the obvious question to ask was *how* did it actually get there?

With various theories ranging from a local bonding-stress-induced change in refractive index, to surface modification of the glass substrates during sample polishing, it was only after extensive material analysis of the bulk glasses and direct-bonded samples that an internal ion-exchange mechanism occurring directly between the two glass layers was discovered and developed for use as a single-step solid-state solution for creating buried planar waveguide laser devices in glass.

In this chapter, the principles behind alkali ion-exchange and its role in the production of waveguiding structures are described. Discussed are the issues of loss reduction in ion-exchanged devices, sources of exchanging ions, factors concerning the choice of a host glass, and the current state of technology. The concept of modifying glass for use as a solid-state source for ion-exchange is introduced, with the aim of creating novel waveguiding structures in adjoining substrates. Direct bonding is applied as the means of atomic contact between ion-exchanging substrates and provides a heat treatment suitable for simultaneous annealing and diffusion between two glass layers. Finally, the characteristics of buried waveguide devices produced in neodymium-doped BK-7 by a novel intersubstrate ion-exchange technique are presented.

## 5.2 Refractive index change due to alkali ion-exchange

The refractive index of a multicomponent glass is dependent on the type and concentration of the different alkali ions in its chemical composition [17]. Changing one type of alkali ion for another will perturb the refractive index, an effect that can be used to fabricate waveguiding structures in silicate glass substrates [4-6]. In this ion-exchange process, both cations for substitution are glass network modifiers while the oxygen anions remain fixed in the silicon-oxygen network [17]. This leaves the basic structure of the glass unchanged whilst modifying the refractive index. The net index variation achieved is dependent on three major changes in the glass; ionic polarisability, molar volume, and stresses caused by the substitution [5,18]. An estimation of the refractive index change due to ion-exchange can be performed using a model derived from the Gladstone-Dale equation by Huggins and Sun, as outlined in Reference [5]. By relating the density, refractive index, and dispersion of a glass to the weight percentage of oxide constituents in its composition, this model predicts that the change in refractive index is given by [5]:

$$\Delta n = \frac{\chi}{V_o}\left(\Delta R - R_o \frac{\Delta V}{V_o}\right) \tag{5.1}$$

where $\chi$ is the percentage of cations exchanged for incoming ions, $V_o$ is the volume per mole of oxygen atoms, $R_o$ is the refraction per mole of oxygen atoms, and $\Delta R$ and $\Delta V$ are the changes in these quantities resulting from ion-exchange. In this simple model, the change in refractive index is dependent on two of the major glass altering effects caused by ion-exchange. The first term arises from the difference in ionic polarisability of the two cations and indicates that substituting one ion for another with a higher polarisability will cause an increase in refractive index. This effect dominates the raise in index achieved when silver, thallium, and caesium ions replace sodium in a glass [4]. The second term in Equation 5.1 represents the contribution of changes in molar volume to the refractive index of the glass. When an ion of smaller volume replaces a larger one, the glass matrix contracts and the total polarisability per unit volume increases. This effect explains the increase in refractive index obtained when lithium ions replace sodium in a glass [4].

When Equation 5.1 is used to model the refractive index change caused by exchanging potassium ions for sodium ions the result is two orders of magnitude smaller than that measured by practical means [5]. This is because the model neglects the third major affect of ion-exchange upon refractive index: stress [18]. Ion-exchange involves substituting two ions of different size at temperatures well below the glass annealing temperature. In the case of $K^+$-$Na^+$ ion-exchange the exchanging ion is larger than its predecessor, causing the surface of the substrate to swell. This effect creates compressive stresses in the ion-exchanged region of the glass, which are balanced by tensile stresses in the substrate. The result is an increase in refractive index for the compressive layer and a decrease in the index of the tensile region [17].

To date, a wide variety of glasses and alkali ions have been characterised for use in ion-exchange processes, the majority of which were reviewed by Nikonorov and Petrovskii in 1999 [6]. Table 5.1 features the properties of commonly used alkali ions for ion-exchange, which include; sodium, potassium, silver, thallium, lithium, caesium, and rubidium. The typical characteristics exhibited by each pair of exchanging ions are also presented, as all have different qualities when used in the

fabrication of a waveguide device [4-6]. Silver and thallium cause a large change in refractive index and can be used to create low-loss multimode waveguides in a relatively short time. However, thallium is toxic and silver ions can reduce to atomic form within the glass to cause additional impurities and scattering losses. Caesium ions have low mobility in glass and require field-assisted processes to reduce exchange time. Caesium is also highly reactive and requires resistant containers to handle the molten salt. Lithium ions are highly mobile in glasses, allowing multimode waveguides to be fabricated quickly, although volumetric changes in the glass structure can cause it to collapse. Potassium ions exchange easily with sodium ions to produce small changes in refractive index, a process mainly used for the production of single-mode waveguides. Such waveguides can feature very low losses if an appropriate host glass is chosen, but require relatively long processing times.

| Ion | Polarisability ($Å^3$) | Ionic radius (Å) | Salt | Melting point (°C) | Δn | Waveguide depth (μm) | Losses (dB $cm^{-1}$) |
|---|---|---|---|---|---|---|---|
| $Na^+$ | 0.41 | 0.95 | $NaNO_3$ | 307 | - | - | - |
| $K^+$ | 1.33 | 1.33 | $KNO_3$ | 334 | 0.009 | 15-20 | < 0.1 |
| $Ag^+$ | 2.40 | 1.26 | $AgNO_3$ | 212 | 0.1 | 50 | <0.2 |
| $Tl^+$ | 5.20 | 1.49 | $TlNO_3$ | 206 | 0.2 | 12 | <0.1 |
| $Li^+$ | 0.03 | 0.65 | $LiNO_3$ | 264 | 0.012 | 10-70 | 1 |
| $Cs^+$ | 3.34 | 1.65 | $CsNO_3$ | 414 | 0.04 | 8 | 0.2 |
| $Rb^+$ | 1.98 | 1.49 | $RbNO_3$ | 310 | 0.02 | 15 | 0.1 |

**Table 5.1**: General characteristics of alkali ions and their corresponding waveguides after ion-exchange into sodium-doped silicate glasses. Data compiled from References [5-6] where the values for losses are not presented for a particular wavelength.

## 5.3 Sources of exchanging ions

Actively studied and reviewed [4-6] for many years, the ion-exchange process remains almost exclusively based upon the use of a molten salt bath as a source of alkali ions for diffusion. Nitrates of the exchanging ions are most commonly used for this process as their low melting temperatures allow ion-exchange to be performed in readily available substrate materials such as sodalime and borosilicate glasses. Suitably masked to define waveguiding regions on the substrate, the glass is immersed in the nitrate melt for a time and temperature dependent on required waveguide characteristics such as diffusion depth and the number of modes. Though the rate of diffusion is increased with temperature, allowing shorter processing times, the molten salt will become increasingly aggressive towards the glass substrate as the

temperature of the melt is raised. As such, lower ion-exchange temperatures are preferred, with the applied temperature never exceeding the glass transition temperature lest glass modification occur [17].

Deposition of a thin metal film onto a glass substrate provides a solid-state source for ion-exchange processes. Since no alkali metal can be deposited and maintained in a stable form [19], this technique is mainly used for the fabrication of silver-based waveguides [20-21] although other metals such as copper [9], gold, and thallium have also generated interest [6]. Ion-exchange between the substrate glass and metallic layer is generally achieved at an elevated temperature, with the metal film often applied as an anode for use in field-assisted diffusion. The main difference between this and the case of molten salts is that the ions are introduced into the glass by an electrochemical reaction in which silver oxidises and no appreciable thermal diffusion from the metal film occurs [21].

As an alternative to these methods, the results presented in this chapter are based on a previously unexplored solid-state source of exchanging ions for optical confinement in glass, namely: glass. The premise behind this technique is the creation of two complementary glass substrates that, once contacted, feature the opposing chemical gradients of alkali ions necessary for ion-exchange to take place. As an example, $K^+$-$Na^+$ ion-exchange has been achieved by doping one glass layer with more potassium and less sodium than its counterpart, encouraging intersubstrate diffusion of the two ionic species. After a suitable heat treatment, this process results in a region of raised refractive index near the edge of the sodium rich substrate, where potassium has been introduced. As with other ion-exchange methods, careful consideration of the time, temperature and starting materials involved in this process is a necessary part of waveguide design. In particular, it should be noted that if the glass layers are to be permanently joined, as per the direct bonding [22,23] technique, then the refractive index of each layer must be carefully balanced such that the exchange of ions will create one region of raised refractive index suitable for waveguiding (Figure 5.1). This can be simply achieved by ensuring that the substrate into which index-raising ions will be diffused begins with an equal or higher refractive index than that of the second glass.

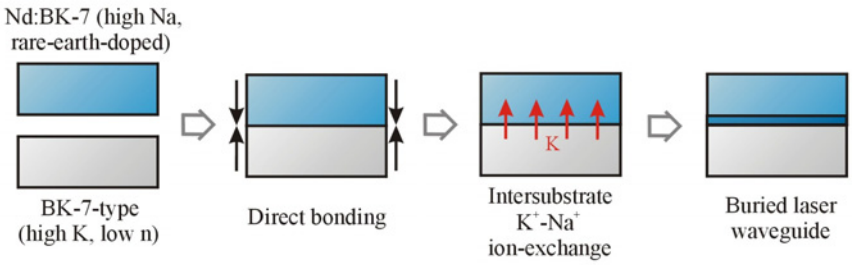


**Figure 5.1:** Key stages in the design and fabrication of an intersubstrate ion-exchanged planar laser waveguide device.

The benefits of creating a device by the combination of intersubstrate diffusion and direct bonding techniques are threefold. Firstly, direct bonding provides a region of atomic contact between the two glass layers across which ion-exchange can occur uniformly. This allows large waveguiding regions to be processed, limited only by the areas across which direct bonding will perform successfully. The second and third benefits of this amalgamation both arise from the heat treatment used in direct bonding to anneal the sample interface. As stated earlier, ion-exchange must be performed below the glass transition temperature otherwise glass modification will occur. This is also true for the annealing of direct-bonded glasses, with relatively low temperatures providing ample strength for further machining. Therefore, if a suitable temperature is chosen, both of these processes can be performed simultaneously, resulting in single step waveguide fabrication. This is the most beneficial result of this combined process, as the two glass substrates will be in permanent contact both during and after ion-exchange, resulting in a buried waveguide structure.

## 5.4 Buried ion-exchanged waveguides

The production of efficient integrated optics devices in glass requires that the losses associated with surface waveguides must be minimised. Such problems are due to light scattering from imperfections at the waveguide-air interface, causing propagating fields to have increased loss and asymmetric mode profiles that can prove inefficient for coupling into optical fibres [3-6]. Overcoming these losses is an active area of study, leading researchers to investigate novel ways of burying waveguides below the surface of an ion-exchanged substrate [16,24].

Fabrication of a buried waveguide by ion-exchange is generally achieved in two stages, beginning with a standard ion-exchange process into a substrate material. The

region of exchanged ions is then diffused further into the substrate with a secondary heat or electric field treatment [3,16], or by means of a second ion-exchange process designed to lower the refractive index of the substrate at the surface [6]. The improved symmetry offered by these waveguides reduces insertion losses into optical fibres, while the buried structure avoids surface related problems entirely. However, care must be taken to account for the further diffusion of ions in the material, especially in the case of purely thermal two-step ion-exchange processes, as this can alter the waveguide depth and refractive index profile. Alternatives to these techniques are few, but include a more recently applied method of direct bonding a second layer onto an ion-exchanged substrate, burying the waveguide completely [24].

As mentioned in Section 5.3, direct bonding can be combined with the glasses designed for intersubstrate ion-exchange to produce a buried waveguide. This technique has been successfully implemented for the fabrication of waveguides in neodymium doped BK-7, with $K^+$-$Na^+$ ion-exchange forming the basis of waveguide creation. Substrates of neodymium-doped BK-7 and BK-7-type glass (see the next section), which feature the opposing chemical gradients of potassium and sodium necessary for $K^+$-$Na^+$ ion-exchange, are joined across a low-loss, atomically smooth interface by direct bonding. In direct contrast to the two-step method employed by Pelissiér et al. [24], which involves writing waveguides into borosilicate glass by ion-exchange and then burying them with direct bonding techniques, the heat treatment used for intersubstrate ion-exchange is only applied once the two substrate layers are contacted. By taking this approach, a single-step buried ion-exchange mechanism with intrinsically low waveguide losses is achieved. It is the annealing phase used in direct bonding that provides the key to this process, as the time and temperature used to strengthen direct bonded BK-7 substrates (between 350 °C and 400 °C for several hours) is also appropriate for $K^+$-$Na^+$ ion-exchange [7]. Performing these processes simultaneously removes any risk of secondary diffusion of the waveguide layer, or damage to the optically polished substrates prior to bonding, reducing the potential for waveguide degradation. An additional benefit of this technique is that the entire process is performed in a dedicated clean area, from sample cleaning to direct

bonding and ion-exchange, removing the glasses from the hostile environment associated with a molten salt bath.

## 5.5 Glasses for ion-exchange

The losses inherent within an ion-exchanged waveguide can be minimised by careful choice of the host glass [6]. Although any glass containing monovalent ions is a potential candidate for ion-exchange, absorption due to impurities in the glass, combined with scattering losses from inhomogenities and surface defects, can drastically affect waveguide characteristics. The ability of the glass to withstand ion-exchange temperatures, without undergoing structural changes, is another factor that must be considered prior to fabrication.

The most common substrate for use in ion-exchange experiments remains sodalime glass due to its sodium-rich content, low cost, and ready availability [6]. However, waveguides produced in this material tend to be lossy, an effect largely due to metallic impurities and variations in material composition [5]. As such, commercially available optical quality glasses such as BK-7, which features excellent transmissive properties in the visible and near infra-red [6], have received much attention for use in integrated-optics applications with waveguide losses as low as 0.1 dB $cm^{-1}$ having been reported in such substrates [6,25]. Although a wide variety of glasses are available for ion-exchange, around ninety percent of ion-exchange processes are performed in just three glass types [6]; BK-7 from Schott, 0211 from Corning, and K8 (a Russian glass of comparable composition and optical properties to BK-7) from the Vavilov State Optical Institute.

The devices introduced in this chapter were produced from glass substrates with similar compositions to that of commercially available BK-7 from Schott [25]. An active glass layer, chosen due to its suitability for laser action and raised refractive index, was fabricated by introducing rare-earth ions into commercially available BK-7 by a process developed by Ji Wang and Eustace Mwarania at Southampton University [11,12,19]. Preparation of the rare-earth-doped substrate began by mixing pieces of commercially available BK-7 glass with 2 wt.% of neodymium oxide in a ceramic crucible. This mixture was placed in an electrically heated furnace and stirred

to promote uniformity of neodymium ions within the host material. A temperature range of 850 °C to 1450 °C was available throughout the doping process, the melt being fined at 1400 °C and removed from the furnace at 1300 °C. Cast into a stainless steel mould, the melt was finally annealed in a muffle furnace at 580 °C. Further details of this technique can be found in Reference [19].

The second glass type, which forms the cladding layer of the device and acts as a source of potassium for ion-exchange, was prepared from basic oxide materials by a similar technique. Based on the chemical composition of commercially available BK-7, this oxide mix features approximately 4 wt.% of additional $K_2O$ in the glass, for which an equal amount of $Na_2O$ was removed. Such an offset in glass composition between our BK-7-type and neodymium-doped substrates, the latter of which features around 6 wt.% of both $K_2O$ and $Na_2O$ (this is slightly lower than normal due to the doping process), allows the realisation of buried laser waveguides by internal ion-exchange processes in direct bonded structures. Multiple samples have been produced by this method, all of which feature a single mode waveguide at the neodymium-doped edge of the bonded interface, proving that this is a robust technique for waveguide creation. It should be noted however, that these glasses have not yet been optimised for intersubstrate ion-exchange. In particular, the neodymium-doped glass provided for these experiments features visible inhomogeneties and variations in concentration, aberrations that will inevitably affect laser performance, although subsequent results prove sufficient for this initial demonstration of principal.

| Glass | Composition (weight %) | | | | | |
|---|---|---|---|---|---|---|
| | $SiO_2$ | $B_2O_3$ | $Na_2O$ | $K_2O$ | $Ba_2O$ | Trace |
| BK-7 | 69.6 | 9.9 | 8.4 | 8.4 | 2.5 | 1.2 |

**Table 5.2**: Composition of commercially available BK-7 glass from Schott [29].

The chemical composition of commercially available BK-7 is given in Table 5.2 and the refractive index of the bulk glass is 1.5168. Refractive indices of the neodymium-doped BK-7 and BK-7-type substrates used in this experiment were measured using an Abbe refractometer [26] at a wavelength of 587 nm, and were recorded as 1.5147

and 1.5105 respectively. These values are lower than expected and probably result from the compositional problems faced during the fabrication of the glass.

## 5.6 Intersubstrate ion-exchanged buried laser waveguides

From the neodymium-doped BK-7 glass, a 2-mm-thick substrate, of 10 mm × 5 mm surface area, was diced and polished to provide an optically flat surface suitable for direct bonding. A similar substrate was prepared from the BK-7-type material. After cleaning, a mixture of $H_2O_2$-$NH_4OH$-$H_2O$ (1:1:6), followed by several minutes of rinsing in deionised water, was applied to both materials in order to render their surfaces hydrophilic [27]. The doped and undoped layers were then brought into contact at room temperature and finger pressure applied in order to promote adhesive avalanche [28]. This effect forced any excess air or liquid from between the two substrates, as demonstrated by the removal of all interference fringes across the 10 mm × 5 mm bonded interface. Annealing of the sample at 350 °C for 6 hours provided ample bond strength for further machining and sufficient ion-exchange to create a single-mode waveguide on the neodymium-doped side of the bonded interface. The sample was then diced and polished to a final length of 5.8 mm. Dimensions of the resulting buried laser waveguide device are given in Figure 5.2.

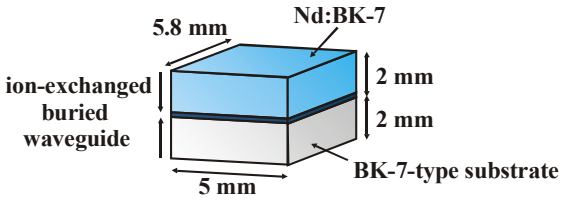


**Figure 5.2**: Schematic end-face diagram of a buried laser waveguide device fabricated by intersubstrate ion-exchange.

Images of the polished end face of the device, obtained by scanning electron microscopy, show no gaps in the bonded interface at 250× magnification, although the two material layers are easily distinguished (Figure 5.3a). Increasing the magnification to ×2500 also shows no gaps along the bond (Figure 5.3b), although the interface becomes less recognisable at higher resolutions. The spots evident in Figure 5.3b are the result of several point compositional analyses performed by the scanning electron microscope (SEM), a technique introduced in the next section, and the large dark area is simply dirt on the end face of the sample.

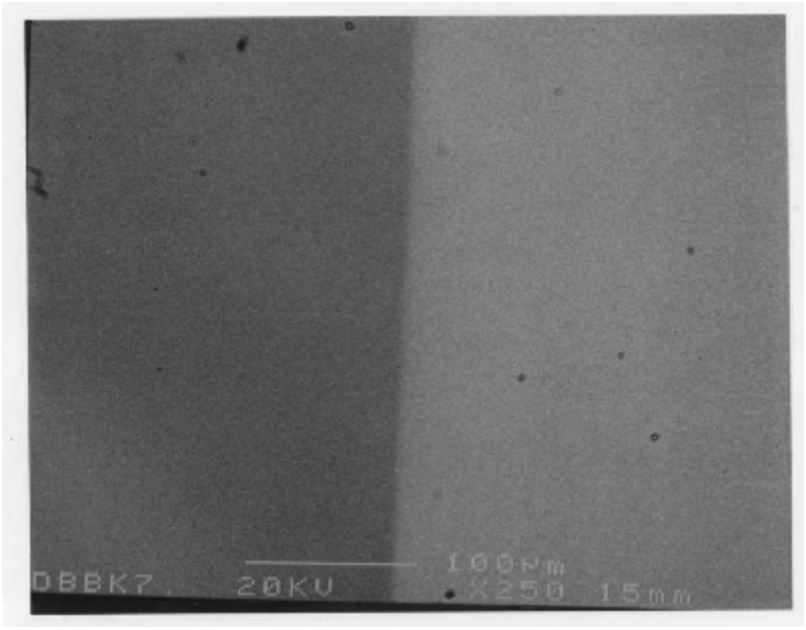


(a)

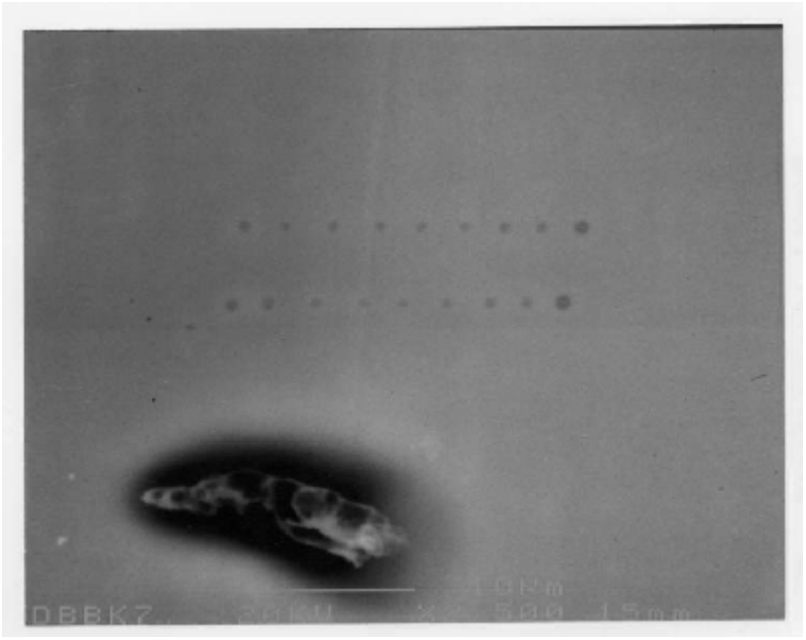


(b)

**Figure 5.3**: Images of a direct-bonded interface between neodymium-doped BK-7 (the darker region to the left of the picture) and BK-7-type glass layers. Image (a) was taken using scanning electron microscopy at 250× magnification and image (b) was taken at 2500× magnification.

## 5.7 Compositional analysis

The discovery of a buried waveguide near the bonded interface of each sample prompted several tests to confirm the origin as an internal ion-exchange mechanism. Optical testing produced no evidence of waveguiding as a result of any pre-annealing processing step (from polishing and cleaning to the direct bonding of the two layers), although every annealed sample exhibited a buried waveguide. This result indicates

that the direct bonding heat treatment was directly responsible for the creation of optical confinement within the devices.

Confirmation of the ion-exchange process within these direct bonded samples was provided by a scanning electron microscope based compositional line profile analysis. This technique was used to measure the difference in relative concentration for potassium and sodium across the polished end-faces of an annealed device and an unannealed control sample, the results of which are given in Figure 5.4. As illustrated by the graph, there is a significant ionic redistribution between the line profiles of the unannealed (broken line) and annealed (solid line) samples, wherein $K^+$ and $Na^+$ ions have inter-diffused across the bonded interface. This heat-related change in chemical composition provides proof of an internal ion-exchange mechanism within our devices, the result of which is a single-step buried waveguide of around 10-μm-deep.

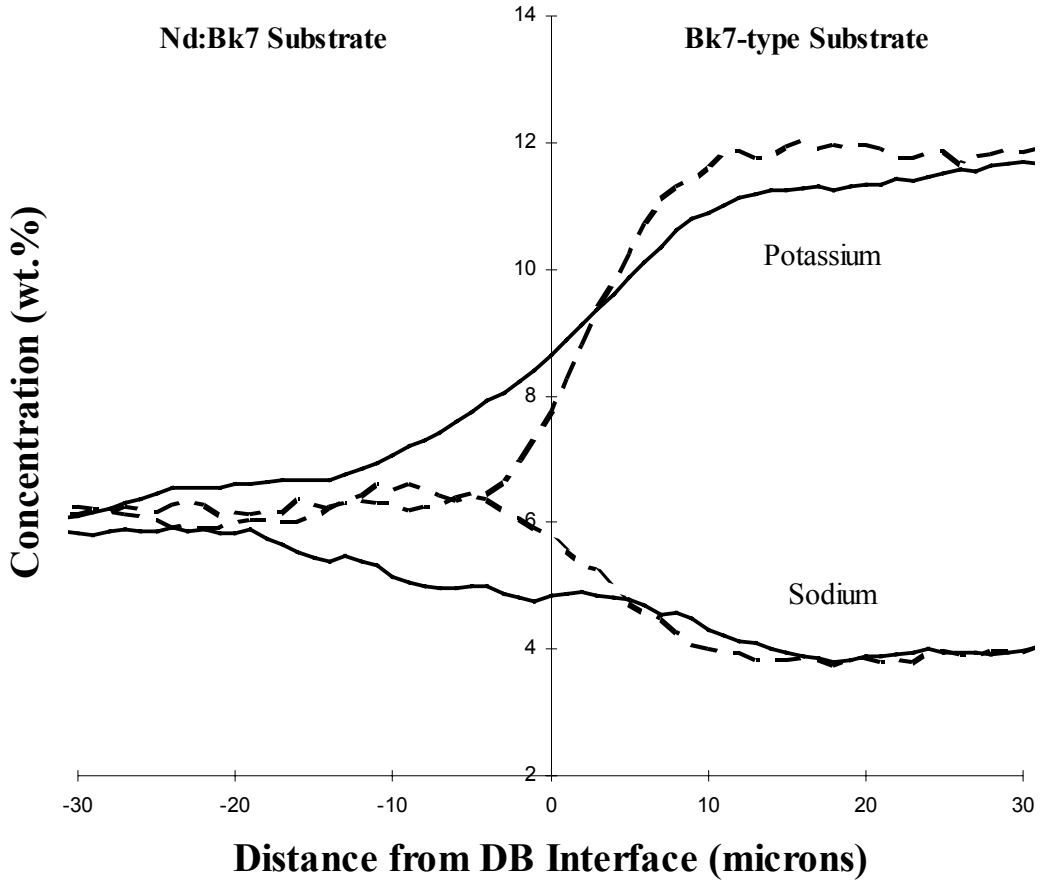


**Figure 5.4**: A graph of chemical composition versus distance across the interface of an annealed device (solid line) and an unannealed control sample (broken line). The change in chemical profile with annealing indicates $K^+$-$Na^+$ ion-exchange between the two glass substrates.

Unfortunately, the low resolution offered by the SEM requires that a mathematical deconvolution be performed in order to isolate the overall changes in ionic distribution from our results [Appendix A]. This is most evident for the case of the unannealed sample, where step functions of sodium and potassium concentration were expected across the sample interface but a curved measurement of composition was recorded, and is caused by the profiling technique chosen. For compositional analysis, a scanning electron microscope works by focussing a high-energy beam of electrons onto the polished surface of a sample and analysing the characteristics of backscattered electrons [29]. The resolution of this process is directly related to the size of the probing beam used and tends to be material specific. Scattering efficiencies of different ions determine the sensitivity of the measurement, with ions of larger atomic masses scattering more efficiently than smaller ones. Concentration profiles for heavy ions, such as; potassium, silver, and thallium, will therefore be more accurate than those for lighter ions; sodium and lithium for example. To measure the relative changes in chemical composition across the glass-based direct-bonded devices, it was necessary to use a probe beam of approximately 5 μm interaction diameter. Considering that the total range of inter-substrate diffusion was around 40 μm, with the majority of activity occurring within 10 μm either side of the device interface, this resolution is simply too low to gain an accurate description of the chemical changes in the sample. As such our future plans for diffusion modelling include a more accurate secondary ion mass spectroscopy (SIMS) compositional analysis [25] combined with further studies into the effects of annealing time and temperature on waveguide parameters.

## 5.8 Waveguide characteristics

Characterisation of spectroscopy, laser performance, and propagation loss of the buried laser waveguide device was performed with a tuneable (700 nm to 850 nm) Ti-Sapphire laser, as illustrated in Figure 5.5. Pump radiation was focussed for launch into the waveguide by means of a ×10 microscope objective, to a measured input spot size of approximately 3 μm. Optimisation of the launch was performed in relation to the fluorescence measured by a silicon detector and maximum absorption was found to occur at 808 nm in the neodymium-doped substrate layer by careful tuning of the pump wavelength. The absorption efficiency of the neodymium-doped glass was

calculated from relative measurements of input and output pump power from the doped and undoped regions of the device (measured at an pump wavelength of 808 nm), giving a value of 68 %. A launch efficiency of 76 % was calculated from similar transmission measurements taken from the bulk and buried waveguide regions of the neodymium-doped substrate. Fluorescence spectra (Figure 5.6) from the waveguide and bulk neodymium-doped BK-7 regions of the device were measured using a triple grating spectrograph and were typical of similarly produced glass [12]. The fluorescence lifetime of the rare-earth doped waveguide was measured by placing an optical chopper before the input objective and measuring the output fluorescence with a silicon detector and digital oscilloscope. The recorded value of 470 μs (Figure 5.7) is also typical of neodymium-doped borosilicate glass [12].

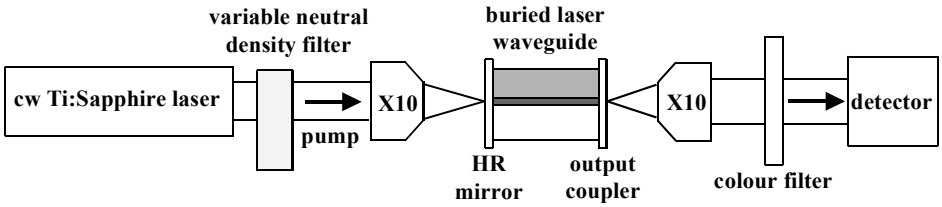


**Figure 5.5**: Typical arrangement for laser characterisation of the buried waveguide (although during launch absorption measurements no mirrors were applied to the ends of the device). A pump wavelength of 808 nm was used to obtain a 1059 nm laser output from our device.

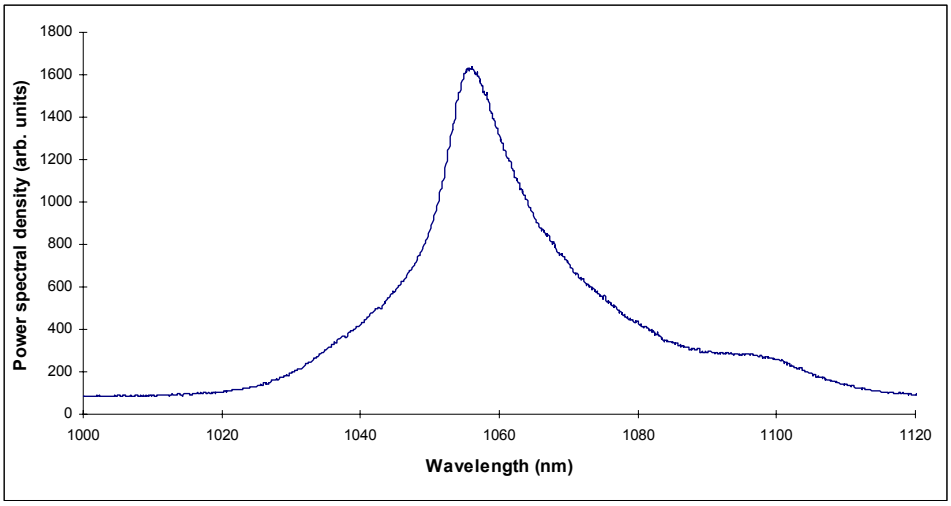


**Figure 5.6**: A graph showing the fluorescence spectra characteristics of neodymium ions in a buried laser waveguide device, as measured with a triple grating spectrograph.

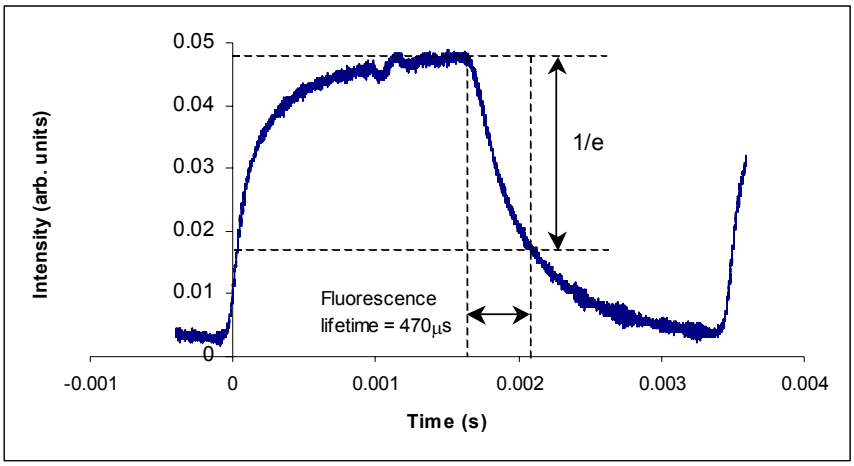


**Figure 5.7:** Fluorescence lifetime of neodymium ions in a buried laser waveguide device, as measured with a silicon detector and digital oscilloscope.

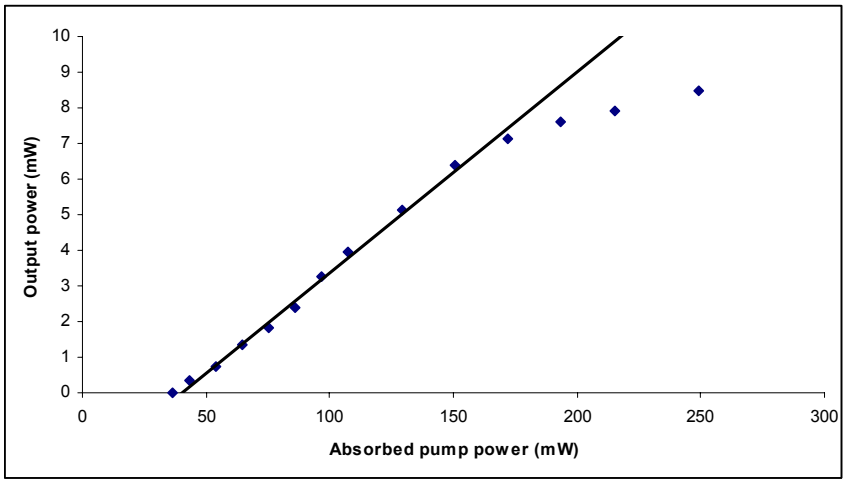


**Figure 5.8**: A graph of output power versus absorbed pump power for a buried laser waveguide device. The straight line of best fit defines a slope efficiency of 6 % for the device, while the fall off of the curve at higher absorbed powers could indicate an effect such as thermal lensing, although this has not been investigated within the scope of this project.

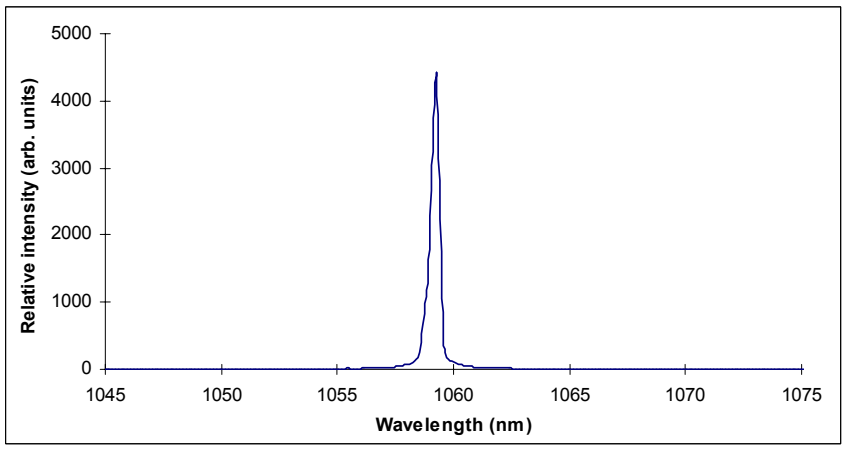


**Figure 5.9**: A graph of wavelength versus intensity for the output of the buried laser waveguide device. This measurement was taken using 615 mW of pump power from an 808 nm wavelength Ti:Sapphire laser source.

Laser action was achieved in the $Nd^{3+}$ $^4F_{3/2} \rightarrow {}^4I_{11/2}$ transition [19] by butting plane mirrors to the end faces of the device and pumping the waveguide at 808 nm. Thresholds as low as 21 mW of absorbed power were obtained with these devices using two HR mirrors. With a 3 % output coupler the lasing threshold rose to 41 mW of absorbed power and a slope efficiency of 6 % was obtained (Figure 5.8). Maximum output power with this configuration was 8.5 mW for an absorbed power of 249 mW, although no effort was made to optimise the overlap of the pump and signal radiations. An optical spectrum analyser was used to measure the output laser wavelength of 1059 nm (the graph of intensity versus wavelength is given in Figure 5.9), a value expected for neodymium ions in BK-7 glass [12]. It was also noted that the output of the laser waveguide remained TE polarised regardless of pump polarisation, a result measured with a Glan-Thompson polariser and confirmed in several similar devices. Such birefringence is common to ion-exchanged waveguides and attributed to localised changes in density and stress in the area of raised refractive index [18].

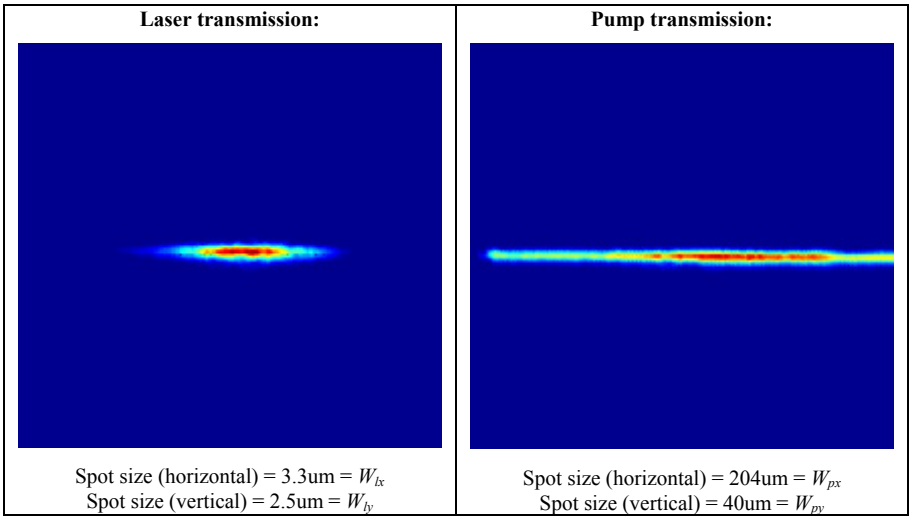


**Figure 5.10:** Mode profiles for the pump and laser transmissions of a buried intersubstrate ion-exchanged planar waveguide laser. The values, $W_{lx}$, $W_{ly}$, $W_{px}$, and $W_{py}$, refer to the $1/e^2$ intensity radius for the laser signal and pump transmission of the buried channel waveguide in the horizontal (non-guiding) and vertical (ion-exchanged) planes respectively.

Mode profiling of the output from the buried waveguide was performed with a silicon camera and PC based evaluation software. It was observed that both the laser output and pump throughput were in the fundamental spatial-mode, with guided output dimensions ($1/e^2$ intensity radius) of 3.3 μm and 2.5 μm respectively. Mode

dimensions in the unguided direction were determined as 40 μm for the laser output and 204 μm for the pump throughput. Mode profiles for the laser output and pump throughput are given in Figure 5.10.

Propagation loss in the waveguide was estimated by investigating the relationship between laser threshold and output coupling [30]. Assuming negligible lower laser level population, constant loss with variable pump intensity, and constant laser mode size, the threshold of the laser, $P_{th}$, is expected to obey the equation [30,31]:

$$P_{th} = \frac{\pi h \upsilon_p}{4\sigma_e \tau}\left(W_{lx}^2 + W_{px}^2\right)^{1/2}\left(W_{ly}^2 + W_{py}^2\right)^{1/2}\left(2\alpha l - \ln\left(R_1 R_2\right)\right) \qquad (5.2)$$

where $h$ is Planck's constant, $\upsilon_p$ is the pump frequency, $\sigma_e$ is the emission cross-section of Nd ions in a borosilicate glass [19], $\tau$ is the fluorescence lifetime, $l$ is the length of the monolithic cavity, $\alpha$ is the propagation loss coefficient, and $R_1$ and $R_2$ are mirror reflectivities corresponding to a high reflector ($R_1$ = 1) and an output coupler ($R_2 = R$) respectively. By varying the output coupler used, a plot of threshold power against -ln$R$ was produced, the result of which is given in Figure 5.11. At the x-axis intercept of this graph the incident threshold power drops to zero and -ln$R$ becomes equal to $2\alpha l$, the internal round trip losses of the laser waveguide. Conversion of the measured intercept value of -0.029 into a loss measured in dB cm$^{-1}$ is performed using the equation:

$$\text{Loss (dB cm}^{-1}\text{)} = (10 \log [e^{-\alpha l}]) / l_{(cm)} \qquad (5.3)$$

which gives a propagation loss in the buried waveguide of 0.1 dB cm$^{-1}$.

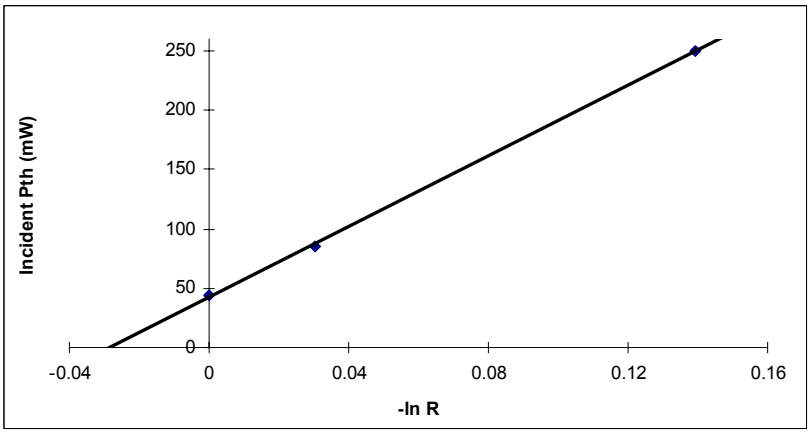


**Figure 5.11**: A graph depicting the dependence of laser threshold power with output coupling for a buried laser waveguide device. The intercept value of -0.029 can be used to determine the loss of the waveguide by calculation.

Unfortunately, the availability of suitable mirror sets limited these experiments to just three output couplers, corresponding to the three points on the graph of Figure 5.11. However, separate calculations of the expected threshold and slope efficiency, $\eta$, can also be used to confirm this result, and the relation [31]:

$$\eta = \frac{\upsilon_l}{\upsilon_p} \frac{-\ln(R_1 R_2)}{2\alpha l - \ln(R_1 R_2)} \eta_q \frac{W_{lx} W_{ly} \left(2W_{px}^2 + W_{lx}^2\right)^{1/2} \left(2W_{py}^2 + W_{ly}^2\right)^{1/2}}{\left(W_{px}^2 + W_{lx}^2\right)\left(W_{py}^2 + W_{ly}^2\right)} \tag{5.4}$$

where $\upsilon_l$ is the signal frequency and $\eta_q$ is the quantum efficiency of the device (assumed to be 100% to obtain an upper limit for propagation loss), leads to an upper limit for the propagation loss of 0.4 dB $cm^{-1}$, a result which compares well with the losses achieved by alternative potassium ion-exchange processes in neodymium-doped BK-7 glass [12,19].

## 5.9 Conclusions

This chapter describes a novel solid-state fabrication technique for the production of single-step buried $K^+$-$Na^+$ ion-exchanged laser waveguides in neodymium-doped BK-7 glass. The key to this process is the direct bonding technique which provides atomic contact between the two substrate layers and a 350 °C heat treatment suitable for simultaneous annealing and inter-substrate ion-exchange. Opposing chemical gradients of potassium and sodium across the bonded interface were provided by modifying the composition of the cladding material from that of commercially available BK-7 glass. It has been shown that replacing 4 wt.% of $Na_2O$ with $K_2O$ in the cladding glass is sufficient for the production of a single-mode waveguide in an adjoining neodymium doped BK-7 substrate. Characterisation of laser performance from the buried waveguide gives a propagation loss of less than 0.4 dB $cm^{-1}$ for the TE polarised laser output. These initial results suggest that optimisation of glass composition and heat treatments could lead to efficient low-loss buried waveguide devices for use with integrated optics. The potential for bonding large wafers of material (to be diced into many smaller devices) for the mass production of low-loss ion-exchanged waveguides could also prove ideal for fabricating laser waveguides with long absorption lengths, such as erbium-doped devices.

## REFERENCES

[1] T. Izawa and H. Nakagome, "*Optical waveguide formed by electrically induced migration of ions in glass plates*", Applied Physics Letters, Vol. 21, p.584-586 (1972).

[2] H. M. Garfinkel, "*Ion-exchange equilibria between glass and molten salts*", The Journal of Physical Chemistry, Vol. 72, No. 12, p.4175-4181 (1968).

[3] T. G. Giallorenzi, E. J. West, R. Kirk, R. Ginther, and R. A. Andrews, "*Optical waveguides formed by thermal migration of ions in glass*", Applied Optics, Vol. 12, No. 6, p.1240-1245 (1973).

[4] T. Findakly, "*Glass waveguides by ion exchange: a review*", Optical Engineering, Vol. 24, No. 2, p.244-250 (1985).

[5] R. V. Ramaswamy and R. Srivastava, "*Ion-exchanged glass waveguides: a review*", Journal of lightwave technology, Vol. 6, No. 6, p.984-1002 (1988).

[6] N. V. Nikonorov and G. T. Petrovskii, "*Ion-exchange glasses in integrated optics; the current state of research and prospects (a review)*", Glass Physics and Chemistry, Vol. 25, No. 1, p.16-55 (1999).

[7] J. E. Gortych and D. G. Hall, "*Fabrication of planar optical waveguides by $K^+$-ion exchange in BK7 and Pyrex glass*", IEEE Journal of Quantum Electronics, Vol. QE-22, No. 6, p.892-895 (1986).

[8] C. R. Lavers, B. J. Ault, and J. S. Wilkinson, "*Characterisation of secondary silver ion exchange in potassium-ion-exchanged glass waveguides*", Journal of Physics, D: Applied Physics, Vol. 27, p.235-240 (1994).

[9] D. Salazar, H. Porte, and H. Márquez, "*Optical channel waveguides by copper ion-exchange in glass*", Applied Optics, Vol. 36, No. 34, p.8987-8991 (1997).

[10] R. G. Walker, C. D. W. Wilkinson, and J. A. H. Wilkinson, "*Integrated optical waveguiding structures made by silver ion-exchange in glass*", Applied Optics, Vol. 22, No. 12, p.1923-1928 (1983).

[11] T. Feuchter, E. K. Mwarania, J. Wang, L. Reekie, and J. S. Wilkinson, "*Erbium-doped ion-exchanged waveguide lasers in BK-7 glass*", IEEE Photonics Technology Letters, Vol. 4, No. 6, p.542-544 (1992).

[12] E. K. Mwarania, J. Wang, J, Lane, and J. S. Wilkinson, "*Neodymium-doped ion-exchanged waveguide lasers in BK-7 glass*", Journal of Lightwave Technology, Vol. 11, No. 10, p.1550-1558 (1993).

[13] J. Albert and G. L. Yip, "*Refractive-index profiles of planar waveguides made by ion-exchange in glass*", Applied Optics, Vol. 24, No. 22, p.3692-3693 (1985).

[14] A. Lupascu, A. Kevorkian, T. Boudet, F. Saint-Andre, D. Persegol, and M. Levy, "*Modelling ion exchange in glass with concentration-dependent diffusion coefficients and mobilities*", Optical Engineering, Vol. 35, No. 6, p.1603-1610 (1996).

[15] G. L. Yip and J. Albert, "*Characterisation of planar optical waveguides by $K^+$-ion exchange in glass*", Optics Letters, Vol. 10, No. 3, p.151-153 (1985).

[16] P. G. Noutsios and G. L. Yip, "*Characterisation and modelling of planar surface and buried glass waveguides made by field-assisted $K^+$ ion exchange*", Applied Optics, Vol. 31, No. 25, p. 5283-5291 (1992).

[17] A. K. Varshneya, "*Fundamentals of inorganic glasses*", Academic Press (1994).

[18] A. Brandenburg, "*Stress in ion-exchanged glass waveguides*", Journal of Lightwave Technology, Vol. LT-4, No. 10, p.1580-1593 (1986).

[19] E. K. Mwarania, "*Planar ion-exchanged waveguide lasers in glass*", University of Southampton, Thesis (1992).

[20] C. Thévenin-Annequin, M. Levy, and T. Pagnier, "*Electrochemical study of the silver-sodium substitution in a borosilicate glass*", Solid State Ionics, Vol. 80, p.175-179 (1995).

[21] S. Honkanen and A. Tervonen, "*Experimental analyis of $Ag^+$-$Na^+$ exchange in glass with Ag film ion sources for planar optical waveguide fabrication*", Journal of Applied Physics, Vol. 63, No. 3, p.634-639 (1988).

[22] J. Haisma, B. A. C. M. Spierings, U. K. P. Biermann, and A. A. van Gorkum, "*Diversity and feasibility of direct bonding: a survey of a dedicated optical technology*", Applied Optics, Vol. 33, No. 7, p.1154-1169 (1994).

[23] A. Plößl and G. Kräuter, "*Wafer direct bonding: tailoring adhesion between brittle materials*", Materials Science and Engineering, Vol. R25, No. 1-2, p.1-88 (1999).

[24] S. Pélissier, F. Pigeon, B. Biasse, M. Zussy, G. Pandraud, and A. Mure-Ravaud, "*New technique to produce buried channel waveguides in glass*", Optical Engineering, Vol. 37, No. 4, p. 1111-1114 (1998).

[25] C. Ciminelli, A. D'Orazio, M. De Sario, C. Geradi, V. Petruzzelli, and Francesco Prudenzano, "*Effects of thermal annealing on the optical characteristics of $K^+$-$Na^+$ waveguides*", Vol. 37, No. 9, p.2346-2356 (1998).

[26] D. W. Tenquist, R. M. Whittle, and J. Yarwood, "*University Optics*" Volume 1, Iliffe (1969).

[27] G. A. C. M. Spierings, J. Haisma, and T. M. Michelsen, "*Surface-related phenomena in the direct bonding of silicon and fused-silica wafer pairs*", Philips Journal of Research, Vol. 49, p.47-63 (1995).

[28] J. Haisma, G. A. C. M. Spierings, T. L. Michielsen, and C. L. Adema, "*Surface preparation and phenomenological aspects of direct bonding*", Philips Journal of Research, 49, p.23-46, 1995.

[29] P. J. Goodhew and F. J. Humphreys, "*Electron microscopy and analysis*" 2nd Ed., Taylor and Francis (1988).

[30] D. Findlay and R. A. Clay, "*The measurement of internal losses in 4-level lasers*", Physics Letters, Vol. 20, No. 3, p.277-278 (1966).

[31] W. P. Risk, "*Modelling of longitudinally pumped solid-state lasers exhibiting reabsorption losses*", Journal of the Optical Society of America B, Vol. 5, No. 7, p.1412-1423 (1988).

# Chapter 6
# UV-WRITTEN BURIED CHANNEL WAVEGUIDE LASERS IN DIRECT-BONDED INTERSUBSTRATE ION-EXCHANGED Nd:SGBN

## 6.1 Introduction

Photosensitivity is a fundamental characteristic of silica-based glasses, allowing the refractive index of the material to be changed by the application of short wavelength radiation [1]. Discovered by Hill et al. in 1978 [1], photosensitivity was first observed in a germanium-doped optical fiber core where a standing wave interference pattern created with an argon-ion laser induced a permanent Bragg refractive index grating capable of reflecting the incident beam. The refractive index change observed in these first processes was typically around $10^{-6}$ and no significant applications were derived from this initial technology as Bragg reflection would only work at the wavelength of the writing beam [1]. However, interest in photosensitivity surged ten years later when Meltz et al. demonstrated that Bragg gratings could be induced into a fiber core by side exposure through the cladding layer with a UV exposed interference pattern [2]. This development allowed refractive index modulations of almost any period to be produced, opening up the fields of photosensitivity and fiber-based Bragg grating filters [3-5]. The next major breakthrough came in 1993 when Lemaire et al. demonstrated that the photosensitivity of silica fibers could be increased by several orders of magnitude by high pressure loading of the glass with gaseous hydrogen [6]. With changes in refractive index now available up to $10^{-2}$ [7], it soon became possible not only to modify the cores of optical fibers but also to UV-write channel waveguide structures directly into planar substrate materials, providing an alternative route towards the fabrication of integrated optical devices [7-10].

The intersubstrate ion-exchange technique introduced in Chapter 5 provides a novel solid-state solution for the fabrication of buried low-loss planar waveguide devices in glass [11]. Here this theme is continued, as direct-UV-writing is used to bring these structures one dimension closer to an application in integrated optical technology by the introduction of channel confinement in the buried waveguide layer. Both challenging and interesting to develop, the inclusion of photosensitivity into these direct-bonded samples was based on the simple problem of *how* channel confinement

could be created in a waveguide layer buried more than a millimeter below the surface of a device. With no single-step solution immediately obvious, and the route of polishing back the top cladding layer to micron-order waveguide dimensions (allowing a secondary process such as etching or ion-beam milling) undesirable, the chosen route forward was optical.

Discussed in this chapter are the origins of photosensitivity in germanosilica-based glasses and their application towards the development of single-mode buried channel waveguide laser devices in direct-bonded intersubstrate ion-exchanged structures. The work presented was performed in collaboration with Daniel Milanese [12-14] of the Politecnico de Turino in Italy, who prepared the complex rare-earth doped SGBN substrate required for this experiment. Described are the design and fabrication procedures required to create a buried waveguide layer in a neodymium-doped SGBN glass, and the direct-UV-writing process used to create channel waveguide structures in that layer. Finally, the optical characteristics of a buried channel waveguide laser device are presented.

### 6.2 Photosensitivity and UV induced refractive index change

Photorefractivity [15] and photosensitivity are two inherently different processes that both arise from a localised change in refractive index when a material is exposed to light, although the terms are often confused. The first of these processes, the photorefractive effect, was described previously in Chapter 4 and refers to a phenomenon usually ascribed to crystalline materials with a second-order nonlinearity, allowing the refractive index to be changed via a photoinduced internal electric field [16]. The later term, photosensitivity, was appointed to photoinduced refractive index changes in glass [1], where the lack of internal symmetry prohibits the electro-optic effect and must therefore arise from a different origin. This is most widely believed to be due to the formation of molecular bonding defects in exposed areas of the glass [17], which alter the local refractive index via changes in absorption characteristics and stress. However, it should be noted that despite more than a decade of research into the subject by various groups worldwide [18-21] a coherent theory for the mechanism responsible for UV-induced refractive index change in

germanosilicate glasses has yet to be developed. As such, the reader is directed towards the related References [3,17,21] for more detailed discussions on this topic.

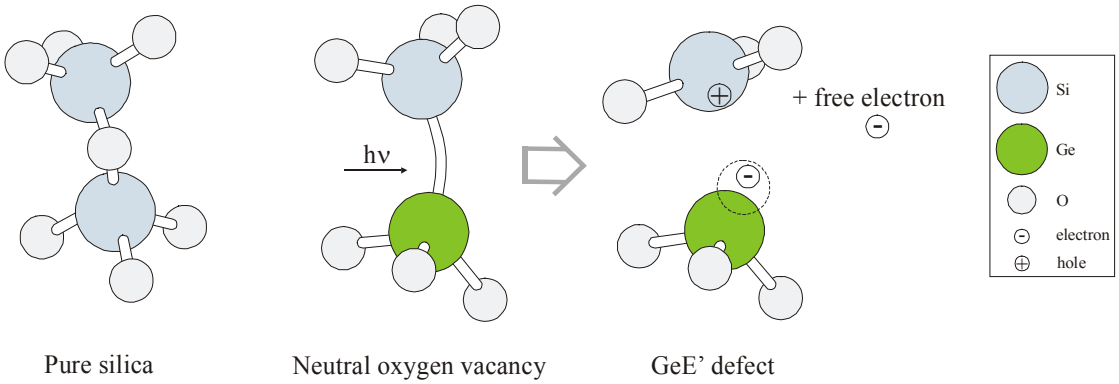


**Figure 6.1:** The tetrahedral structure of pure silica and the neutral oxygen vacancy defect common to germanosilicate glasses. Upon UV illumination, the chemical bond between silicon and germanium atoms in the neutral oxygen vacancy defect readily breaks, forming a GeE' defect [3].

To date, the most widely accepted mechanism for UV-written refractive index changes in germanosilicate glass is based on the presence of oxygen-deficiency defect centres in the host material [3,17,20]. While the general structure of germanosilica glass is based on the same tetrahedral shapes found in pure silica, consisting of a central silicon (or germanium, as both have a similar number of valence electrons) atom bonded to four oxygen atoms in a localised glass network [22-23], numerous defects are known to develop around the germanium sites when insufficient oxygen atoms are present, all of which are associated with strong absorption bands (in the range of 180-350 nm) in the glass [3]. One of the most common such defects is the neutral oxygen vacancy (Figure 6.1), which consists of a direct chemical bond between neighbouring germanium and silicon atoms where an oxygen atom is missing, and features a characteristic absorption peak around 245 nm [3]. UV illumination readily breaks this germanium-silicon bond, forming a GeE' defect centre [24] in the glass by trapping a hole at the oxygen vacancy site and liberating an electron associated with the germanium atom. The subsequent change in molecular shape caused by the removal of this electron is believed to increase the absorption coefficient of the glass in the UV spectral region [3], inducing a positive refractive index change in the material (even at wavelengths far from the photosensitive band) via the Kramers-Kronig relation [3], and facilitating the direct formation of waveguide structures in germanosilicate glass with a UV writing beam.

## 6.3 Direct UV writing

Since the first demonstration by Svaalgard et al. in 1994 [7], direct UV writing has proven to be a successful and versatile technique for lab-based creation of optical confinement in thin film germanosilicate substrates [7,25-30]. Based on the localised change in refractive index obtained by short wavelength radiation, direct UV writing gains its name from the ability to literally draw waveguide structures directly into photosensitive materials by computer-controlled scanning of a focussed continuous-wave ultraviolet beam (Figure 6.2) [7]. Such point-to-point refractive index changes are ideally suited to the fabrication of compact two-dimensional structures in large wafer substrates and surprisingly versatile when compared to other UV patterning techniques, which often rely on cylindrical focussing [9] or deposited metal layers [10,31] to create waveguide definition. Instead, parameters such as the physical size and refractive index step of a direct-UV-written waveguide are controlled by adjustment of the focussing conditions, spot size, input power, and scan rate of the writing beam, facilitating precisely defined refractive index structures. Used in the design and fabrication of various optical devices, ranging from the first direct-UV-written channel waveguides [7,26] towards more complex structures based on Bragg gratings [30], band splitters [27], and directional couplers [27,30], the primary advantage of this technique is the in-situ control of the computer-based waveguide pattern, which eliminates the need for costly photolithography and facilitates a rapid turnaround for device optimisation based on continuing results [20].

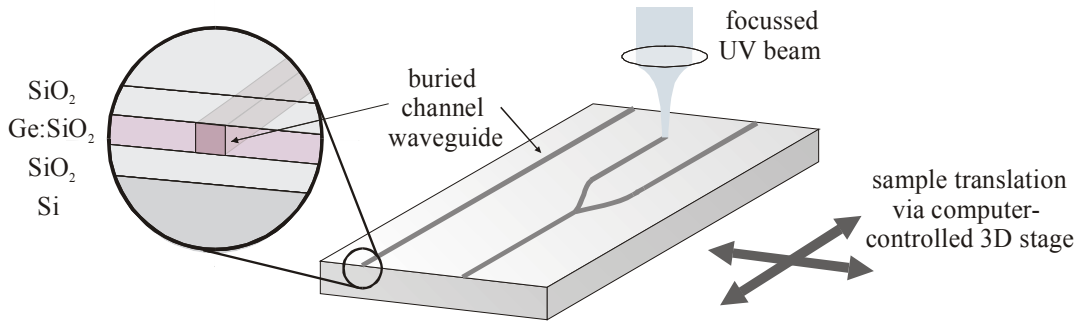


**Figure 6.2:** Direct UV writing into a thin film germanosilica layer [7]. Translation of the photosensitive sample under a focussed cw UV beam allows waveguide patterns to be designed and implemented with a high degree of versatility, and channel waveguides, Y-junctions, and Bragg gratings have all been demonstrated in PECVD deposited buried germanosilica layers [30].

To date, the majority of direct UV writing processes have been performed on buried thin film germanosilicate layers based on Plasma Enhanced Chemical Vapour Deposition (PECVD) silica-on-silicon wafers [7,25-30]. Such multilayered structures are developed to allow UV writing through a cladding layer and directly into the photosensitive material (Figure 6.2 inset), offering improved mode quality, low losses (of $\leq 0.2$ dB $cm^{-1}$ [26]), and efficient coupling to optical fibers [28]. However, as the demand for novel telecommunications devices grows, recent experiments have expanded to involve more versatile bulk glasses and substrate materials (including borosilicates [12], fluoroaluminates [32], and chalcogenides [33]) which have the advantages of being potentially simpler to produce and more readily tailored to incorporate large amounts of exotic and volatile components, not usually available by wafer deposition techniques, for a wider range of applications and effects.

## 6.4 UV written structures in SGBN

One novel glass type recently developed for direct UV writing processes is SGBN [12-14], a bulk multicomponent oxide glass named after its main constituent parts of silica, germania, boron, and sodium (Na), and the first to incorporate simultaneous photosensitivity, ion-exchangability, and rare-earth doping (although never previously in the same device). Previously investigated by Daniel Milanese in a joint project between the Optoelectronics Research Centre and the Politecnico de Turino in Italy [12], SGBN was originally designed to incorporate the popular properties exhibited by commercially available BK-7 (see Section 5.5) with germanium-doped photosensitivity to facilitate a wide range of possible waveguide fabrication processes and effects. This is mirrored in the basic composition of the glass, which contains a similar borosilicate basis to that of BK-7 with additional germanium and sodium contributions for UV writing [12] and ion-exchange [14] respectively (Table 6.1). SGBN exhibits the characteristic absorption peak of 240 nm associated with germanosilicate glass, with an absorption of 40 dB $cm^{-1}$ at the widely used UV-writing wavelength of 244 nm, and a UV-induced refractive index change of $5\times10^{-4}$ is the largest measured in this (6 wt.% Ge doped) material [12].

| Glass | Composition (weight %) | | | | | | |
|---|---|---|---|---|---|---|---|
| | $SiO_2$ | $B_2O_3$ | $Na_2O$ | $K_2O$ | $Ba_2O$ | $GeO_2$ | Trace |
| SGBN | 64.0 | 9.2 | 20.7 | - | - | 6.1 | - |
| BK-7 | 69.6 | 9.9 | 8.4 | 8.4 | 2.5 | - | 1.2 |

**Table 6.1**: Comparative compositions of SGBN and commercially available BK-7 glass [12,36].

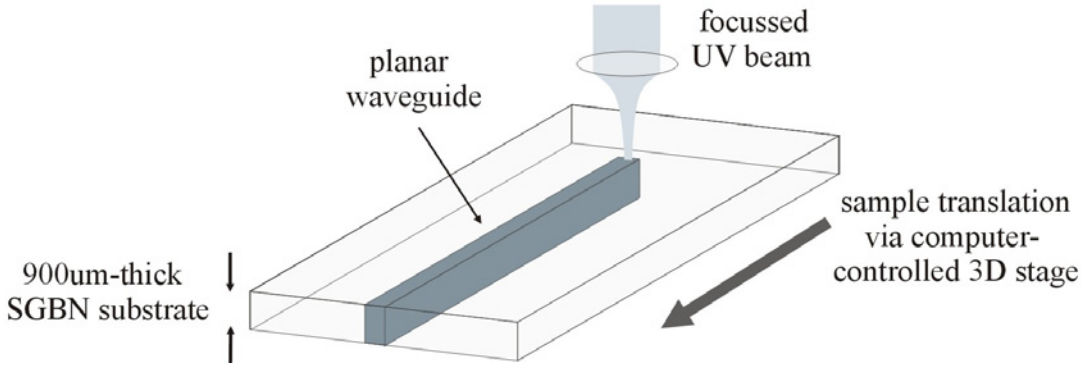


**Figure 6.3:** Direct UV writing of planar waveguide structures into SGBN [12]. Previous experiments have demonstrated that waveguide structures can be UV-induced through almost a millimeter of the material, depending on glass composition (increased germanium content also increases the absorption of the glass at 244 nm) [12]. With a stationary beam, channel waveguide structures can also be fabricated through the material with this technique [12].

To date, several UV written waveguide structures have been demonstrated in SGBN [12], including surface-written channel waveguides (achieved only in a more photosensitive 20 wt.% Ge doped material), and bulk-written channel and planar waveguide structures, which are both transversely written by a UV beam through almost a millimeter of the material (Figure 6.3) [12]. The latter result is of particular importance to the experiments performed in this chapter, providing the penetration depth required for direct UV writing applicable to deeply buried intersubstrate ion-exchanged waveguides. However, all UV-written waveguides created in bulk SGBN feature very high propagation losses of 6 dB $cm^{-1}$ or more [12] (depending on glass composition), which prevent any real application. As SGBN is prepared to include sodium, making the material suitable for $K^+$-$Na^+$ ion-exchange, one approach to improve these losses is to find a new route towards combining the versatile characteristics of the bulk glass with the improved losses and mode profiles associated with buried waveguide structures [28].

To this end, the remainder of this chapter describes our initial study towards creating buried channel waveguide lasers in neodymium-doped SGBN glass by a combination of direct-bonding [34-35] and direct UV writing techniques. Based on the intersubstrate ion-exchange technique presented in Chapter 5, direct bonding is used to provide a region of atomic contact between Nd:SGBN and a potassium-rich borosilicate cladding substrate, between which $K^+$-$Na^+$ ion-exchange can occur [11]. By taking this approach a low-loss buried planar waveguide layer is fabricated in the Nd:SGBN glass, which retains the photosensitive characteristics of the bulk material and into which single-mode channel waveguide structures can be directly written with a focussed UV beam.

## 6.5 Glass design and preparation

In order to extend the design of an intersubstrate ion-exchanged planar waveguide device to incorporate direct-UV-written channel waveguide structures, several additional factors must first be included in the design of the glass substrate materials. For example, the two glass layers must be compatible for a range of processes and effects (the key elements of which are illustrated in Figure 6.4), including; direct bonding, intersubstrate ion-exchange, waveguiding, direct UV writing, and subsequent laser action. From these initial requirements, the combination of SGBN and BK-7-type glass seems ideal for this experiment, as both are based on a composition similar to that of commercially available BK-7 [36] and so exhibit similar thermal expansion coefficients ($\alpha_{SGBN} = 88\times10^{-7}$ $K^{-1}$ [12] and $\alpha_{BK\text{-}7} = 83\times10^{-7}$ $K^{-1}$ [36]) and compatibility for direct bonding. SGBN can also be doped to include previously investigated concentrations of germanium and boron for photosensitivity, allowing a UV induced refractive index change of up to $5\text{x}10^{-4}$ to be written through almost a millimeter of the material [12]. The ability to incorporate rare-earth ions into the host material [14] also allows neodymium to be added to the SGBN for laser action, although in this experiment the amount was limited due to early problems of annealing the cast glass. As the BK-7-type cladding substrate is potassium rich and of a lower refractive index than the rare-earth doped material, this also facilitates intersubstrate $K^+$-$Na^+$ ion-exchange and planar waveguide confinement in the photosensitive substrate, completing the diverse range of effects and compatibility required of the two materials.

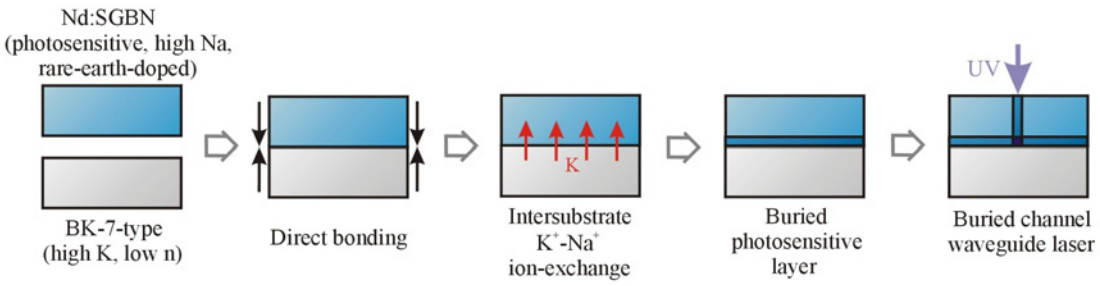


**Figure 6.4:** Key processing stages in the design and fabrication of a buried channel laser waveguide by a combination of direct bonding and direct UV writing techniques.

Preparation of the rare-earth-doped SGBN material used in this experiment was performed by Daniel Milanese at the Politecnico de Turino in Italy, and began by melting batch powders of $SiO_2$ (63.8 wt.%), $GeO_2$ (6.1 wt.%), $B_2O_3$ (9.2 wt.%), $Na_2O$ (20.7 wt.%), and $Nd_2O_3$ (0.2 wt.%), in a resistance furnace for 2 hours. A temperature range of 850 °C to 1450 °C was available throughout the doping process, the melt being fined at 1400 °C and removed from the furnace at 1300 °C. Cast onto a preheated copper plate, the glass was slowly returned to room temperature to promote structural stability. The second glass type, which forms the cladding layer of the device and acts as a source of potassium for ion-exchange, was the same BK-7-type substrate material used in earlier direct bonding experiments [11]. Based on the chemical composition of commercially available BK-7, the oxide mix was altered to allow an additional 4 wt.% (approx.) of $K_2O$ into the glass by removing an equal amount of $Na_2O$. As demonstrated in Chapter 5, such an offset in glass composition between the BK-7-type and rare-earth doped substrates allows the realisation of buried laser waveguides by internal ion-exchange processes in direct-bonded structures. The refractive indices of the Nd:SGBN and BK-7-type substrates were measured using an Abbe refractometer [37] at a wavelength of 587 nm, giving values of 1.5132 and 1.5105 respectively.

## 6.6 Fabrication of UV written buried channel waveguides

Fabrication of buried channel waveguide devices in Nd:SGBN is performed in two main stages, starting with the direct bonding and intersubstrate ion-exchange required to produce a buried waveguide layer in the photosensitive substrate, and followed by direct UV writing into that layer (Figure 6.4). From each of the Nd:SGBN and BK-7-type glasses a 2-mm-thick substrate, of 30 mm × 10 mm surface area, was diced

and polished to provide an optically flat surface suitable for direct bonding. After cleaning, a mixture of $H_2O_2$-$NH_4OH$-$H_2O$ (1:1:6), followed by several minutes of rinsing in deionised water, was applied to both materials in order to render their surfaces hydrophilic [38]. The doped and undoped layers were then brought into contact at room temperature and finger pressure applied in order to promote adhesive avalanche [39], forcing any excess air or liquid from between the two substrates. Annealing of the sample at 350 °C for 6 hours provided ample bond strength for further machining and sufficient ion-exchange to create a single-mode planar waveguide layer on the photosensitive side of the bonded interface [11]. The increase in refractive index provided by this technique was crudely estimated from the measured refractive indices of the bulk glass, waveguide height, and single-mode nature of the waveguide using a simple mode-solver program, yielding a value of $\sim 5\times10^{-4}$. The rare-earth doped layer of the sample was then polished down to 200 μm, a dimension appropriate for direct UV writing (see next section), followed by dicing and parallel end-face polishing to a final device length of 7.5 mm (Figure 6.5).

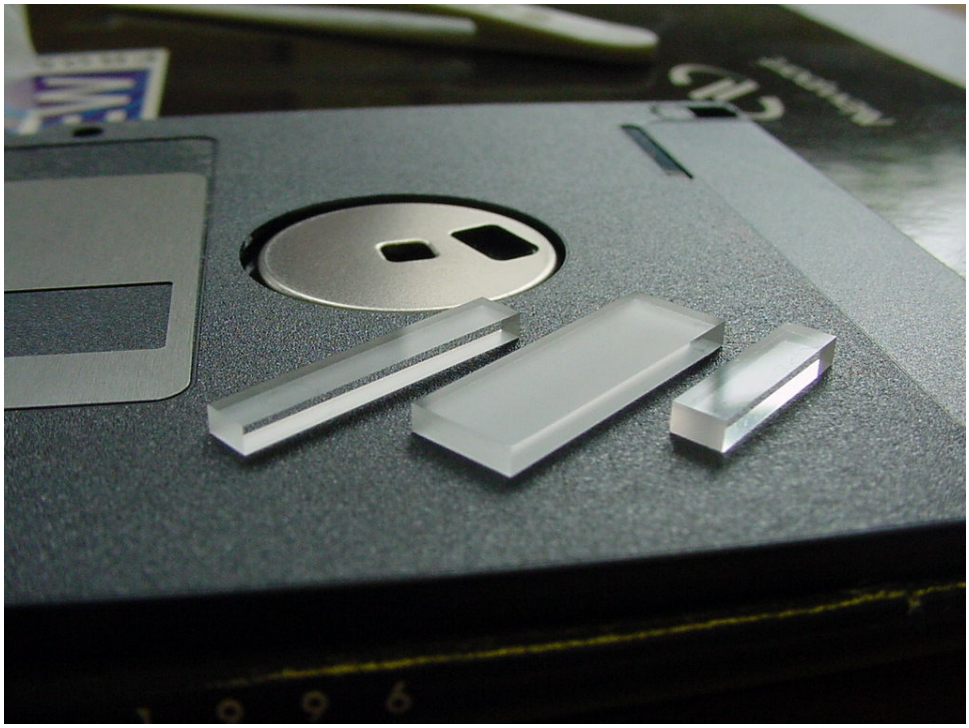

**Figure 6.5:** A photograph of three direct-bonded devices for use in direct-UV-writing experiments. The larger samples each feature a 200-μm-thick Nd:SGBN top layer bonded to a 2-mm-thick BK-7-type substrate. The smaller sample features an Erbium-doped SGBN top layer.

Direct UV writing into the buried waveguide layer was performed using a frequency doubled argon laser at 244 nm. The beam was expanded and collimated to a diameter of 3.1 mm and spatially filtered to provide a uniform beam for focussing on to the rare-earth doped layer of the direct-bonded glass structure. A 35 mm lens was used to focus the UV beam to a calculated 3.3-μm-spot on the top surface of the sample, the beam waist of which was adjusted to coincide with the ion-exchanged layer for maximum intensity UV writing in this area. Channel confinement was created in the buried waveguide layer by translating the sample under the focussed UV beam with a high precision computer controlled three-dimensional translation stage. A localised positive refractive index change was induced in the exposed areas of the glass by the formation of GeE' defect centres in the photosensitive material [3], accompanied by visible darkening of the host substrate. While the overall effect was to create weak vertical slab waveguides in each UV exposed area of the glass, it is only in the focussed ion-exchanged layer where the Nd:SGBN material has undergone two positive refractive index changes that channel waveguiding can occur (Figure 6.6).

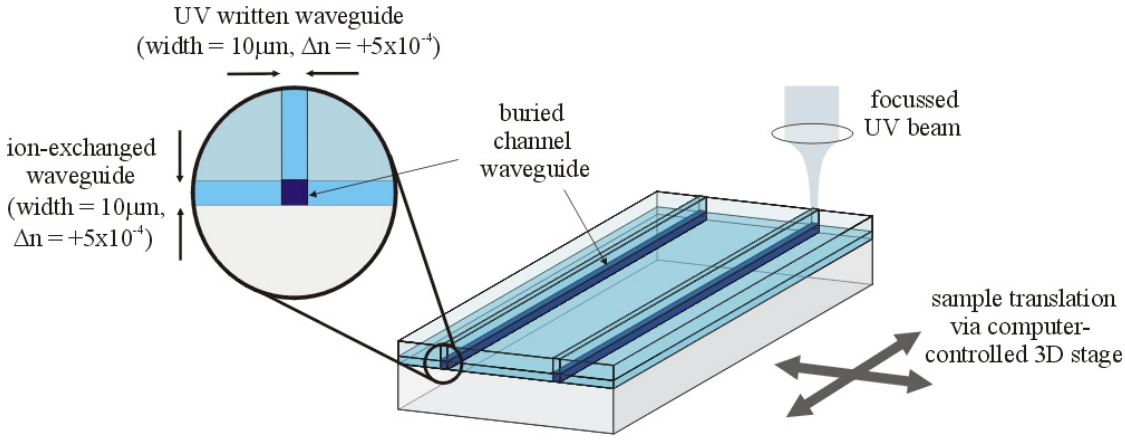


**Figure 6.6:** Buried channel waveguide structures in Nd:SGBN by a combination of direct bonding and direct UV writing techniques. Here, the intersection of a vertical planar waveguide induced through the photosensitive upper cladding layer by a focussed UV beam and an intersubstrate ion-exchanged buried waveguide layer, provides a local positive change in refractive index suitable for channel confinement. Optical confinement in the vertical waveguides is observed to be very weak, and the refractive index change of $5\times10^{-4}$ is assumed to occur locally at the high intensity focus of the beam.

## 6.7 Device optimisation

Optimisation of the channel waveguide geometry (physical size, mode profile etc.) was performed by adjusting the thickness of the Nd:SGBN top cladding layer and the writing intensity and translation speed of the focussed UV beam. Several

combinations of these parameters were investigated in a variety of direct-bonded samples, with variations of 50-μm- to 2-mm-thick cladding layers, 50 mW to 250 mW input powers, and sample translation speeds of between 1 mm $min^{-1}$ and 10 mm $min^{-1}$ under the UV beam. The results of these experiments particularly useful as a means to limit unwanted thermal effects in the photosensitive glass substrate [12], such as glass ablation and photothermal expansion [32], which can damage the device and prevent optical confinement. Over the range of input powers used, these effects were mainly limited to those samples with a 50-μm-thick top Nd:SGBN layer, where the photosensitive material became damaged (and often burned through) even with low intensity UV. Conversely, the UV beam seemed unable to fully penetrate the 2-mm-thick samples, such that any UV writing effects were observed only near the top surface and not in the buried waveguide layer. In the subsequently chosen 200-um-thick Nd:SGBN samples, it was noted that the mechanisms of UV induced refractive index change were very sensitive to input power, ranging from no effect, to a positive change in refractive index, and then to a negative change in refractive index [40], all between the input power range of 190 mW to 210 mW. Overall it was determined that writing conditions of 200 mW input power with a translation speed of 10 mm $min^{-1}$ were required to give single-mode channel waveguide confinement in the ion-exchanged layer. Again by crude calculation, this corresponds to a positive refractive index change of $\sim 5\times10^{-4}$ in the buried waveguide layer (assuming a waveguide width of ~ 10 μm and ion-exchanged Δn of $5\times10^{-4}$). Under these conditions over 50 single-mode channel waveguides were written into several similar devices, proving that this is a robust technology. A schematic diagram representing typical dimensions of a buried channel laser waveguide device are given in Figure 6.7.

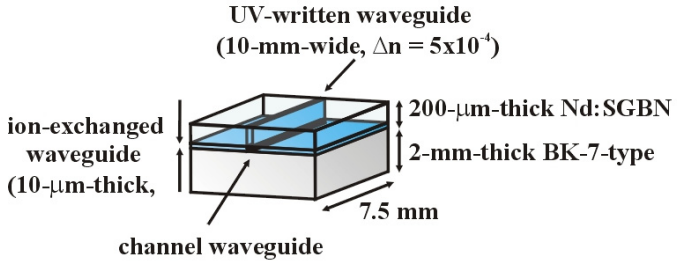


**Figure 6.7:** Typical dimensions of the buried channel waveguide lasers used for device characterisation. In each fabricated structure a separation of around 50 μm was allowed between UV-written waveguides, facilitating potentially hundreds of devices in every sample.

## 6.8 Channel waveguide characterisation

Characterisation of spectroscopy, laser performance, and propagation loss of the device was performed with a tunable (700 nm to 850 nm) Ti-Sapphire laser using the methods and equations previously described in Chapter 5. Pump radiation was focussed for launch into each buried channel waveguide by means of a ×10 microscope objective with a measured input spot size of approximately 3 μm. Optimisation of the launch was performed in relation to the fluorescence measured by a silicon detector, and an absorption of 31 % and launch efficiency of 13 % (a low value associated with modal-mismatch and the difficulty of isolating the fluorescence of the buried channel in this mixed waveguide geometry) were calculated from measurements of input and output pump power from the waveguide. It was observed that absorption tails off with increased input power due to pump saturation (Figure 6.8), an effect due to the limited amount of rare-earth dopant in the substrate material (there is only so much neodymium to excite into higher energy levels) [41].

Laser action was achieved in the $Nd^{3+}$ $^4F_{3/2} \rightarrow {}^4I_{11/2}$ transition by butting plane mirrors to the end faces of the device and pumping a selected channel waveguide at 808 nm. While a comparison of laser performance between the bulk material, the horizontal intersubstrate ion-exchanged planar waveguide, the vertical UV written planar waveguides, and the buried channel waveguides, would provide valuable comparative results as to the efficiency of each process, laser action could only be achieved in the buried channel waveguides. This effect is assumed to be due to pump saturation, and any future devices based on this technology will incorporate a higher concentration of rare-earth ions. Nevertheless, lasing thresholds as low as 2.7 mW of absorbed power were obtained with these channel waveguide devices using two HR mirrors, showing ten times improvement over the planar waveguide version [11]. With a 3 % output coupler the lasing threshold rose to 4.5 mW of absorbed power and a slope efficiency of 9 % was obtained (Figure 6.9), also showing improved performance over the planar device. Maximum output power with this configuration was 2 mW for an absorbed power of 32 mW, although no effort was made to optimise the overlap of the pump and signal radiations for this initial demonstration. The laser emission wavelength was measured as 1059 nm using a triple grating spectrograph (Figure 6.10), and it was

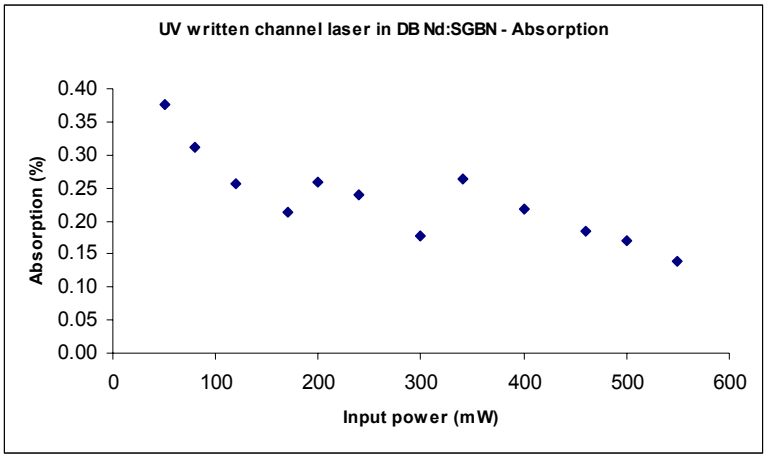


**Figure 6.8:** Absorption characteristics of a UV-written buried channel waveguide in Nd:SGBN. The downward trend of the curve with increased input power denotes pump saturation due to insufficient rare-earth-dopant concentration.

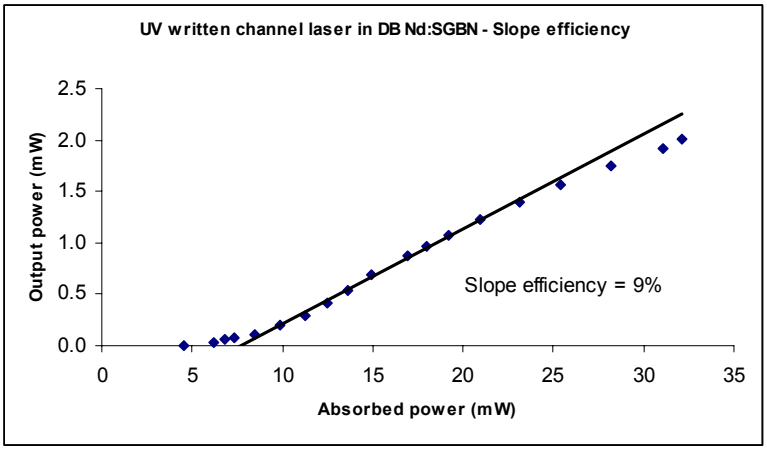


**Figure 6.9:** A graph of absorbed pump power versus laser signal output power for a buried channel waveguide. The line of best fit provides a value of 9% for the slope efficiency of the device.

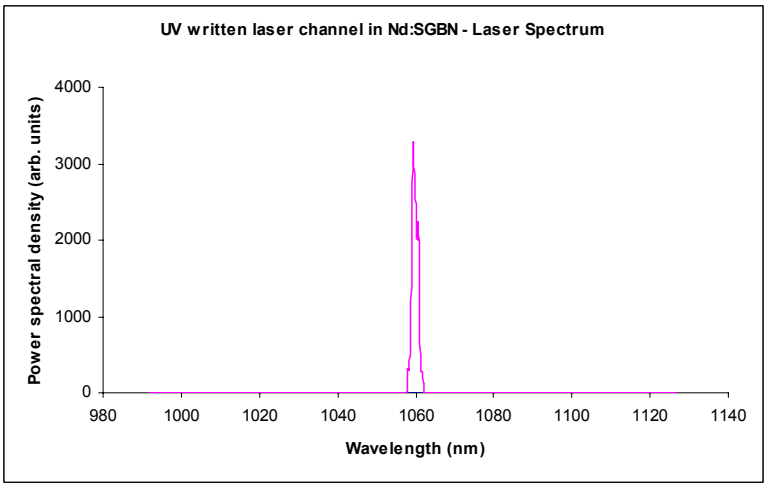


**Figure 6.10:** Output laser wavelength for a buried channel waveguide in Nd:SGBN. An output wavelength of 1059 nm is typical for laser action in neodymium-doped borosilicate glasses [11,41].

noted that the output of the laser waveguides remained TM polarized regardless of pump polarisation, an effect opposite to that observed in the previous inter-substrate ion-exchanged buried laser waveguide devices [11]. Such birefringence is common to UV written structures and believed to result from the stress induced by local changes in material density [42], although this difficult to investigate in such a buried mixed-waveguide geometry.

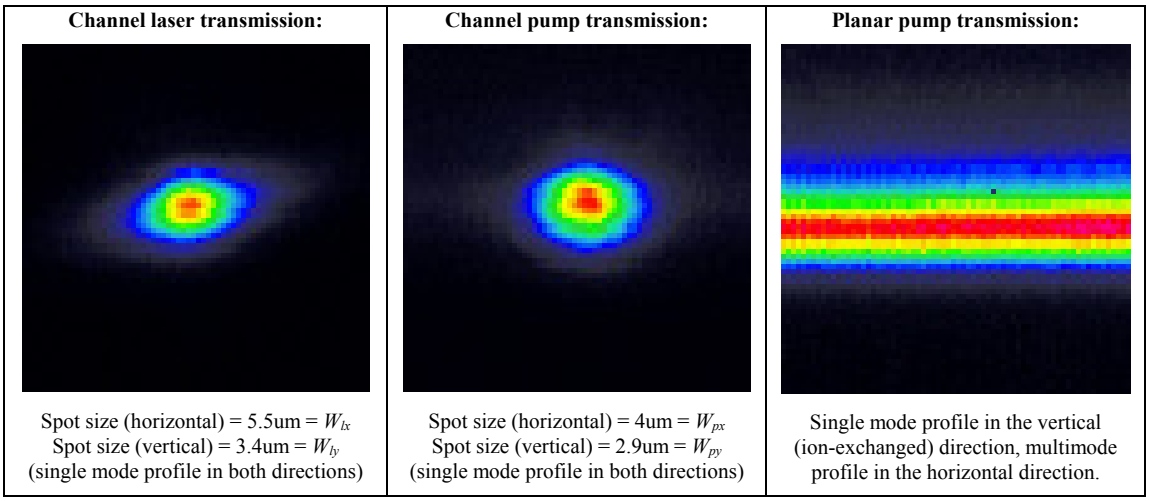


**Figure 6.11:** Mode profiles for the pump and laser transmissions of a buried channel waveguide, and the pump transmission of a section of the buried intersubstrate ion-exchanged waveguide layer. The values, $W_{lx}$, $W_{ly}$, $W_{px}$, and $W_{py}$, refer to the $1/e^2$ intensity radius for the laser signal and pump transmission of the buried channel waveguide in the horizontal (UV-written) and vertical (ion-exchanged) planes respectively.

Mode profiling of the output from the buried waveguide was performed with a silicon camera and PC based evaluation software, the results of which are given in Figure 6.11. It was observed that both the laser output and pump throughput were in the fundamental spatial-mode, with Gaussian mode profiles in both guided directions. A guided output spot size ($1/e^2$ intensity radius) of 3.4 μm × 5.4 μm was measured for the laser output in the vertical (ion-exchanged) and horizontal (UV written) planes respectively, while the pump throughput spot size was 2.9 μm × 4.0 μm. Such near-circular mode profiles indicate good possibility for low loss coupling to optical fibers, although further investigation of the combined ion-exchange and direct UV writing parameters (such as refractive index change and the physical waveguide size) are required for future improvement.

The simplest way to measure loss in this relatively unexplored glass type, knowing the least amount of spectroscopic measurements, is via the slope efficiency [43]. The slope efficiency is a definite figure based on a ratio of losses and spot sizes and gives an absolute upper value for the propagation loss in a laser device. This is based on the assumption that all neodymium ions excited into a higher energy level state will contribute to laser action, such that the quantum efficiency of the device, $\eta_q$, is assumed to be 100 %. Using the measured slope efficiency of 9%, the measured spot sizes (see Figure 6.11 for $W_{lx}$, $W_{ly}$ etc.), and the equation [43]

$$\eta = \frac{\upsilon_l}{\upsilon_p}\frac{T}{L+T}\eta_q \frac{W_{lx}W_{ly}\left(2W_{px}^2+W_{lx}^2\right)^{1/2}\left(2W_{py}^2+W_{ly}^2\right)^{1/2}}{\left(W_{px}^2+W_{lx}^2\right)\left(W_{py}^2+W_{ly}^2\right)} \tag{6.1}$$

(where $\upsilon_l$ and $\upsilon_p$ are the signal and pump frequencies, $T$ is the output coupler transmission at the signal wavelength (-ln$R$), and $L$ is the roundtrip internal loss) the upper limit for propagation loss in the direct UV written buried channel waveguide is calculated to be less than 0.3 dB cm$^{-1}$. This result was confirmed with a Findlay-Clay loss measurement investigating the relationship between laser threshold and output coupling [44]. Assuming negligible lower laser level population, constant loss with variable pump intensity, and constant laser mode size, the threshold of the laser, $P_{th}$, is expected to obey the equation [44]:

$$P_{th} = k\,[2\alpha l - \ln(R_1R_2)] \tag{6.2}$$

where $k$ is a constant encompassing the pump and laser mode spatial properties and material parameters, $l$ is the length of the monolithic cavity, $R_1$ and $R_2$ are the mirror reflectivities, and α is the propagation loss coefficient. By varying the output coupler a plot of threshold against -ln($R_1R_2$) was produced (Figure 6.12), the x-axis intercept of which gives an estimate of propagation loss. For our buried channel waveguides a value of 2.3 m$^{-1}$ was measured for $\alpha$, corresponding to a propagation loss of just 0.1 dB cm$^{-1}$. This is a significant result, demonstrating more than twenty times improvement over other direct-UV-written channel waveguides in the bulk SGBN material [12] (a result which may also be based on improved glass performance), and comparing to the ≤ 0.2 dB cm$^{-1}$ channel waveguide propagation losses achieved in PECVD buried germanosilica layers by Svalgaard et al. [26-30].

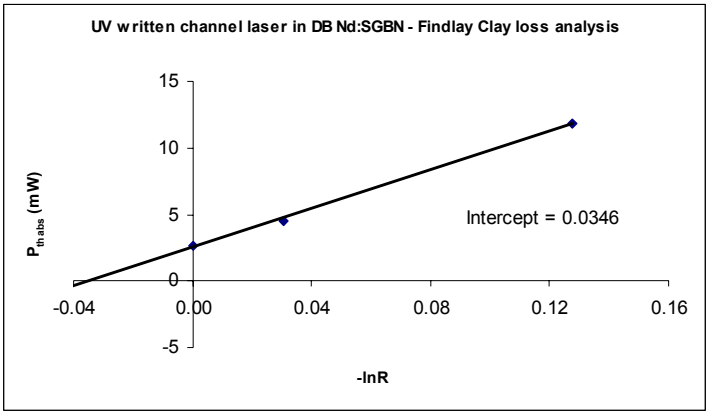


**Figure 6.12:** A graph depicting the dependence of laser threshold power with output coupling for a buried laser waveguide device. The intercept value of -0.0346 can be used to determine the loss of the waveguide by calculation.

## 6.9 Conclusions

In conclusion, this chapter describes a novel fabrication technique for the production of low-loss single-mode buried laser channel waveguides in neodymium-doped SGBN glass. The key to this process is the combination of direct bonding, which provides a buried waveguide layer in the photosensitive glass by intersubstrate ion-exchange, and direct UV writing, which is used to create channel waveguide confinement in that layer. Characterisation of laser performance in the buried channel waveguides demonstrates milliwatt-order laser thresholds, single-spatial-mode operation, and propagation losses of less than 0.3 dB $cm^{-1}$. These initial results suggest that optimisation of glass composition and UV writing conditions could lead to highly efficient low-loss buried channel waveguide devices for use with integrated optics. The potential for bonding large wafers of material (to be diced into many smaller devices) for the mass production of complex UV-written devices could also prove ideal for fabricating laser waveguides with long absorption lengths, such as erbium-doped devices. More generally, the combination of direct bonding and direct UV writing techniques offers extra degrees of design freedom in the realisation of 2D and 3D waveguide structures in multicomponent photosensitive glass.

## REFERENCES

[1] K. O. Hill, Y. Fujii, D. C. Johnson, and B. S. Kawasaki, "*Photosensitivity in optical waveguides: Application to reflection filter fabrication*", Applied Physics Letters, Vol. 32, No. 10, p.647-649 (1978).

[2] G. Meltz, WW. Morey, and W. H. Glen, "*Formation of Bragg gratings in optical fibers by a transverse holographic method*", Optics Letters, Vol. 14, No. 15, p.823-825 (1989).

[3] R. Kashyap, "*Fiber Bragg gratings*", Academic Press (1999).

[4] D. P. Hand and P. St. J Russell, "*Photoinduced refractive index changes in germanosilicate optical fibers*", Optics Letters, Vol.15, No.2, p.102-104 (1990).

[5] A. Othonos and K. Kalli, "*Fiber Bragg gratings: Fundamentals and applications in telecommunications and sensing*", Artch House (1999).

[6] P. J. Lemaire, R. M. Atkins, V. Mizrahi, and W. A. Reed, "*High pressure $H_2$ loading as a technique for achieving ultrahigh UV photosensitivity and thermal sensitivity in $GeO_2$ doped optical fibres*", Electronics Letters, Vol. 29, No. 13, p.1191-1193 (1993).

[7] M. Svalgaard, C. V. Poulsen, A. Bjarklev, and O. Poulsen, "*Direct UV writing of buried singlemode channel waveguides in Ge-doped silica films*", Electronics Letters, Vol. 30, No. 17, p.1401-1403 (1994).

[8] F. Bilodeau, B. Malo, J. Albert, D. C. Johnson, and K. O. Hill, "*Photosensitization of optical fiber and silica-on-silicon / silica waveguides*", Optics Letters, Vol. 18, No. 12, p. 953-955 (1993).

[9] G. Meltz, W. W. Morey, W. H. Glenn, and D. J. Fritz, "*UV-induced Bragg gratings in optical fibers and thin film waveguides*", SPIE, Vol. 2044, p.236-245 (1993).

[10] V. Mizrahi, P. J. Lemaire, T. Erdogan, W. A. Reed, D. J. DiGiovanni, "*Ultraviolet laser fabrication of ultra-strong optical fiber gratings and of germania-doped channel waveguides*", Applied Physics Letters, Vol. 63, No. 13, p.1727-1729 (1993).

[11] C. B. E. Gawith, T. Bhutta, D. P. Shepherd, P. Hua, J. Wang, G. W. Ross, and P. G. R. Smith, "*Buried laser waveguides in neodymium-doped BK-7 by $K^+$-$Na^+$ ion-exchange across a direct-bonded interface*", Applied Physics Letters, Vol. 75, No. 24, p.3757-3759 (1999).

[12] D. Milanese, L. N. Ng, A. Fu, E. R. M. Taylor, C. Contardi, and M. Ferraris, "*UV-written channels in germano borosilicate glasses doped with sodium*", SPIE, Vol. 3620, p.263-265 (1999).

[13] D. Milanese, A. Fu, C. Contardi, E. R. M. Taylor, and M. Ferraris, "*Photosensitivity and directly UV written waveguides in an ion-exchangeable bulk oxide glass*", submitted to Journal of Optical Materials (2000).

[14] G. Perrone, A. Moro, C. Contardi, and D. Milanese, "*Ion exchanged waveguide in new and active and photosensitive glass*", Electronics Letters, Vol. 36, No. 22, p.1845-1846 (2000).

[15] A. M. Glass, "*The photorefractive effect*", Optical Engineering, Vol. 17, No. 5, p.470-479 (1978).

[16] N. V. Kukhtarev, V. B. Markov, S. G. Odulov, M. S. Soskin, and V. L. Vinetskii, "*Holographic storage in electrooptic crystals. I. Steady state*", Ferroelectrics, Vol. 22, p.949-960 (1979).

[17] V. B. Neustruev, "*Colour centres in germanosilicate glass and optical fibres*", Journal of Physics: Condensed Matter, Vol. 6, p.6901-6936 (1994).

[18] R. M. Atkins and R. P. Espindola, "*Photosensitivity and grating writing in hydrogen loaded germanosilicate core optical fibers at 325 and 351 nm*", Applied Physics Letters, Vol. 70, No. 9, p.1068-1069 (1997).

[19] M. V. Bazylenko, M. Gross, and D. Moss, "*Mechanisms of photosensitivity in germanosilica films*", Journal of Applied Physics, Vol. 81, No. 11, p.7497-7505 (1997).

[20] M. Svalgaard, "*Ultraviolet light induced refractive index structures in germanosilica*", Technical University of Denmark, Thesis (1997).

[21] J. Canning, "*Engineering large anisotropy in amorphous glass*", Optics Letters, Vol. 25, No. 4, p.233-235 (2000).

[22] D. L. Griscom, "*Defect structure of glasses. Some outstanding questions in regard to vitreous silica*", Journal of Noncrystalline solids, Vol. 73, p.51-77 (1985).

[23] G. Pacchioni and G. Ierano, "*Ab initio theory of optical transitions of point defects in $SiO_2$*", Physical Review B, Vol. 57, No. 2, p.818-832 (1998).

[24] T. Uchino, M. Takahashi, and T. Yoko, "*E' centers in amorphous $SiO_2$ revisited: a new look at an old problem*", Physical Review Letters, Vol. 86, No. 24, p.5522-5525 (2001).

[25] M. Svalgaard and M. Kristensen, "*Direct writing of planar waveguide devices using ultraviolet light*", Photonics, BTuB2-1 / 27 (1994).

[26] M. Svalgaard and M. Kristensen, "*Directly UV written silica-on-silicon planar waveguides with low loss*", Electronics Letters, Vol. 33, No. 10, p.861-863 (1997).

[27] M. Svalgaard, "*Direct writing of planar waveguide power splitters and directional couplers using a focussed ultraviolet beam*", Electronics Letters, Vol. 33, No. 20, p.1694-1695 (1997).

[28] D. Zauner, K. Kulstad, J. Rathje, and M. Svalgaard, "*Directly UV-written silica-on-silicon planar waveguides with low insertion loss*", Electronics Letters, Vol. 34, No. 16, p.1582-1584 (1998).

[29] M. Svalgaard, "*Effect of $D_2$ outdiffusion on direct UV writing of optical waveguides*", Electronics Letters, Vol. 35, No. 21, p.1840-1842 (1999).

[30] M. Svalgaard, "*Optical waveguides and gratings made by UV-photogeneration*", ECIO, p.333-338 (1999).

[31] G. D. Maxwell and B. J. Ainslie, "*Demonstration of a directly written directional coupler using UV-induced photosensitivity in a planar silica waveguide*", Electronics Letters, Vol. 31, No. 2, p.95-96 (1995).

[32] D. W. J. Harwood, A. Fu, E. R. Taylor, R. C. Moore, Y. D. West, and D. N. Payne, "*A 1317nm neodymium doped fluoride glass waveguide laser*", ECOC, 6.4.8 (2000).

[33] A. K. Mairaj, A. Fu, H. N. Rutt, and D. W. Hewak, "*Optical channel waveguide in chalcogenide (Ga:La:S) glass*", submitted to Electronics Letters (2001).

[34] J. Haisma, G. A. C. M. Spierings, U. K. P. Biermann, and A. A. van Gorkum, "*Diversity and feasibility of direct bonding: a survey of a dedicated optical technology*", Applied Optics, Vol. 33, No. 7, p.1154-1169 (1994).

[35] A. Plößl and G. Kräuter, "*Wafer direct bonding: tailoring adhesion between brittle materials*", Materials Science and Engineering, Vol. R25, No. 1-2, p.1-88 (1999).

[36] C. Ciminelli, A. D'Orazio, M. De Sario, C. Geradi, V. Petruzzelli, and Francesco Prudenzano, "*Effects of thermal annealing on the optical characteristics of $K^+$-$Na^+$ waveguides*", Vol. 37, No. 9, p.2346-2356 (1998).

[37] D. W. Tenquist, R. M. Whittle, and J. Yarwood, "*University Optics*" Volume 1, Iliffe (1969).

[38] G. A. C. M. Spierings, J. Haisma, and T. M. Michelsen, "*Surface-related phenomena in the direct bonding of silicon and fused-silica wafer pairs*", Philips Journal of Research, Vol. 49, p.47-63 (1995).

[39] J. Haisma, G. A. C. M. Spierings, T. L. Michielsen, and C. L. Adema, "*Surface preparation and phenomenological aspects of direct bonding*", Philips Journal of Research, Vol. 49, p.23-46 (1995).

[40] J. Canning, D. Moss, M. Aslund, and M. Bazylenko, "*Negative index gratings in germanosilicate planar waveguides*", Electronics Letters, Vol. 34, No. 4, p.366-367 (1998).

[41] E. K. Mwarania, "*Planar ion-exchanged waveguide lasers in glass*", University of Southampton, Thesis (1992).

[42] T. A. Strasser, T. Erdogan, A. E. White, V. Mizrahi, and P. J. Lemaire, "*Ultraviolet laser fabrication of strong, nearly polarization-independent Bragg reflectors in germanium-doped silica waveguides on silica substrates*", Applied Physics Letters, Vol. 65, No. 26, p.3308-3310 (1994).

[43] W. P. Risk, "*Modeling of longitudinally pumped solid-state lasers exhibiting reabsorption losses*", Journal of the Optical Society of America B, Vol. 5, No. 7, p.1412-1423 (1988).

[44] D. Findlay and R. A. Clay, "*The measurement of internal losses in 4-level lasers*", Physics Letters, Vol. 20, No. 3, p.277-278 (1966).

# Chapter 7
# CONCLUSIONS

## 7.1 Direct bonding

The future of direct bonding seems promising. Initial forays into this relatively unexplored technique for waveguide design and fabrication have provided interesting results in both crystalline and amorphous materials, confirming the versatility of the technique and inspiring several directions for further research. As a fabrication technique for contacting optically flat substrate layers across a low-loss interface, direct bonding has proved repeatedly successful and readily reproducible in a number of materials, with minor alterations to the basic technique giving enhanced results for different bonding configurations (the pyroelectric effect inherent to ferroelectric crystals is used to improve contact between bonding layers for example) and structures (such as the application of controlled annealing to promote intersubstrate diffusion). With uniform bonded areas of as large as 5 cm × 3 cm prepared within the scope of this research, and interfacial strength sufficient to withstand dicing and thinning of a bonded layer to ten microns (or less), subsequent devices based on this technology have demonstrated high operational efficiencies and low propagation losses, indicating a strong potential for use in integrated optical devices and structures. With several novel active waveguide devices produced to date [1-4], based on a range of existing and innovative technologies, future projects are likely to be dominated by the development of these structures into more complex channel waveguides and direct-bonded configurations, as described in the following sections.

## 7.2 Waveguide structures in periodically-poled lithium niobate

The direct-bonded planar waveguide structure of PPLN buried in lithium tantalate described in Chapter 3 demonstrates a significant improvement over similar devices in the bulk material. From initial tests (performed without an optimum optical launch arrangement) an increase in second-harmonic-generation conversion efficiency of almost 40 % over the bulk has been obtained, indicating that even greater efficiencies could be available with some optimisation of the waveguide geometry and optical focussing techniques. From Equation 3.4, it is apparent that the first stage in improving the efficiency of a direct-bonded buried PPLN waveguide device is to

increase the crystal length and waveguide geometry in which the nonlinear process takes place [5]. As such, the creation of long channel waveguide devices in PPLN substrates is a fundamental step towards improving the efficiency of nonlinear processes in this material [6].

Several techniques for creating channel confinement in direct-bonded PPLN waveguides are proposed for future work, and begin with the development of existing results. Based on the transverse confinement observed within the original buried PPLN waveguide device (an effect evident in the changed transmission and modal properties between poled and unpoled regions of the lithium niobate waveguide), it is hoped that thin PPLN gratings will exhibit channel waveguide behaviour when buried in lithium tantalate by direct bonding methods (Figure 7.1).

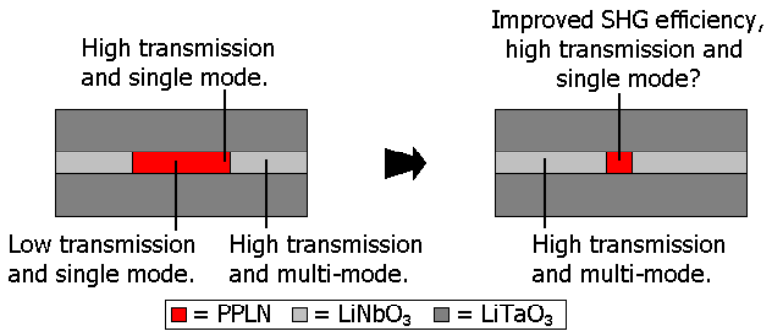


**Figure 7.1**: A proposed path towards creating channel waveguides in buried PPLN structures based upon results from previous direct-bonding experiments (Chapter 3).

Diffusion of magnesium oxide [7] or titanium [8] into PPLN substrates is a second approach towards creating transverse optical confinement in this material. The first of these processes uses the reduction of refractive index caused by magnesium oxide diffusion into lithium niobate to surround a core region of undoped material with $MgO:LiNbO_3$, creating a change in refractive index suitable for transverse confinement. Burying the doped layer in lithium tantalate would then complete the channel waveguide structure (Figure 7.2). Conversely, titanium indiffusion increases the refractive index of PPLN and can be diffused as a distinct channel along the crystal substrate before adding a lithium niobate cladding layer (Figure 7.3). This method could also be used to direct bond a titanium indiffused (unpoled) lithium niobate substrate to a cladding layer of lithium niobate, before using the room temperature electric field poling technique to create periodic domain inversion across

the entire direct-bonded arrangement. Such diversity means that diffusion processes could provide a useful array of channel waveguide fabrication techniques.

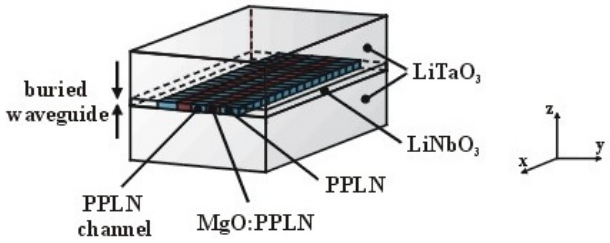


**Figure 7.2**: Proposed structure for a buried PPLN channel waveguide. Magnesium oxide is diffused into the bulk lithium niobate substrate prior to bonding, reducing refractive index to give horizontal optical confinement. Precision polishing techniques are then used to bury a selected region of the periodically poled substrate.

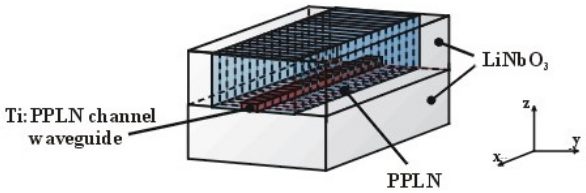


**Figure 7.3**: Proposed structure for a buried PPLN channel waveguide. Here, titanium indiffusion (used to create a channel of raised refractive index for optical confinement) and periodic poling of the top layer is performed prior to direct bonding. An alternative approach is to direct bond a titanium indiffused (unpoled) lithium niobate substrate to a second, similarly oriented, lithium niobate substrate and periodically pole the entire arrangement.

### 7.3 Etched structures in lithium niobate

As an addition to the devices and experiments described in Chapters 3 to 6, the direct bonding work performed within the scope of this project also includes a collaboration with Ian Barry, Collin Sones, and Prof. Robert Eason of the University of Southampton, into the fabrication of three-dimensional ridge structures in direct-bonded selectively-domain-inverted lithium niobate [9-11]. Previous experiments performed by Barry et al. [9], utilised the differential etching rates of the +z and -z domain orientations of lithium niobate to create raised ridges of crystal material in partially domain-inverted substrates. The basis of this process was a $HF:HNO_3$ treatment which etched exposed -z regions of domain-inverted lithium niobate while leaving the surrounding +z surfaces relatively unscathed (exposed -z surfaces on the reverse side of the poled sample were also etched away). However, while ridges created by this method feature extremely smooth (< 5 nm roughness), near-vertical walls, they also remain surrounded by rough areas of etched substrate material.

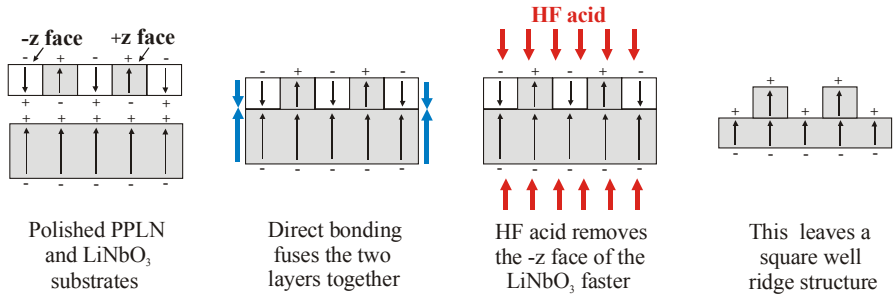


**Figure 7.4**: The etching process used to create 3D ridge structures in a partially-domain-inverted $LiNbO_3$ substrate direct-bonded to a single-domain $LiNbO_3$ crystal.

The application of direct bonding to this process has been to provide an etch-stop boundary at the +z surface of the poled sample, as illustrated in Figure 7.4. By direct bonding the (predominantly) +z faces of two samples together, an optically flat etch-resistant surface is brought into atomic contact with the poled sample, preventing the removal of -z material beyond this boundary. It has been proposed [10-11] that the combination of this process with the well-established techniques of photolithography and precision polishing could lead to the creation of intricate three-dimensional structures of lithium niobate mounted upon lithium niobate substrates.

As an initial demonstration of this technique, three pairs of crystals were direct-bonded for etching experiments, to be performed by Ian Barry, and provided two distinctly different results. The first two etched samples provided the expected etch-stop boundary, to which several smooth-walled ridges are bonded, and the results of which are shown in Figure 7.5. As illustrated by the SEM photography, the etched ridge structures are well defined, and possible applications of this technique include 3D device engineering, channel waveguide structures, and optical fibre butt-coupling alignment [9]. However, an unexpected result was obtained from the last etched sample, which included unbonded gaps at several points across the interface (possibly resulting from a pre-poling acid-etch treatment or residual dirt between the sample interfaces) and allowed the final stages of etching to circumvent the etch-stop and attack the reverse side of some ridges. When the sample was cleaved (to allow inspection of the etched structures from the side) several protruding ridges of lithium niobate were exposed, an example of which is given in Figure 7.6. This unusual result has subsequently formed the basis of a new research project undertaken by Collin Sones [11] at the Optoelectronics Research Centre who is developing the

possibility of applying shaped electrodes to the anchored end of the $LiNbO_3$ protrusions as the basis for a piezoelectric waveguide-based switch.

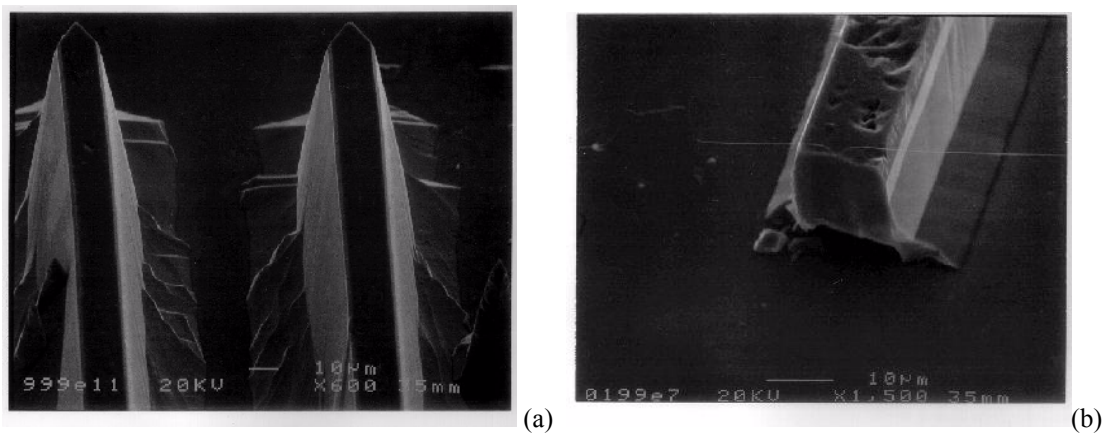


(a) (b)

**Figure 7.5**: Acid etched ridges of lithium niobate with a smooth etch-stop boundary provided by direct bonding. Figure 7.3(a) shows two ~ 60-μm-high ridges of lithium niobate on a dark lithium niobate background. Figure 7.3(b) shows the end of a ~ 20-μm-high ridge fabricated on a separate lithium niobate substrate.

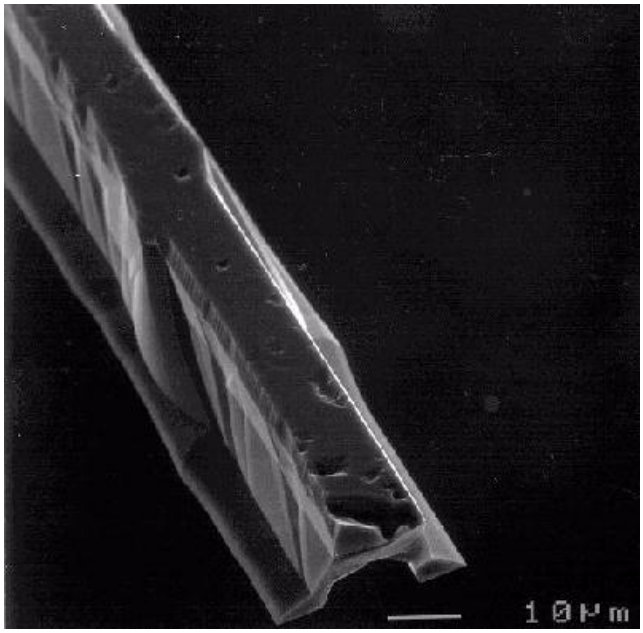


**Figure 7.6**: SEM image of an etched lithium niobate bridge protruding from a lithium niobate substrate.

## 7.4 Photorefractive waveguide devices

The direct-bonded structure of $Fe:LiNbO_3$ buried in $MgO:LiNbO_3$ described in Chapter 4 shows considerable improvement in optical limiting experiments over the bulk and earlier waveguide devices in this material [12]. However, expanding the current planar structure towards channel waveguide confinement in non-degraded

material is an essential step if the deleterious effects of beam divergence and intersubstrate ion-exchange, which reduce the attainable $\Delta OD$ and increase the input intensity required for a fast photorefractive response, are to be overcome. While an immediate solution to this problem would be to optimise the existing three-layered structure towards a two-dimensional waveguide format, perhaps with undoped cladding layers to help minimise depletion of the iron-doped core during annealing, the tolerances involved in isolating a < 20-μm core would make fabrication *extremely* challenging. Instead, a proposed alternative is to achieve a localised change in refractive index at the surface of an Fe:$LiNbO_3$ substrate prior to the addition of a direct-bonded cladding layer. For example, titanium-indiffusion is a well-established means of producing channel waveguides in $LiNbO_3$, which can exhibit losses of less than 1 dB $cm^{-1}$ and photorefractivity suitable for holographic processes [13-14]. An ideal solution therefore, would be to bury a titanium-indiffused Fe:$LiNbO_3$ channel waveguide with a direct-bonded cladding layer of Fe:$LiNbO_3$ (Figure 7.7) providing buried channel confinement with low losses and no reduction in photorefractivity for a highly efficient optical limiting device. Such technology could also be extended towards dense multi-layered waveguide arrays for use in spatially coherent bundles, allowing ordinary scenes to be relay imaged through a larger device in which optical limiting would only occur in those regions at the focus of an incident beam.

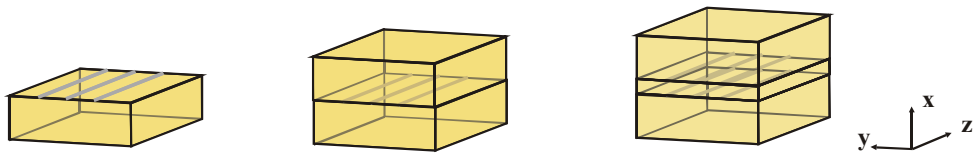


a) Ti:Fe:$LiNbO_3$ b) Ti:Fe:$LiNbO_3$ - Fe:$LiNbO_3$ c) Ti:Fe:$LiNbO_3$ - Ti:Fe:$LiNbO_3$ - Fe:$LiNbO_3$

**Figure 7.7:** Schematic diagrams of various waveguiding structures in titanium-indiffused Fe:$LiNbO_3$, from a) channel waveguides to b) buried channel waveguides and c) dense multilayered waveguide arrays, for optical limiting applications.

## 7.5 Intersubstrate ion-exchange and direct UV writing

The low-loss single-mode buried channel waveguide devices described in Chapter 6 demonstrate a significant step towards complex integrated optical devices in direct-bonded glass. Also demonstrated is a distinct improvement over the preceding devices [2,15], providing previously unattained single-mode channel waveguide confinement in an intersubstrate ion-exchanged layer and low propagation losses in a

direct-UV-written SGBN-based glass. Based on these promising results, a viable route forward for this multi-fabricational project would be to push both the techniques of direct-bonding and direct-UV-writing one step further, creating a more complex combination of substrate and structure. Following recent developments in hybrid glass substrate bonding, a technique presented by Schott Glass Technologies earlier this year (based on phosphate glasses for ion-exchange) [16], distinct regions of erbium-doped and ytterbium-doped SGBN material could be direct-bonded together to form a single sample for direct UV writing, into which an intersubstrate ion-exchanged layer could be formed (Figure 7.8).

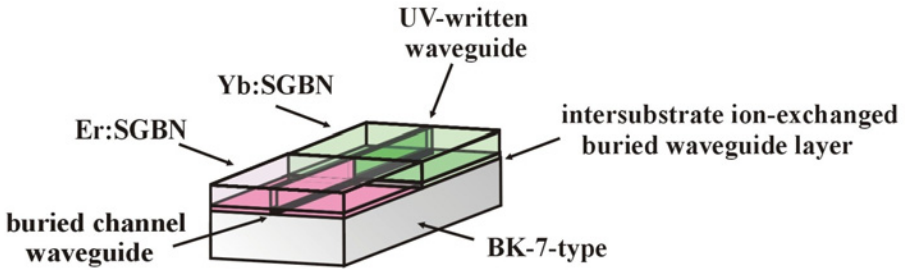


**Figure 7.8:** Proposed structure for a hybrid-glass buried channel waveguide laser by the combined processes of direct bonding and direct-UV-writing.

While complex, this approach would allow the fabrication of a low-loss buried photosensitive hybrid glass waveguide layer into which dense channel waveguides with long path lengths could be fabricated and individually optimised for laser action in each rare-earth doped section. As suggested by Daniel Milanese, the potential to incorporate UV-written Bragg-grating-based reflectors [17] to act as laser mirrors, an innovation not available in non-photosensitive substrates designed for ion-exchange techniques alone, could also prove a viable route towards reducing the associated butt-mounting mirror loss.

## REFERENCES

[1] C. B. E. Gawith, D. P. Shepherd, J. A. Abernethy, D. C. Hanna, G. W. Ross, and P. G. R. Smith, "*Second-harmonic generation in a direct-bonded periodically poled $LiNbO_3$ buried waveguide*", Optics Letters, Vol. 24, No. 7, p.481-483 (1999).

[2] C. B. E. Gawith, T. Bhutta, P.Hua, J. Wang, D. P. Shepherd, G. W. Ross, and P. G. R. Smith, "*Buried laser waveguides in neodymium doped BK-7 by $K^+$-$Na^+$ ion-exchange across a direct-bonded interface*", Applied Physics Letters, Vol. 75, No. 24, p.3757-3759 (1999).

[3] C. B. E. Gawith, P. Hua, P. G. R. Smith, and G. Cook, "*Nonreciprocal transmission in a direct-bonded photorefractive Fe:$LiNbO_3$ buried waveguide*", Applied Physics Letters, Vol. 78, No. 26, p.4106-4108 (2001).

[4] C. B. E. Gawith, A. Fu, T. Bhutta, P. Hua, J. Wang, E. B. M. Taylor, D. P. Shepherd, P. G. R. Smith, D. Milanese, and M. Ferraris, "*Direct-UV-written single-mode buried laser channel waveguides in direct-bonded intersubstrate ion-exchanged Nd:SGBN glass*", submitted to Applied Physics Letters.

[5] P. G. Harper and B. S. Wherret, "*Nonlinear optics*", Scottish Universities Summer School in Physics 16th, Heriot-Watt University (1975).

[6] M. Houe and P. D. Townsend, "*An introduction to methods of periodic poling for second-harmonic generation*", Journal of Physics D: Applied Physics, Vol. 28, p.1747-1763 (1995).

[7] K. Komatsu, S. Yamazaki, M. Kondo, and Yoshinori Ohta, "*Low-loss broad-band $LiNbO_3$ guided-wave phase modulators using titanium / magnesium double diffusion method*", Journal of Lightwave Technology, Vol. LT-5, No. 9, p.1239-1245 (1987).

[8] J. Amin, V. Pruneri, J. Webjörn, P. St. J. Russell, D. C. Hanna, and J. S. Wilkinson, "*Blue light generation in a periodically poled $Ti:LiNbO_3$ channel waveguide*", Optics Communications, Vol. 135, p.41-44 (1997).

[9] I. E. Barry, G. W. Ross, P. G. R. Smith, and R. W. Eason, "*Ridge waveguides in lithium niobate fabricated by differential etching following spatially selective domain inversion*", Applied Physics Letters, Vol. 74, No. 10, p.1487-1488 (1999).

[10] R. W. Eason, I. E. Barry, G. W. Ross, P. G. R. Smith, and C. B. E. Gawith, "*Microstructuring in $LiNbO_3$: a route to MEMS devices in piezoelectric crystal media*", ISAP 2000 / Micro-Opto-Electro-Mechanical Systems, Glasgow (2000).

[11] C. Sones, S. Mailis, V. Apostolopoulos, I. E. Barry, C. B. E. Gawith, P. G. R. Smith, and R.W.Eason, "*Fabrication of piezoelectric micro-cantilevers in domain engineered $LiNbO_3$ single crystals*", submitted to the Journal of Micromechanics and Microengineering.

[12] G. Cook, J. P. Duignan, L. L. Taylor, and D. C. Jones, "*Developing photorefractive fibres for optical limiting*", SPIE, Vol. 4106, p.230-244 (1999).

[13] J. Hukreide, D. Kip, and E. Krätzig, "*Investigation of titanium- and copper-indiffused channel waveguides in lithium niobate and their application as holographic filters for infrared light*", Journal of Optics A: Pure and Applied Optics, Vol. 2, p.481-487 (2000).

[14] J. C. Chon, W. Feng, and A. R. Mickelson, "*Photorefractive damage thresholds in $Ti:LiNbO_3$ channel waveguides*", Applied Optics, Vol. 32, No. 36, p.7572-7580 (1993).

[15] D. Milanese, A. Fu, C. Contardi, E. R. M. Taylor, and M. Ferraris, "*Photosensitivity and directly UV written waveguides in an ion-exchangeable bulk oxide glass*", submitted to Journal of Optical Materials (2000).

[16] S. D. Conzone, J. S. Hayden, D. S. Funk, A. Roshko, and D. L. Veasey, "*Hybrid glass substrates for waveguide device manufacture*", Optics Letters, Vol. 26, No. 8, p.509-511 (2001).

[17] C. Montero, C. Gomez-Reino, and J. L. Brebner, "*Planar Bragg gratings made by excimer-laser modification of ion-exchanged waveguides*", Optics Letters, Vol. 24, No. 21, p.1487-1489 (1999).

## Appendix A
## DIFFUSION MODELLING

The diffusion characteristics of potassium ions in an intersubstrate ion-exchange process can been approximated for two direct-bonded glasses featuring chemical compositions similar to the devices described Chapter 5.

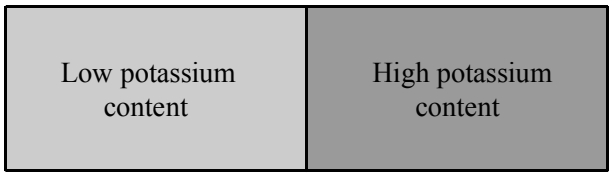


**Figure A.1**: A simple model of potassium diffusion between two glass layers assuming semi-infinite sources of material.

In this model the two glass layers of a buried laser waveguide device are represented as semi-infinite sources of cations for ion-exchange, as illustrated in Figure A.1. Using a solution of Fick's second law [1], the concentration of potassium at a selected position across the sample interface can be related to diffusion time by the equation [1]:

$$C = \left(\frac{C_1 + C_2}{2}\right) - \left(\frac{C_1 - C_2}{2}\right) \mathrm{erf}\left(\frac{x}{2\sqrt{D_e t}}\right) \qquad \text{(A.1)}$$

where $C_1$ and $C_2$ are the potassium concentrations of each glass layer (12 % and 6 % respectively), $x$ is the distance across the sample interface (the direct-bonded interface is assumed to be at $x$ = 0), and t is the diffusion time in seconds. The value used for $D_e$, the effective diffusion coefficient of potassium in BK-7 glass, is dependent on ion-exchange temperature and has been approximated as $1.42\times10^{-15}$ $m^2$ $s^{-1}$ (for six hours of $K^+$-$Na^+$ ion-exchange at 350 °C in a BK-7 glass substrate) from previous publications [2]. The error function of Equation A.1 is determined by [1]:

$$\mathrm{erf}(z) = \frac{2}{\sqrt{\pi}} \int_0^z e^{-y^2}\, dy = \frac{2}{\sqrt{\pi}} \left[ -\frac{1}{2} e^{-y^2} \right]_0^z \qquad \text{(A.2).}$$

The subsequent graph of theoretical potassium concentration versus distance across the direct-bonded interface of an intersubstrate ion-exchanged buried laser waveguide is given in Figure A.2.

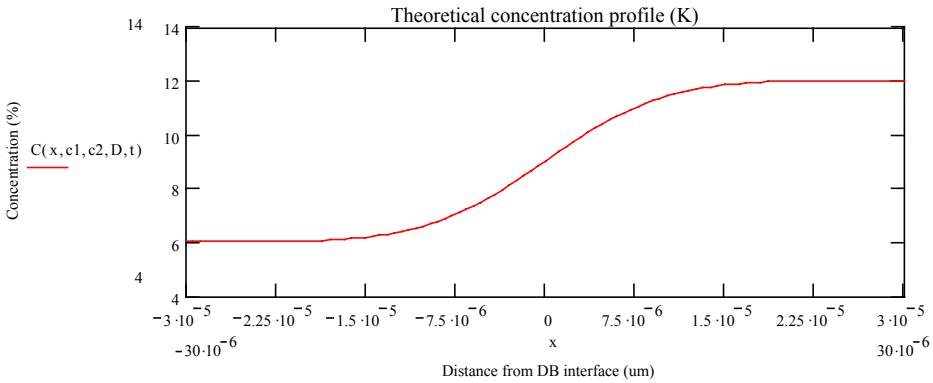


**Figure A.2**: Theoretical diffusion profile for potassium across the interface (x = 0) of a neodymium-doped BK-7 to BK-7-type direct-bonded sample. Simulated for 6 hours of diffusion at 350 °C.

As mentioned in the Chapter 5, it is necessary to perform a mathematical deconvolution of the compositional profile presented in Figure 5.4 before the results can be compared with the theoretical model. Here, the 5 μm resolution offered by the SEM for potassium and sodium compositional analysis, which is defined by the size of the electron beam probe, is approximated by a gaussian function with a full-width-half-maximum (FWHM) of 5 μm. This is initially applied to our data to synthesise resolution error on the potassium step function expected between the two glass layers of an unannealed direct-bonded sample. Applying potassium concentrations either side of the bonded interface as boundary conditions, multiple gaussian functions are then multiplied by this step function at different points across its width, as shown in Figure A.3. This simulates the scanning of an electron beam across the sample. Integrating each result gained by this method gives a theoretical representation of SEM error for a line-scan compositional analysis, a graph of which is plotted in Figure A.4.

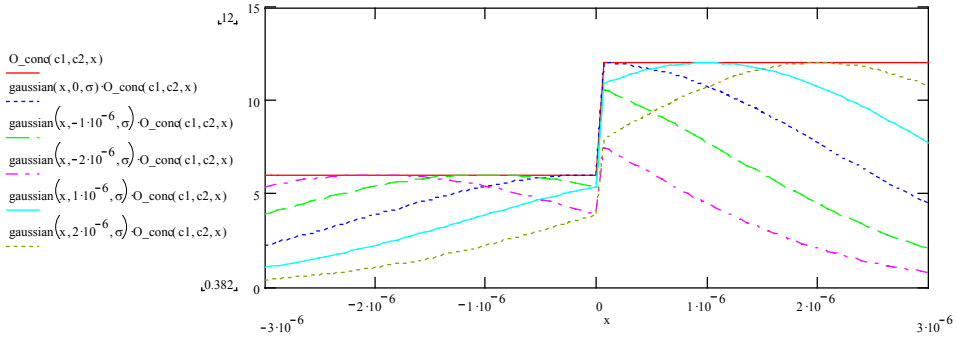


**Figure A.3**: The result of multiplying gaussian functions by a step function at several intervals along its length. To simulate resolution error in a line scan compositional analysis, many gaussian functions are integrated along the length of the step function.

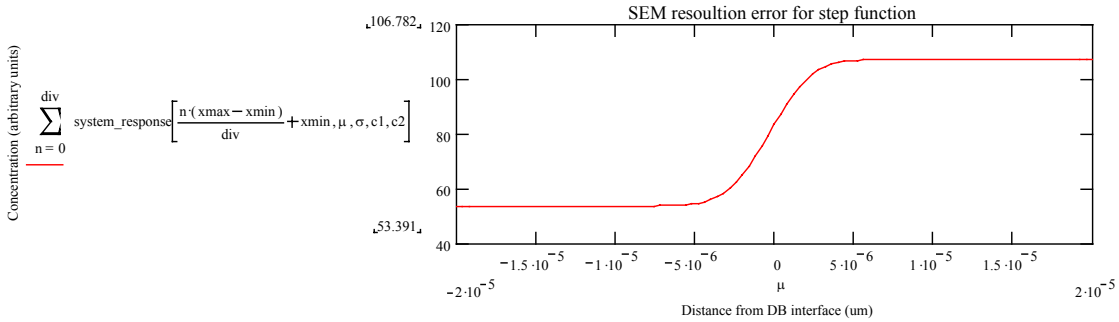


**Figure A.4**: Theoretical profile of resolution error for SEM compositional analysis. This model is based on a step function of potassium concentration between the two layers of an unannealed sample.

This result compares well with the potassium profile measured by the SEM for an unannealed sample (Figure 5.4), featuring a total range of diffusion of around 15 μm. Figure A.5 illustrates the effect of applying this model of SEM resolution error to the predicted diffusion profile of Equation A.1. As can be seen from the graph, the difference between the two curves is minimal, with both results comparing well to the approximate 40-μm range of diffusion presented in Figure 5.4. It is therefore suggested that Equation A.1 will give a good approximation for the diffusion characteristics of $K^+$-$Na^+$ intersubstrate ion-exchange after prolonged temperature treatment, although alternate measurement techniques (such as SIMS) should be used for unannealed samples.

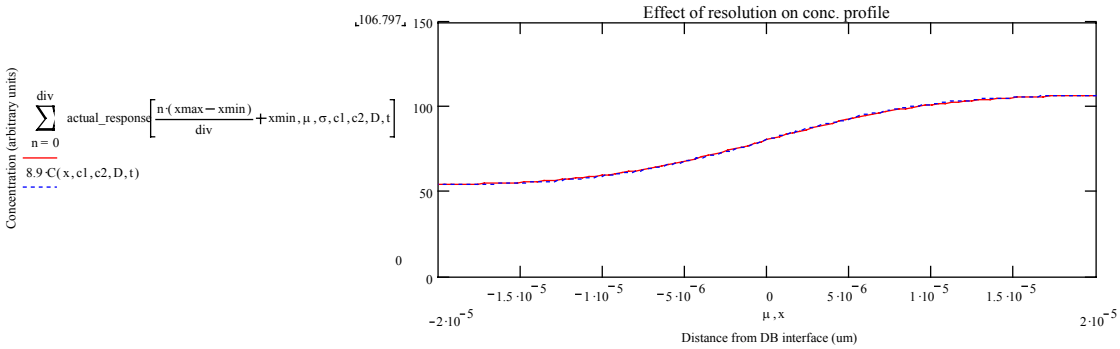


**Figure A.5**: Theoretical concentration profile of potassium diffusion between glass layers with 6 % and 12 % of potassium respectively, plotted with and without simulated SEM resolution error (the two plots are overlayed).

## REFERENCES

[1] J. Crank, "*The mathematics of diffusion*" 2nd Ed., Oxford Science Publications (1997).

[2] G. L. Yip and J. Albert, "*Characterisation of planar optical waveguides by $K^+$-ion exchange in glass*", Optics Letters, Vol. 10, No. 3, p.151-153 (1985).

## Appendix B

## PUBLICATIONS

### Journal publications

The publications listed below regard the work described in this thesis. Copies of published journal papers are included after these pages.


[1] C. B. E. Gawith, D. P. Shepherd, J. A. Abernethy, D. C. Hanna, G. W. Ross, and P. G. R. Smith, "*Second-harmonic generation in a direct-bonded periodically poled $LiNbO_3$ buried waveguide*", Optics Letters, Vol. 24, No. 7, p.481-483 (1999).

[Also see the related newsbreak, "*Periodically poled lithium niobate buried waveguide doubles output frequency*", Laser Focus World, Vol. 35, No. 5, p.9 (1999)].

[2] C. B. E. Gawith, T. Bhutta, P.Hua, J. Wang, D. P. Shepherd, G. W. Ross, and P. G. R. Smith, "*Buried laser waveguides in neodymium doped BK-7 by $K^+$-$Na^+$ ion-exchange across a direct-bonded interface*", Applied Physics Letters, Vol. 75, No. 24, p.3757-3759 (1999).

[3] C. B. E. Gawith, P. Hua, P. G. R. Smith, and G. Cook, "*Nonreciprocal transmission in a direct-bonded photorefractive Fe:$LiNbO_3$ buried waveguide*", Applied Physics Letters, Vol. 78, No. 26, p.4106-4108 (2001).

[4] C. B. E. Gawith, A. Fu, T. Bhutta, P. Hua, J. Wang, E. B. M. Taylor, D. P. Shepherd, P. G. R. Smith, D. Milanese, and M. Ferraris, "*Direct-UV-written single-mode buried laser channel waveguides in direct-bonded intersubstrate ion-exchanged Nd:SGBN glass*", submitted to Applied Physics Letters (2002).


### International meetings


[5] C. B. E. Gawith, D. P. Shepherd, J. A. Abernethy, D. C. Hanna, G. W. Ross, and P. G. R. Smith, "*Efficient second-harmonic generation in a directly-bonded, buried, PPLN planar waveguide*", CLEO/EUROPE-EQEC'98 Glasgow, Post Deadline Papers CPD2.7 (1998).

[6] C. B. E. Gawith, T. Bhutta, D. P. Shepherd, P. Hua, G. W. Ross, P. G. R. Smith, and J. Wang, "*Ion-exchange across a direct-bonded interface*", CLEO 2000 San Francisco, CWK37 (2000).

[7] C. B. E. Gawith, P. Hua, P. G. R. Smith, and G. Cook, "*Nonreciprocal transmission in a direct-bonded photorefractive Fe:$LiNbO_3$ waveguide buried in MgO:$LiNbO_3$*", CLEO Pacific Rim Japan, 1313 (2001).

[8] C. B. E. Gawith, A. Fu, T. Bhutta, D. P. Shepherd, E. R. Taylor, P. G. R. Smith, D. Milanese, and M. Ferraris, "*Single-mode UV-written buried channel waveguide lasers in direct-bonded neodymium-doped SGBN*", accepted for presentation at CLEO 2002 California, CTuK53 (2002).

**Other publications to stem from the direct bonding and fabrication processes outlined in this thesis**


[9] R. W. Eason, I. E. Barry, G. W. Ross, P. G. R. Smith, and C. B. E. Gawith, "*Microstructuring in $LiNbO_3$: a route to MEMS devices in piezoelectric crystal media*", ISAP 2000 / Micro-Opto-Electro-Mechanical Systems, Glasgow (2000).

[10] P. G. R. Smith, C. B. E. Gawith, J. A. Abernethy, R. W. Eason, I. E. Barry, S. Mailis, N. G. R. Broderick, D. J. Richardson, D. C. Hanna, "*Material aspects of periodically poled lithium niobate*", BACG (British Association for Crystal Growth), Manchester (2000)

[11] P. G. R. Smith, P. E. Britton, D. Taverner, N. G. Broderick, D. J. Richardson, G. W. Ross, C. B. E. Gawith, J. A. Abernethy, H. L. Offerhaus, D. C. Hanna, "*Review of erbium fibre laser based nonlinear optics in periodically poled lithium niobate (PPLN)*", International Workshop on Periodically Microstructured Nonlinear Optical Materials Madrid (2001).

[12] C. Sones, S. Mailis, V. Apostolopoulos, I. E. Barry, C. B. E. Gawith, P. G. R. Smith, and R.W.Eason, "*Fabrication of piezoelectric micro-cantilivers in domain engineered $LiNbO_3$ single crystals*", Journal of Micromechanics and Microengineering, Vol. 12, No. 1, p53-57 (2002).


**Invited talks at other host institutions**


[13] C. B. E. Gawith, "*Ion-exchange across a direct-bonded interface*", Politecnico de Turino, Italy (2000).

[14] C. B. E. Gawith, "*Direct-bonded PPLN waveguide structures*", Tohoku University, Japan (2000).

# Second-harmonic generation in a direct-bonded periodically poled $LiNbO_3$ buried waveguide

**C. B. E. Gawith, D. P. Shepherd, J. A. Abernethy, D. C. Hanna, G. W. Ross, and P. G. R. Smith**

*Optoelectronics Research Centre, University of Southampton, Highfield, Southampton SO17 IBJ, UK*

Received December 8, 1998

We report the fabrication of a 12-$\mu$m-thick periodically poled $LiNbO_3$ planar waveguide buried in $LiTaO_3$ by direct bonding of precision-polished surfaces. Frequency doubling of the 1064-nm output of a cw diode-pumped Nd:YAG laser was performed in a 5.5-mm-long device with a 6.50-$\mu$m-period grating at an elevated temperature of 174 °C. The resultant green second-harmonic output exhibited fundamental-spatial-mode characteristics at a 4.3% $W^{-1}$ conversion efficiency. 

*OCIS codes:* 230.7390, 190.2620, 190.4360, 160.3730.

Periodically poled $LiNbO_3$ (PPLN) combines the important characteristics of a large nonlinear coefficient and noncritical phase-matching capabilities for any wavelength in its transmission range, which makes it an attractive material for nonlinear frequency conversion.[1] The combination of these material characteristics with the optical confinement offered by a waveguide geometry provides a promising route to the realization of various compact nonlinear devices based on harmonic[2] or parametric[3] generation.

The two most common methods for fabricating waveguides in $LiNbO_3$, which also work for PPLN, are annealed proton exchange[4] and Ti indiffusion.[5] These processes modify the crystal near the surface to create regions of higher refractive index for optical confinement. In contrast, direct bonding[6] (DB) is a fabrication technique that uses the Van der Waals forces that are present when one brings two atomically flat bodies near each other to combine layers of different materials to form waveguiding boundaries. Such a bond can be formed irrespective of the lattice constants and the orientation of the materials concerned and involves no deleterious modification[7] of the crystalline microstructure of either material. By bringing surfaces into contact in this way, DB preserves the bulk characteristics of each bonded material.

Some recent experiments investigating the bonding characteristics of PPLN have been directed toward fabricating thick multilayered stacks[8] of the material for a large physical aperture, and thus high-power applications. By contrast, our experiments have been aimed at creating a thin waveguide layer of PPLN and exploiting optical confinement to obtain efficient second-harmonic generation (SHG) even at low pump powers. Our initial attempts have been directed at planar waveguide devices. One can fabricate such a device by bonding PPLN onto a suitable substrate before precision polishing it down to waveguide dimensions, a method that has already been demonstrated in the production of $LiNbO_3$ planar waveguides[7,9] for electro-optic applications. One of the primary attractions of this technique is that during the fabrication process, in contrast with the proton-exchange[4] and Ti indiffusion[5] methods, the nonlinearity and domain characteristics of the PPLN structure should remain entirely unchanged from those of the bulk material. A further attraction of the DB method is the extra flexibility that is available when one is designing devices, which offers the possibility of, for example, combinations of multiple layers with different material properties. Such structures have previously been explored in the fabrication of silicon semiconductors (see Ref. 10 and other papers on DB in the same journal issue) and of garnet and glass waveguides for use in lasers,[11] although many areas of exploration remain for DB multilayered optical devices. To this end, in this Letter we describe the fabrication of a symmetrical PPLN waveguide buried in $LiTaO_3$ by DB and precision-polishing methods and the SHG characteristics exhibited by the domain-inverted structure.

Production of the PPLN grating began with a 0.5-mm-thick single-domain $z$-cut $LiNbO_3$ sample of $\sim$15 mm $\times$ 15 mm surface area. A photoresist pattern was created on the $-z$ face of the crystal by photolithography, and domain inversion in the $z$ axis was performed at room temperature by application of a single high-voltage pulse of $\sim$11 kV through liquid electrodes. Application of this pulse resulted in three 5.5-mm-long PPLN gratings positioned in the center of the $LiNbO_3$ sample at 1-mm intervals. Grating periods of 6.58, 6.50, and 6.38 $\mu$m were created, the first two of which are suitable for frequency doubling of a Nd:YAG laser operating at 1064 nm. $LiTaO_3$ was chosen as a suitable material for both the substrate and the cladding layers, as it has a lower refractive index than $LiNbO_3$ and also combines thermal characteristics that are a good match for $LiNbO_3$, an essential prerequisite when one is annealing bonds at high temperatures. The $LiTaO_3$ substrate was 0.5-mm thick and was shaped relative to the PPLN sample, which provided a bonding area of $\sim$12 mm $\times$ 10 mm between the two optically flat surfaces. A mixture of $H_2O_2$–$NH_4OH$–$H_2O$ (1:1:6) was applied to both materials after they were cleaned, followed by several minutes of rinsing in deionized water so that their surfaces could be rendered hydrophilic.[9] The PPLN and the $LiTaO_3$ layers were brought into contact at room temperature, with both samples aligned along

0146-9592/99/070481-03$15.00/0 

the same crystalline orientation. Heat treatment of up to 120 °C immediately followed crystal contact, inducing the pyroelectric effect[8] at the DB interface. The resultant electrostatic attraction forced any excess air or liquid from between the two surfaces, while bringing them close enough to encourage the formation of hydrogen bonds.[12] This effect was demonstrated by the elimination of most of the contact fringes at the crystal interface. Annealing of the bonded sample at 320 °C for 6 h provided a bond strength that was sufficient for further machining, and we then polished down the PPLN region to obtain a waveguiding layer of 12-$\mu$m thickness (with a variance of less than 1 $\mu$m across the entire layer). A further DB cladding layer of $LiTaO_3$ was then added with the same procedure as above. The final DB structure included bonded interfaces of ~12 mm × 10 mm above the below the PPLN core, although the presence of optical fringes provided evidence of small unbonded regions at the edges of the sample. The unwanted material surrounding the gratings was later removed by use of dicing equipment, and the waveguide end faces were then polished to a parallel optical finish. The dimensions of the resulting buried PPLN planar structure are given schematically in Fig. 1.

An upper limit for the value of the propagation loss of the waveguide structure was found by measurement of the transmission of a 1064-nm laser beam when it was end launched into the waveguide. It was noted that the transmission changed between the PPLN and the $LiNbO_3$ (not periodically poled) sections of the waveguide, and the launch condition was therefore optimized individually for each of these regions. Maximum transmission of 81% was found at the edges of the PPLN grating (where the best SHG occurred) and throughout the uniform $LiNbO_3$ sections, whereas 65% transmission was obtained at the center of the PPLN grating. Thus, over the 5.5-mm length of the grating, the upper limit on the propagation loss in each section is found to be 1.7 dB $cm^{-1}$ for the PPLN edges and the $LiNbO_3$ regions and 3.4 dB $cm^{-1}$ for the center of the PPLN grating. In fact, these transmission figures also include launch losses, so the propagation losses are likely to be much lower. Indeed, DB waveguides in garnets and glasses for laser applications have shown losses of ~0.5 dB $cm^{-1}$ or less.[11]

To test the nonlinear properties of the buried PPLN structure we investigated the SHG characteristics of the 6.50-$\mu$m grating. This grating, which occupied the middle section of the PPLN waveguide, was chosen for investigation, as its phase-matching temperature (for 1064-nm doubling) of 174.1 °C suppressed the photorefractive effect. The 1064-nm pump source was a cw diode-pumped Nd:YAG laser operating with multiaxial modes. We rotated the linear polarization state with a half-wave plate so that it was parallel with the $z$ axis of the PPLN to access the material's largest nonlinear coefficient ($d_{33}$). Focusing of the pump radiation for launch into the waveguide was performed with the combination of microscope objective and cylindrical lenses shown in Fig. 2. We passed the initially circular pump beam through a 2.4× cylindrical-lens telescope to expand it in the guided direction before focusing the beam onto the PPLN grating with a 10× microscope objective. Such a combination of optics was chosen to provide good launch efficiency while helping to reduce divergence in the horizontal unguided plane. This choice resulted in a pump source with a line focus and a measured spot size of 4 ± 1 $\mu$m in the guided direction and 11 ± 1 $\mu$m in the nonguided direction. It should be noted that focusing to a waist in the nonguided plane at the input face is not the optimum condition for maximum SHG efficiency[13] and was chosen here for the sake of simplicity. Also, for this initial demonstration both the input and the output end faces of the waveguide were polished but left uncoated, leading to 14% reflection loss at each face.

A second 10× microscope objective was used to collect the transmitted light from the waveguide. This objective was followed by an infrared filter that removed any pump light, and the second-harmonic (SH) power was then measured on a powermeter. For 204 mW of launched pump power ($\lambda = 1064$ nm), a SH power of 1.8 mW ($\lambda = 532$ nm) was generated internal to the crystal. Figure 3 shows a plot of the square root of the SH power versus launched pump power, confirming the expected quadratic dependence.

In the absence of a detailed analysis for SHG in this mixed guided–unguided geometry, we compared the observed efficiency with a calculation of the SH power expected from a similar length of bulk PPLN with optimized focusing in the center of the grating.[13] Assuming a nonlinear coefficient of 16 pm $V^{-1}$ (a value consistent with results in bulk experiments with similarly produced PPLN gratings), an optimized SH output power of 1.3 mW is predicted for the bulk material—a lower result than the 1.8-mW power obtained from the direct-bonded waveguide. This

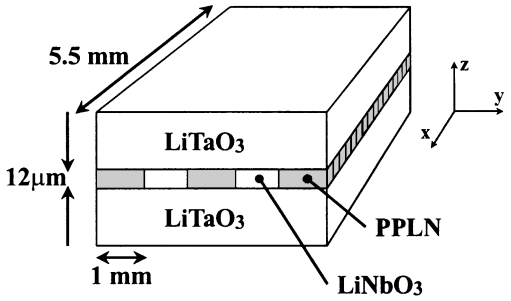


Fig. 1. Schematic end-face diagram of the buried $LiNbO_3$ waveguide, incorporating three PPLN gratings (fabricated before bonding), each 1 mm wide.

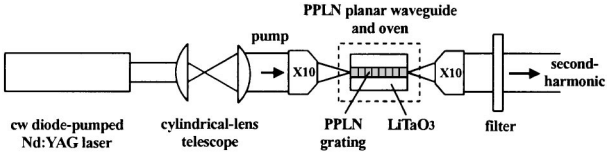


Fig. 2. Experimental arrangement for SHG in the buried PPLN waveguide (side view). A fundamental beam of 1064-nm wavelength was used for frequency-doubling experiments in the 6.5-$\mu$m PPLN grating.

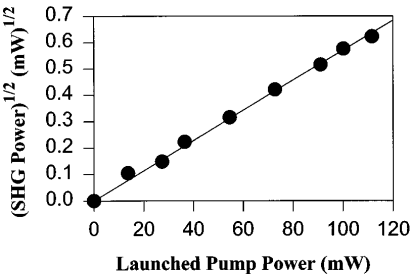


Fig. 3. Dependence of the square root of the generated second-harmonic (532-nm) power on the fundamental infrared (1064-nm) power. The powers are internal to the PPLN.

comparison demonstrates that even with nonoptimum focusing, a short crystal length and only one guided dimension the buried PPLN device shows an improved SHG efficiency of almost 40% over that of the bulk material.

Modal characterization of the output from the PPLN waveguide was performed with a video camera and PC-based evaluation software. It was observed that both the remaining 1064-nm light and the generated SH radiation from the PPLN grating were in the fundamental spatial mode, despite the fact that a 12-$\mu$m-thick waveguide with such a large index difference ($\Delta n_e \approx 1\%$) could be expected to support a number of modes. Indeed, only by using a deliberately poor launch was it possible to excite anything other than the fundamental mode at 1064 nm. At the same time, it was noted that the 1064-nm throughput from the $LiNbO_3$ region within the same buried structure was multispatial mode in nature. This clear difference in the mode properties, combined with the different transmissions described above, suggests that the index profile of the PPLN grating is different from that of the uniform $LiNbO_3$ region. The reason for these unexpected but potentially useful properties has not yet been determined, although they are possibly linked to strain-induced changes in refractive index that we noted in other DB experiments. It is hoped that researchers can exploit this effect to provide a simple route to creating channel waveguides in a DB structure.

In conclusion, we have reported the successful fabrication through direct bonding of a 12-$\mu$m-thick 5.5-mm-long symmetrical PPLN waveguide buried in $LiTaO_3$. Using a 6.50-$\mu$m-period PPLN grating at an elevated temperature of 174 °C, we have demonstrated efficient quasi-phase-matched frequency doubling of the 1064-nm line of a cw diode-pumped Nd:YAG laser. For 204 mW of fundamental pump power, nearly 2 mW of green power was generated at an output wavelength of 532 nm. This result, obtained with nonoptimum focusing conditions, provides a SHG output almost 40% greater than the theoretical expectation for a similar length of bulk material. The waveguiding properties were shown to be different in the PPLN and the uniform $LiNbO_3$ regions of the sample, with the PPLN grating showing surprisingly robust single-spatial-mode behavior. These results suggest that the production of longer buried waveguides, potentially incorporating channel structures, could lead to highly efficient nonlinear devices. The ability to work with thin samples may allow shorter periods to be fabricated effectively, thus extending SHG to shorter blue wavelengths.[14] More generally, the DB technique offers promise in providing extra degrees of design freedom for nonlinear waveguiding devices.

The Optoelectronics Research Centre is an interdisciplinary research center supported by the Engineering and Physical Sciences Research Council (EPSRC). C. Gawith and J. Abernethy acknowledge studentships from the EPSRC. The authors thank Ping Hua for her advice and technical support during sample polishing. C. B. E. Gawith's e-mail address is cbeg@orc.soton.ac.uk.

## References

1. M. M. Fejer, G. A. Magel, D. H. Jundt, and R. L. Byer, IEEE J. Quantum Electron. **28,** 2631 (1992).
2. K. Kintaka, M. Fujimura, T. Suhara, and H. Nishihara, J. Lightwave Technol. **14,** 462 (1996).
3. M. A. Arbore and M. M. Fejer, Opt. Lett. **22,** 151 (1997).
4. P. Baldi, M. P. De Micheli, K. E. Hadi, S. Nouh, A. C. Cino, P. Aschieri, and D. B. Ostrowsky, Opt. Eng. **37,** 1193 (1998).
5. J. Amin, V. Pruneri, J. Webjorn, P. St. J. Russell, D. C. Hanna, and J. S. Wilkinson, Opt. Commun. **135,** 41 (1997).
6. J. Haisma, B. A. C. M. Spierings, U. K. P. Biermann, and A. A. van Gorkum, Appl. Opt. **33,** 1154 (1994).
7. K. Eda, M. Sugimoto, and Y. Tomita, Appl. Phys. Lett. **66,** 827 (1994).
8. M. J. Missey, V. Dominic, L. E. Myers, and R. C. Eckardt, Opt. Lett. **23,** 664 (1998).
9. Y. Tomita, M. Sugimoto, and K. Eda, Appl. Phys. Lett. **66,** 1484 (1995).
10. J. Haisma, T. M. Michielsen, and F. J. H. M. van der Kruis, Phillips J. Res. **49,** 65 (1995).
11. C. T. A. Brown, C. L. Bonner, T. J. Warburton, D. P. Shepherd, A. C. Tropper, D. C. Hanna, and H. E. Meissner, Appl. Phys. Lett. **71,** 1139 (1997).
12. G. A. C. M. Spierings, J. Haisma, and T. M. Michielsen, Philips J. Res. **49,** 47 (1995).
13. G. D. Boyd and D. G. Kleinmann, J. Appl. Phys. **39,** 3597 (1968).
14. G. W. Ross, M. Pollnau, P. G. R. Smith, W. A. Clarkson, P. E. Britton, and D. C. Hanna, Opt. Lett. **23,** 171 (1998).

# Buried laser waveguides in neodymium-doped BK-7 by $K^+$–$Na^+$ ion-exchange across a direct-bonded interface

Corin B. E. Gawith,[a] Tajamal Bhutta, David P. Shepherd, Ping Hua, Ji Wang, Graeme W. Ross, and Peter G. R. Smith
*Optoelectronics Research Centre, University of Southampton, Southampton S017 1BJ, United Kingdom*

(Received 3 August 1999; accepted for publication 20 October 1999)

We report a technique for producing single-step buried $K^+$–$Na^+$ ion-exchanged waveguide lasers in neodymium doped BK-7. Direct bonding is the basis for this process, providing atomic contact between two chemically modified BK-7-type substrates followed by a 350 °C treatment suitable for simultaneous annealing and intersubstrate ion exchange. Characterization of a 6 mm long device was performed using a Ti:sapphire laser operating at 808 nm. The resultant laser output exhibited TE polarized single-spatial-mode operation with losses of $<0.4$ dB $cm^{-1}$ and a maximum output power of 8.5 mW for 249 mW of absorbed pump power. © *1999 American Institute of Physics.* [S0003-6951(99)02650-9]

Ion-exchange techniques provide a simple and versatile method of creating optical-fiber-compatible planar waveguide devices in glass. Actively studied and reviewed[1,2] for many years, the ion-exchange process remains almost exclusively based upon the use of a molten salt bath as a source of alkali ions, with applied heat or electric fields providing control over the rate of exchange of ions with the substrate material. The few exceptions to this method include depositing a thin layer of metal onto a substrate, a technique mainly used in the fabrication of silver and copper ion-exchanged waveguides,[2] to act as an anode for field-assisted ion-exchange processes.

The production of efficient integrated optics devices in glass requires that the inherent losses caused by light scattering from surface imperfections at the waveguide interface must be overcome, a problem leading researchers to investigate novel ways of burying waveguides below the surface of an ion-exchanged substrate. This effect is generally achieved by diffusing the waveguide region further into the material[3] with a secondary heat or electric field treatment, or alternatively by means of a second ion-exchange process designed to lower the refractive index of the substrate at the surface.[2] The additional improvement of waveguide symmetry can also reduce fiber-coupling losses,[1] but care must be taken to account for the further diffusion of ions in the material, which can alter the waveguide depth and refractive index profile.

A more recently applied method, to avoid surface related losses in borosilicate glass, has been to bond a second layer onto an ion-exchanged substrate,[4] burying the waveguide completely. This is performed using a combination of Van Der Waals forces (interatomic forces present when two flat bodies are contacted) and suitable chemical and heat treatments, which together comprise the direct bonding[5] (DB) technique. Such a process can be used to create low-loss, seamless, vacuum tight bonds between dissimilar material layers with no deleterious modification[6] of the original substrates, as evidenced in the design and realization of various multilayered active waveguide devices.[7,8]

In this letter we describe our initial study towards producing a buried waveguide laser in neodymium-doped BK-7 glass by ion exchange across a direct bonded interface. In contrast to the methods previously described, we have used the DB technique to provide a region of atomic contact between chemically modified BK-7 substrates, altered to create opposing potassium and sodium concentration gradients across the bonded interface, between which ion exchange can take place. By taking this approach we have achieved a single-step buried ion exchange mechanism with intrinsically low waveguide losses. It is the annealing phase used in DB that provides the key to this process, as the time and temperature used to strengthen direct bonded BK-7 substrates (350–400 °C for several hours) is also appropriate for $K^+$–$Na^+$ ion exchange. By performing these processes simultaneously we remove any risk of secondary diffusion of the waveguide layer, or damage to the optically polished substrates (surface condition is a critical prerequisite for DB), while also escaping the hostile environment associated with a molten salt bath.

Preparation of the rare-earth-doped substrate (illustrated as the top layer in Fig. 1) used in this experiment began by mixing pieces of commercially available BK-7 glass with 2 wt. % of neodymium oxide in a ceramic crucible. This mixture was placed in an electrically heated furnace and stirred to promote uniformity of neodymium ions within the host material. A temperature range of 850–1450 °C was available throughout the doping process, the melt being fined at 1400 °C and removed from the furnace at 1300 °C. Cast into a stainless steel mold, the melt was finally annealed in a

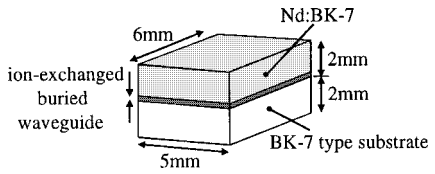


FIG. 1. Schematic diagram of the buried laser waveguide.

[a]Electronic mail: cbeg@orc.soton.ac.uk

 

muffle furnace at 580 °C. Further details of this technique can be found in Ref. 9. The second glass type, which forms the cladding layer of the device (the lower level in Fig. 1) and acts as a source of potassium for ion exchange, was prepared from basic oxide materials by a similar technique. Based on the chemical composition of commercially available BK-7,[3] our oxide mix was altered to allow an additional 4 wt. % (approximately) of $K_2O$ into the glass by removing an equal amount of $Na_2O$. Such an offset in glass composition between our BK-7-type and neodymium-doped substrates, the latter of which features 6 wt. % of both $K_2O$ and $Na_2O$ (this is slightly lower than normal due to the doping process), allows the realization of buried laser waveguides by internal ion-exchange processes in DB structures. Multiple samples have been produced by this method, proving that this is a robust technique, but it should be noted that the chemical composition of each substrate layer has yet to be optimized.

From each glass type a 2 mm thick substrate, of 10 mm×5 mm surface area, was diced and polished to provide an optically flat surface suitable for DB. After cleaning, a mixture of $H_2O_2$–$NH_4OH$–$H_2O$ (1:1:6), followed by several minutes of rinsing in de-ionized water, was applied to both materials in order to render their surfaces hydrophilic.[10] The doped and undoped layers were then brought into contact at room temperature and finger pressure applied in order to promote adhesive avalanche.[11] This effect forces any excess air or liquid from between the two substrates, as demonstrated by the removal of all interference fringes across the 10 mm×5 mm bonded interface. Annealing of the sample at 350 °C for 6 h provided ample bond strength for further machining and sufficient ion exchange to create a single-mode waveguide on the neodymium-doped side of the bonded interface. The sample was then diced and polished to the approximate absorption length expected for our neodymium-doped waveguide (~6 mm). Dimensions of the resulting buried laser waveguide device are given in Fig. 1.

The discovery of a buried waveguide near the bonded interface of our sample prompted several tests to confirm its origin as an internal ion-exchange mechanism. Optical testing produced no evidence of waveguiding as a result of any preannealing processing step (from polishing and cleaning to the DB of the two layers), although every annealed sample exhibited a buried waveguide. This result indicates that the DB heat treatment is directly responsible for the creation of optical confinement within our device.

Confirmation of the ion-exchange process within our direct-bonded samples was provided by a scanning electron microscopy (SEM) based compositional line profile analysis. This technique was used to measure the difference in relative concentration for potassium and sodium across the polished end faces of an annealed device and an unannealed control sample, the results of which are given in Fig. 2. As illustrated by the graph, there is a significant ionic redistribution between the line profiles of the unannealed (broken line) and annealed (solid line) samples, wherein $K^+$ and $Na^+$ can be seen to interdiffuse across the bonded interface. This heat-related change in chemical composition provides proof of an internal ion-exchange mechanism within our devices, the result of which is a single-step buried waveguide. Unfortunately, the low resolution available from the SEM, most evident in the rounding of the predicted step function of material composition between the two unannealed layers, requires that a mathematical deconvolution be performed in order to isolate the overall changes in ionic distribution from our results. As such our future plans include a more accurate secondary ion mass spectroscopy compositional analysis, combined with further studies into the effects of annealing time and temperature on waveguide parameters, in order to enhance our diffusion modeling.

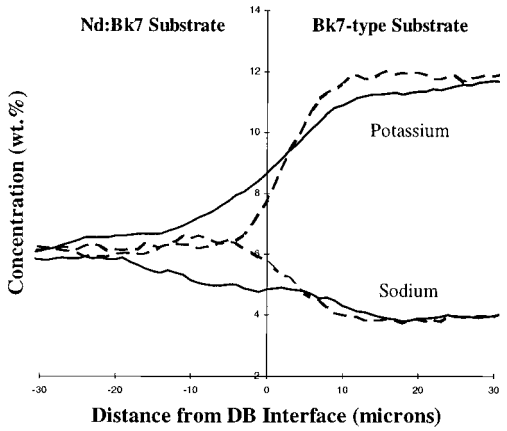


FIG. 2. A graph of chemical composition versus distance across the interface for an annealed device (solid line) and an unannealed control sample (broken line). The change in chemical profile with annealing indicates $K^+$–$Na^+$ ion exchange between the two glass substrates.

Characterization of spectroscopy, laser performance, and propagation loss of the device was performed with a tunable (700–850 nm) Ti-sapphire laser. Pump radiation was focussed for launch into the waveguide by means of a ×10 microscope objective to a measured input spot size of approximately 3 $\mu$m. Optimization of the launch was performed in relation to the fluorescence measured by a silicon detector, and a combined launch and absorption efficiency of 52% was calculated from measurements of input and output pump power from the waveguide. Fluorescence spectra from the waveguide and bulk neodymium-doped BK-7 were typical of similarly produced glass,[9] as was the recorded fluorescence lifetime of 470 $\mu$s. The typical setup used for waveguide characterization is given in Fig. 3.

Laser action was achieved in the $Nd^{3+}$ $^4F_{3/2} \rightarrow {}^4I_{11/2}$ transition by butting plane mirrors to the end faces of the device and pumping the waveguide at 808 nm. Thresholds as low as 21 mW of absorbed power were obtained with these devices using two high reflectivity (HR) mirrors. With a 3% output coupler the lasing threshold rose to 41 mW absorbed power and a slope efficiency of 6% was obtained. Maximum output power with this configuration was 8.5 mW ($\lambda = 1059$ nm) for an absorbed power of 249 mW, although no effort

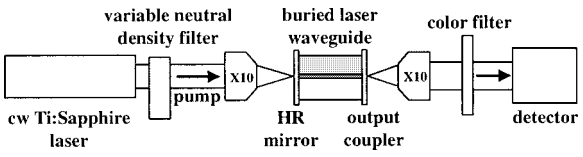


FIG. 3. Experimental arrangement for laser characterization of the buried waveguide. A pump wavelength of 808 nm was used to obtain a 1059 nm laser output from our device.

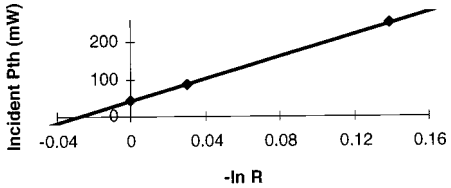


FIG. 4. Dependence of laser threshold power with output coupling.

was made to optimize the overlap of the pump and signal radiations. The output of the laser waveguide remained TE polarized regardless of pump polarization, a result confirmed in several similar devices. Such an effect could be caused by the unusual combination of stresses in our device, resulting from both the ion-exchange and DB processes, although this has yet to be investigated.

Mode profiling of the output from the buried waveguide was performed with a silicon camera and PC based evaluation software. It was observed that both the laser output and pump throughput were in the fundamental spatial mode, with guided output spot sizes ($1/e^2$ intensity radius) of 3.3 and 2.5 $\mu$m, respectively. The bonding process was not designed to give confinement in the horizontal plane, and the laser mode was observed to have an unguided spot size of $\sim$40 $\mu$m.

Propagation loss in the waveguide was estimated by investigating the relationship between laser threshold and output coupling.[12] Assuming negligible lower laser level population, constant loss with variable pump intensity, and constant laser mode size, the threshold of the laser $P_{\mathrm{th}}$ is expected to obey the equation

$$P_{\mathrm{th}} = k[2\alpha l - \ln(R_1 R_2)],$$

where $k$ is a constant encompassing the pump and laser mode spatial properties and material parameters, $l$ is the length of the monolithic cavity, $R_1$ and $R_2$ are the mirror reflectivities, and $\alpha$ is the propagation loss coefficient. By varying the output coupler a plot of threshold against $-\ln(R_1 R_2)$ was produced (Fig. 4), the $x$-axis intercept of which gives an estimate of propagation loss. For our buried waveguide a value of 2.4 $\mathrm{m}^{-1}$ was measured for $\alpha$, corresponding to a loss of 0.1 dB $\mathrm{cm}^{-1}$, although the availability of suitable mirror sets limited these results to just three points on the graph. However, separate calculations of the expected threshold and slope efficiencies (using the measured mode sizes and previously reported emission cross sections[9]) lead to values of propagation loss in the range 0.1–0.4 dB $\mathrm{cm}^{-1}$, a result which compares to the losses achieved by alternative potassium ion-exchange processes in neodymium-doped BK-7 glass.[9]

In conclusion, we have reported a fabrication technique for the single-step production of buried $K^+$–$Na^+$ ion-exchanged laser waveguides in neodymium-doped BK-7 glass. The key to this process is the direct bonding technique, which provides atomic contact between the two substrate layers and a 350 °C heat treatment suitable for simultaneous annealing and intersubstrate ion exchange. Opposing chemical gradients of potassium and sodium across the bonded interface were provided by modifying the composition of the cladding material from that of commercially available BK-7 glass. It has been shown that replacing 4 wt. % of $Na_2O$ with $K_2O$ in the cladding glass is sufficient for the production of a single-mode waveguide in an adjoining neodymium-doped BK-7 substrate. Characterization of laser performance from the buried waveguide gives a propagation loss of $<$0.4 dB $\mathrm{cm}^{-1}$ for the TE polarized laser output. These initial results suggest that optimization of glass composition and heat treatments could lead to efficient low-loss buried waveguide devices for use with integrated optics. The potential for bonding large wafers of material (to be diced into many smaller devices) for the mass production of low-loss ion-exchanged waveguides could also prove ideal for fabricating laser waveguides with long absorption lengths, such as erbium-doped devices. More generally, the direct bonding technique offers promise in providing extra degrees of design freedom for ion-exchanged waveguide devices.

The Optoelectronics Research Centre is an interdisciplinary research centre supported by the Engineering and Physical Sciences Research Council (EPSRC). Corin Gawith and Tajamal Bhutta acknowledge studentships from the EPSRC. The authors thank James Wilkinson for his advice during sample analysis.

[1] R. V. Ramaswamy and R. Srivastava, J. Lightwave Technol. **6**, 984 (1988).
[2] N. V. Nikonorov and G. T. Petrovskii, Glass Phys. Chem. **25**, 16 (1999).
[3] C. Ciminelli, A. D'Orazio, M. De Sario, C. Geradi, V. Petruzelli, and F. Prudenzano, Appl. Opt. **37**, 2346 (1998).
[4] S. Pelissier, F. Pigeon, B. Biasse, M. Zussy, G. Pandraud, and A. Mure-Ravaud, Opt. Eng. **37**, 1111 (1998).
[5] J. Haisma, B. A. C. M. Spierings, U. K. P. Biermann, and A. A. van Gorkum, Appl. Opt. **33**, 1154 (1994).
[6] K. Eda, M. Sugimoto, and Y. Tomita, Appl. Phys. Lett. **66**, 827 (1994).
[7] C. Gawith, D. P. Shepherd, J. A. Abernethy, D. C. Hanna, G. W. Ross, and P. G. R. Smith, Opt. Lett. **24**, 481 (1999).
[8] C. T. A. Brown, C. L. Bonner, T. J. Warburton, D. P. Shepherd, A. C. Tropper, and D. C. Hanna, Appl. Phys. Lett. **71**, 1139 (1997).
[9] E. Mwarania, J. Wang, J. Lane, and J. S. Wilkinson, J. Lightwave Technol. **11**, 1150 (1993).
[10] G. A. C. M. Spierings, J. Haisma, and T. M. Michielsen, Philips J. Res. **49**, 47 (1995).
[11] J. Haisma, G. A. C. M. Spierings, T. M. Michielsen, and C. L. Adema, Philips J. Res. **49**, 23 (1995).
[12] D. Findlay and R. A. Clay, Phys. Lett. **20**, 277 (1966).

# Nonreciprocal transmission in a direct-bonded photorefractive Fe:$LiNbO_3$ buried waveguide

Corin B. E. Gawith,[a] Ping Hua, and Peter G. R. Smith
*Optoelectronics Research Centre, University of Southampton, Southampton SO17 1BJ, United Kingdom*

Gary Cook
*Defence Evaluation and Research Agency, St. Andrews Road, Great Malvern, Worcestershire WR14 3PS, United Kingdom*

(Received 12 February 2001; accepted for publication 2 May 2001)

We report the fabrication of a 20-$\mu$m-thick photorefractive Fe:$LiNbO_3$ planar waveguide buried in MgO:$LiNbO_3$ by direct bonding of precision polished surfaces. Nonreciprocal transmission measurements were performed in a 3-mm-long device with a continuous wave 532 nm frequency-doubled YAG laser source. A Fresnel-reflection-based counterpropagating beam arrangement was used to measure a relative change in optical density of approximately 2 within the waveguide, with a photorefractive response time of 4.9 ms. © *2001 American Institute of Physics.* [DOI: 10.1063/1.1381028]

Nonreciprocal transmission can occur when two counterpropagating beams couple through a reflection grating in certain photorefractive crystals.[1,2] As the two beams interfere in the photorefractive media, charges excited from the bright fringes diffuse into the dark fringes, creating a periodic charge distribution throughout the illuminated region and an associated periodic electric space–charge field. This in turn causes a change in the refractive index of the material through the linear Pockel's effect, creating a refractive index grating that is phase shifted (ideally by 90°) with respect to the light interference pattern and allowing energy to be coupled from one beam to the other.[2] Power transfer occurs in one direction only, leading to reduced power transmission in one direction and increased power transmission in the opposite direction, as determined by the sign of the effective electrooptic coefficient of the crystal.

A primary application of this effect is optical limiting, where a crystal is used to reduce the transmission of coherent laser light while continuing to transmit incoherent light. This has recently received considerable attention as a means of achieving rapid optical limiting of low power continuous wave (cw) lasers, necessitating the development of efficient photorefractive materials and devices. An important material in this respect is iron-doped lithium niobate (Fe:$LiNbO_3$), a photorefractive crystal featuring an exceptionally high value small signal gain coefficient of up to 100 $cm^{-1}$.[3] This high gain coefficient, together with the use of a simple focal plane geometry, has led to reported changes in optical density ($\Delta$OD) of up to 4 with 1/*e* switching speeds of a few milliseconds.[3] At small system apertures (*f*/20 or smaller) bulk Fe:$LiNbO_3$ crystals have been found to work exceedingly well in a focal plane geometry. However, at wider apertures where the confocal parameter becomes less than the crystal path length, the degree of optical limiting decreases rapidly, becoming negligible towards large apertures, e.g., *f*/1.[4] This effect is thought to arise from competition with dark conductivity in the lower-intensity areas away from the beam waist, which reduces the effective optical interaction length within the Fe:$LiNbO_3$ crystal.[4] An ideal solution is therefore to replace the bulk crystal with a photorefractive optical waveguide in which the interaction length can be made arbitrarily long and the focused intensity is no longer related to the effective interaction length.[4]

To this end, in this letter we describe our initial study towards producing an Fe:$LiNbO_3$ photorefractive waveguide device buried in MgO:$LiNbO_3$ by direct bonding[5,6] and precision polishing techniques. Previously applied methods of waveguide manufacture in this material, such as mechanical sawing,[4,7] proton exchange,[4] and light induced frustrated etching,[4,8] have resulted in high losses, no optical limiting, and undersized features, respectively. By contrast, direct bonding is a fabrication technique used to create low-loss, seamless, vacuum tight bonds between dissimilar material layers, and has been previously used in the design and realization of highly efficient lithium niobate waveguide devices.[9] Here, the combination of a photorefractive Fe:$LiNbO_3$ waveguide with direct-bonded nonphotorefractive MgO:$LiNbO_3$ cladding layers has resulted in an efficient buried waveguide device for optical limiting experiments.

Fabrication of the waveguide device began with a sample of $LiNbO_3$ doped with 0.08 mol % of iron. Provided that the crystal has a sufficiently high electron-trap density, optical limiting in Fe:$LiNbO_3$ is insensitive to the total Fe content (at least over the doping range of 0.01–0.1 mol %) and depends mainly on the linear transmission characteristics of the crystal which in turn depend on the relative densities of the $Fe^{2+}$ and $Fe^{3+}$ oxidation states of the iron doping. In Fe:$LiNbO_3$, the $Fe^{2+}$ ions absorb in the visible spectrum and act as electron charge donors, while the $Fe^{3+}$ ions are transparent and act as charge traps. A linear transmission of between 30% and 60% in uncoated crystals with 3–6 mm path lengths usually gives good results.[2] Magnesium-doped lithium niobate (MgO:$LiNbO_3$) was chosen for both the substrate and cladding layers of our buried waveguide device. MgO:$LiNbO_3$ has a refractive index lower than that of either

[a]Electronic mail: cbeg@orc.soton.ac.uk

 

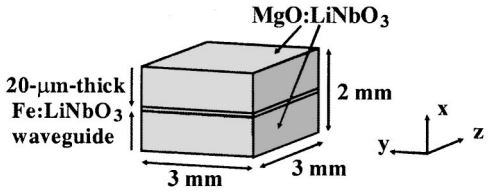


FIG. 1. Schematic diagram of the direct-bonded Fe:$LiNbO_3$ buried planar waveguide device.

undoped lithium niobate or Fe:$LiNbO_3$ (Ref. 10) and features similar thermal properties to those of the iron-doped waveguide layer, an important prerequisite when annealing bonds at high temperatures. An additional benefit of MgO:$LiNbO_3$ is that the MgO doping effectively suppresses the photorefractive effect, ensuring that nonreciprocal transmission will be observed in the buried waveguide region of our device only. For this experiment 5 mol % of magnesium was added to the melt during crystal growth, a value associated with photorefractive resistance in lithium niobate.[11]

From each crystal type a 1-mm-thick x-cut substrate of 6 mm $\times$ 6 mm surface area was diced and polished to provide an optically flat surface suitable for direct bonding. After cleaning, a mixture of $H_2O_2-NH_4OH-H_2O$ (1:1:6), followed by several minutes of rinsing in de-ionized water, was applied to both materials in order to render their surfaces hydrophilic.[12] The Fe:$LiNbO_3$ and MgO:$LiNbO_3$ layers were then brought into contact at room temperature, with both samples aligned along the same crystalline orientation, and finger pressure applied in order to promote adhesive avalanche.[13] This effect forces any excess air or liquid from between the two substrates, as demonstrated by the elimination of the interference fringes at the crystal interface. Annealing of the bonded sample at 350 °C for 6 h provided a sufficient bond strength for further machining and the Fe:$LiNbO_3$ region was then polished down to obtain a waveguiding layer of 20 $\mu$m thickness (with a variance of less than 1 $\mu$m across the entire layer). A further cladding layer of MgO:$LiNbO_3$ was then added using the same procedure as above. The device was completed by removing any residual unbonded edge regions with dicing equipment and polishing the end faces of the waveguide to a parallel optical finish. The final dimensions of the buried Fe:$LiNbO_3$ waveguide device are given in Fig. 1.

Measurement of nonreciprocal transmission in our Fe:$LiNbO_3$ waveguide was performed using two-beam coupling in a counterpropagating beam geometry, a technique illustrated in Fig. 2. This allows the signal beam to be derived from the weak Fresnel reflection of the incident beam at the exit face of the crystal,[4] thereby eliminating the need

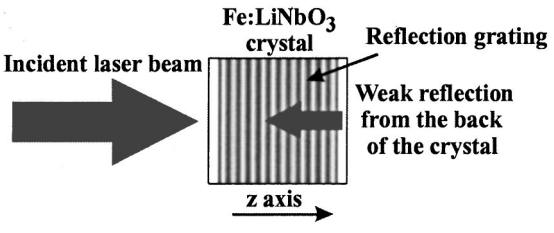


FIG. 2. Two-beam coupling in a counterpropagating beam geometry in Fe:$LiNbO_3$.

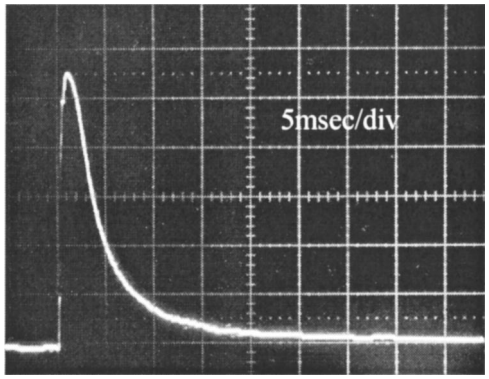


FIG. 3. Far-field optical limiting in the Fe:$LiNbO_3$ buried waveguide at 80 kW $cm^{-2}$ peak focused intensity at 532 nm.

for beam splitters and other ancillary optics. The device is inserted into the beam such that the incident light propagates along the *z* axis of the crystal, providing access to the material's highest effective electro-optic coefficient, $r_{\text{eff}} = \pm r_{13} \approx 9.6$ pm $V^{-1}$.[2] For this experiment a continuous wave 532 nm frequency-doubled Nd:YAG laser source was first preexpanded and collimated to overfill a well corrected *f*/5 spherical lens. This technique provides an approximately uniform beam for focusing onto the front face of the buried Fe:$LiNbO_3$ waveguide and avoids any ambiguity over the actual *f* number arising from the use of a Gaussian beam. The focused spot was therefore an Airy pattern rather than a Gaussian, and only the central lobe contained within the first minima of the Airy pattern was launched into the waveguide. While a cylindrical lens would be more appropriate for use with our multimode planar waveguide, allowing reduction of beam divergence in the unguided direction and thus a more uniform beam intensity along the crystal length, a spherical lens was used in this experiment due to the large aberrations present in our available cylindrical lenses. A fast-response shutter mechanism was used to block the pump beam prior to each crystal exposure and a photodiode was used to measure the far-field transmission characteristics of the device. Upon exposure, the pump transmission in the waveguide declines due to the formation of a volume reflection grating in the photorefractive material as the pump and signal beams interfere. At high intensities (where the photogeneration rate is much greater than the erasure rate from the dark conductivity) optical limiting occurs with a response time inversely proportional to intensity such that the rate of decline is rapid at first but becomes progressively slower as the intensity declines at the rear of the device. This effect is demonstrated in the oscillograph of Fig. 3. From the trace, the relative change in optical density obtained by optical limiting, $\Delta$OD, is determined by

$$\Delta \mathrm{OD} = \log_{10}(I_P / I_{\mathrm{SS}}), \tag{1}$$

where $I_P$ is the peak transmitted intensity at time $t=0$ and $I_{\mathrm{SS}}$ is the steady-state transmitted intensity. For our arrangement, an input focused intensity of approximately 80 kW $cm^{-2}$ gave a measured $\Delta$OD of 2 and $1/e$ response time of 4.9 ms in the Fe:$LiNbO_3$ buried waveguide. This result represents a significant improvement over the bulk material at large apertures, with approximately 20 times less steady-state output transmission and 60 times faster optical limiting

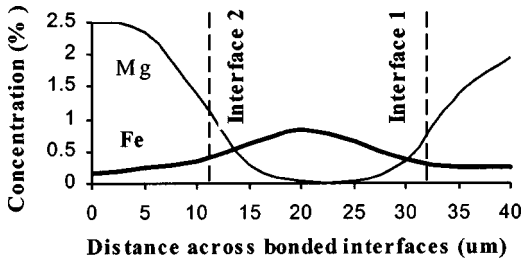


FIG. 4. Chemical composition vs distance across the direct-bonded interfaces of the device. The nonsymmetrical diffusion profile arises as a result of the two annealing processes required to complete the three-layered device.

response than a similar bulk crystal. (A 2.7-mm-long bulk $LiNbO_3$ crystal doped with 0.07 mol % of iron gives a $\Delta$OD of 0.71 and *1/e* response time of 298 ms in the same launch arrangement.) However, the intensity required to achieve millisecond-order response times in our photorefractive waveguide was higher than expected from similar experiments with bulk Fe:$LiNbO_3$ crystals,[2] indicating nonoptimized launch conditions or a possible change in local material properties during the direct bonding process. Since optical limiting in Fe:$LiNbO_3$ is intensity dependent,[2] the first of these problems is likely to arise from the spherical lens used to focus light into the waveguide. Beam divergence in the unguided plane will rapidly reduce the pump intensity with distance, followed by a subsequent decrease in the $\Delta$OD. This deleterious effect would not occur in a channel waveguide geometry, as could be realized, for example, by titanium indiffusing a parallel array of channel waveguides into the planar iron-doped substrate prior to direct bonding.

Investigation of the material properties of our direct bonded sample was performed using a scanning electron microscopy based compositional line profile analysis. While the absolute resolution of this technique is limited by the micron-order spot size of the electron beam, the measurement is sufficient to illustrate the relative changes of iron and magnesium concentrations across the polished end face of our device, the results of which are given in Fig. 4. The graph shows significant interdiffusion of iron and magnesium ions across the two bonded interfaces of the sample, indicating ion exchange between the atomically contacted substrate layers. Such a change in chemical composition is due to the high-temperature annealing used in direct bonding[14] and represents a possible degradation mechanism for the optical limiting efficiency of the Fe:$LiNbO_3$ waveguide layer. For example, reduced iron content leads to reduced photoconductivity, electron trap density and charge generation and recombination rates, reducing the coupling gain and slowing down the response time of the photorefractive material. Further, the presence of magnesium at the edges of the buried waveguide suppresses the photorefractive effect in these areas, reducing the active volume of the waveguide layer. This reduces the average two-beam coupling gain and increases the input intensity needed to achieve a given reduction in optical transmission. However, optimization of material composition and annealing conditions should reduce these effects in future devices.

In conclusion, we have reported the fabrication of a 20-$\mu$m-thick photorefractive Fe:$LiNbO_3$ waveguide buried in MgO:$LiNbO_3$ by direct bonding and precision polishing techniques. Characterization of optical limiting in this device was performed using two-beam coupling in a counterpropagating beam geometry with a 532 nm cw frequency-doubled Nd:YAG laser source. For an input focused intensity of approximately 80 kW $cm^{-2}$ a relative change in optical density of 2 and a response time of less than 5 ms were achieved using *f*/5 focusing optics. This result represents a steady-state optical limiting transmission 20 times less than the bulk material and a 60 times faster photorefractive response time. Overall, the buried planar waveguide structure allows access to wide aperture imaging systems for high-speed optical limiting applications, and future devices based on this technology are likely to incorporate multiple-layer structures and linear arrays of titanium indiffused channel waveguides.

The Optoelectronics Research Center is an interdisciplinary research center supported by the Engineering and Physical Sciences Research Council (EPSRC). This work was supported by a DERA funded CASE award.

[1] A. Krimins, Z. Chen, and T. Shiosaki, Opt. Commun. **117**, 147 (1995).
[2] G. Cook, D. C. Jones, C. J. Finnan, L. L. Taylor, and A. W. Vere, Proc. SPIE **3798**, 2 (1999).
[3] G. Cook, C. J. Finnan, and D. C. Jones, Appl. Phys. B: Lasers Opt. **68**, 911 (1999).
[4] G. Cook, J. P. Duignan, L. L. Taylor, and D. C. Jones, Proc. SPIE **4106**, 230 (2000).
[5] J. Haisma, G. A. C. M. Spierings, U. K. P. Biermann, and A. A. von Gorkum, Appl. Opt. **33**, 1154 (1994).
[6] A. Plössl and G. Kräuter, Mater. Sci. Eng., R. **25**, 1 (1999).
[7] S. Yin, A. V. Petrov, Y. Suzuki, and K. Shinoda, Opt. Mem. Neural Networks **7**, 155 (1998).
[8] I. E. Barry, R. W. Eason, and G. Cook, Appl. Surf. Sci. **143**, 328 (1999).
[9] C. B. E. Gawith, D. P. Shepherd, J. A. Abernethy, D. C. Hanna, G. W. Ross, and P. G. R. Smith, Opt. Lett. **24**, 481 (1999).
[10] J. Noda, M. Fukuma, and S. Saito, J. Appl. Phys. **49**, 3150 (1978).
[11] T. Volk, N. Rubinina, and M. Wohlkecke, J. Opt. Soc. Am. B **11**, 1681 (1994).
[12] Y. Tomita, M. Sugimoto, and K. Eda, Appl. Phys. Lett. **66**, 1484 (1995).
[13] J. Haisma, G. A. C. M. Spierings, T. M. Michelsen, and C. L. Adema, Philips J. Res. **49**, 23 (1995).
[14] C. B. E. Gawith, T. Bhutta, D. P. Shepherd, P. Hua, J. Wang, G. W. Ross, and P. G. R. Smith, Appl. Phys. Lett. **75**, 3757 (1999).

**Appendix C**
**PATENTS**

**Fabrication of Optical Waveguides**
**International PCT Application No. PCT/GB99/03055**
**Corresponding to UK Patent Application No. 9820024.9**

Attached are the abstract specifications related to the above patent application. The patent described arises from the work on buried PPLN waveguides in direct-bonded structures and proposed experiments with doped substrate materials (see Chapter 3 for full details).

**PCT** WORLD INTELLECTUAL PROPERTY ORGANIZATION
International Bureau

INTERNATIONAL APPLICATION PUBLISHED UNDER THE PATENT COOPERATION TREATY (PCT)

(51) International Patent Classification [7]: G02B 6/12, G02F 1/377 — A1

(11) International Publication Number: **WO 00/16140**

(43) International Publication Date: 23 March 2000 (23.03.00)

(21) International Application Number: PCT/GB99/03055

(22) International Filing Date: 14 September 1999 (14.09.99)

(30) Priority Data:
9820024.9 14 September 1998 (14.09.98) GB

(71) Applicant *(for all designated States except US)*: UNIVERSITY OF SOUTHAMPTON [GB/GB]; Highfield, Southampton, Hampshire SO19 1BJ (GB).

(72) Inventors; and
(75) Inventors/Applicants *(for US only)*: SMITH, Peter, George, Robin [GB/GB]; 38 Eight Acres, Romsey, Hampshire S051 5BQ (GB). ROSS, Graeme, William [GB/GB]; 35 Gladstone Place, Queen's Cross, Aberdeen AB10 6UX (GB). HANNA, David, Colin [GB/GB]; 346 Hill Lane, Shirley, Southampton, Hampshire SO15 7PH (GB). SHEPHERD, David, P. [GB/GB]; Flat 2, 116 Highfield Lane, Highfield, Southampton, Hampshire SO17 1NP (GB). GAWITH, Colin, Barry, Edmund [GB/GB]; 24 Upland Court Road, Harold Wood, Romford, Essex RM3 0TT (GB).

(74) Agent: TURNER, James, Arthur; D Young & Co., 21 New Fetter Lane, London EC4A 1DA (GB).

(81) Designated States: AE, AL, AM, AT, AU, AZ, BA, BB, BG, BR, BY, CA, CH, CN, CR, CU, CZ, DE, DK, DM, EE, ES, FI, GB, GD, GE, GH, GM, HR, HU, ID, IL, IN, IS, JP, KE, KG, KP, KR, KZ, LC, LK, LR, LS, LT, LU, LV, MD, MG, MK, MN, MW, MX, NO, NZ, PL, PT, RO, RU, SD, SE, SG, SI, SK, SL, TJ, TM, TR, TT, TZ, UA, UG, US, UZ, VN, YU, ZA, ZW, ARIPO patent (GH, GM, KE, LS, MW, SD, SL, SZ, TZ, UG, ZW), Eurasian patent (AM, AZ, BY, KG, KZ, MD, RU, TJ, TM), European patent (AT, BE, CH, CY, DE, DK, ES, FI, FR, GB, GR, IE, IT, LU, MC, NL, PT, SE), OAPI patent (BF, BJ, CF, CG, CI, CM, GA, GN, GW, ML, MR, NE, SN, TD, TG).

**Published**
*With international search report.*

(54) Title: FABRICATION OF OPTICAL WAVEGUIDES

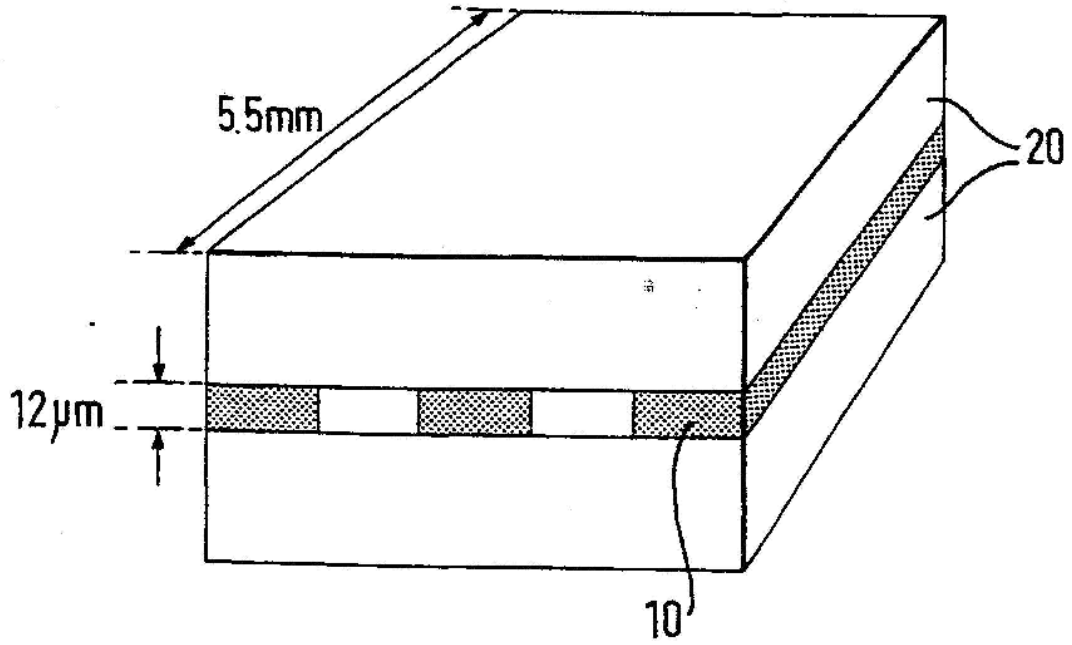


(57) **Abstract**

An optical waveguide comprising at least a guiding lamina (10) of optical material bonded by direct interfacial bonding to a superstructure lamina (20) of optical material, in which regions of the guiding lamina have modified optical properties so as to define a light guiding path along the guiding lamina. In a particular example, a periodically poled $LiNbO_3$ planar waveguide is buried in $LiTaO_3$ by direct interfacial bonding and precision polishing techniques and used in an optical frequency doubling system.